Thermomechanically Processed Magnesium-Silver Alloys as Antibacterial and Biodegradable Implant Materials

Dissertation

zur Erlangung des akademischen Grades

Doktor der Ingenieurwissenschaften

(Dr.-Ing.)

der Technischen Fakultät

der Christian-Albrechts-Universität zu Kiel

vorgelegt von

Zhidan Liu

Kiel 2018

Erstgutachterin: Prof. Dr. Regine Willumeit-Römer

Zweitgutachterin: Prof. Dr. Christine Selhuber-Unkel

Termin der Disputation: 11.01.2018

Eidesstattliche Erklärung

Hiermit erkläre ich, dass die beigefügte Dissertation, abgesehen von der Beratung durch die Betreuerin, nach Inhalt und Form meine eigene Arbeit ist.

Die Arbeit, ganz oder zum Teil, wurde nie schon einer anderen Stelle im Rahmen eines Prüfungsverfahrens vorgelegt und ist abgesehen, von den im Anhang angegebenen Veröffentlichungen, nicht anderweitig zur Veröffentlichung vorgelegt worden.

Außerdem ist die Arbeit unter Einhaltung der Regeln guter wissenschaftlicher Praxis der Deutschen Forschungsgemeinschaft entstanden.

Geesthacht, den 15. 10. 2017

Abstract

In this study, “smart” Mg-Ag alloys as antibacterial and biodegradable implant materials were prepared and systematically evaluated. The microstructure of the as cast Mg-Ag alloys with varied silver content was regulated with respect to the grain size and precipitates via different thermomechanical processing. The processing includes casting, homogenization, hot extrusion, equal channel angular pressing (ECAP), friction stir processing (FSP) and rolling with subsequent annealing. The influence of microstructure on tensile properties and degradation behavior was revealed. The cytocompatibility, mineralization, antibacterial properties and degradation mechanism of Mg-Ag alloys were evaluated. The finer grains and more second phases/precipitates $Mg_{54}Ag_{17}$ contributed to a higher hardness and tensile strength. However, the second phases/precipitates accelerated degradation rate and caused severe pitting, whereas the grain size of Mg-Ag alloys had no significant effect on the degradation rate. Twins in the as rolled Mg-Ag alloys had influence on degradation morphology instead of the degradation rate. The hardness, tensile strength and elongation at break of the as rolled Mg-Ag alloys were adjusted by short time annealing. In terms of biological evaluations, the cytocompatibility was improved by reducing the degradation rate of Mg-Ag alloys. The antibacterial properties of Mg-Ag alloys were enhanced via increasing silver content. Through optimizing the microstructure, the Mg-Ag alloys with high silver content have obtained good antibacterial properties even in harsh dynamic conditions but had almost equivalent cytocompatibility to human primary osteoblasts as pure Mg. In mineralization assay, large amounts of hydroxyapatite (HA) formed on pure Mg via inorganic mineralization. The cell biomineralization activity was slightly higher on Mg-Ag alloys than on pure Mg. The biomineralization products were HA particles. However, the biomineralization activity was weakened with the increase of silver content. The degradation of Mg-Ag alloys was mainly due to micro-galvanic corrosion. However, physiological conditions also influenced the degradation behavior. During degradation process, the inorganic mineralization involving HCO_3^-, Ca^{2+}, SO_4^{2-} and HPO_4^{2-}/H_2PO^{4-} ions led to the formation of dense $Mg_xCa_y(PO_4)(OH)_z$ rather than HA on the surface of Mg-Ag alloys, which retarded the degradation process effectively when the degradation rate was not higher than 3.2 mm/year in HBSS with 10% FBS. The proteins were absorbed on the surface of Mg-Ag alloys and decreased degradation rate when the degradation rate was between 1.46 and 10.28 mm/year in HBSS. Most of the AgNPs are combined with the proteins after being released from Mg-Ag alloys.

Zusammenfassung

Das Ziel dieser Arbeit war die Herstellung und systematische Untersuchung von binären Mg-Ag Legierungen als “smarte” degradierbare Implantatmaterialien mit zusätzlichen antibakteriellen Eigenschaften. Das Gefüge der Legierungen wurde mittels thermomechanischer Prozessierung in Bezug auf Korngröße und Anzahl der Sekundarphasen systematisch variiert. Die angewandte Prozessierung beinhaltete Guß, Wärmebehandlungen, Strangpressen, equal channel angular pressing (ECAP), Reibrührschweissen (FSP) und Walzen mit anschließendem Aushärten. Der Einfluss dieser unterschiedlichen Gefüge auf die mechanischen und Degradations-eigenschaften wurde untersucht. Weitere Untersuchuingen befassten sich mit dem Einfluss der Legierungszusammensetzung auf die Zellkompatibilität, die antibakteriellen Eigenschaften, sowie die Degradationsmechanismen. Feine Körner und mehr Sekundärphasen ($Mg_{54}Ag_{17}$) führten zu höherer Härte und Zugfestigkeit. Gleichzeitig erhöhten die Sekundärphasen jedoch die Degradationsrate und induzierten Lochfraßkorrosion, wohingegen kein Einfluss der Korngröße auf Degradation festgestellt werden konnte. Zwillingsbildung in den gewalzten Legierungen wirkte sich auf die Degradationsmorpholgie aus, aber nicht auf die Degradationsrate. Durch kurze Aushärtungszyklen konnte die Härte, Zugfestigkeit und Bruchdehnung gezielt eingestellt werden. Die Zellkompatibilität zeigt einen direkten Zusammenhang mit der Degradationsrate, die antibakterileen Eigenschaften konnten durch Erhöhung des Silbergehaltes verbessert werden. Durch gezielte Einstellung der Mikrostruktur konnte erreicht werden, das auch die hochlegierten Silberlegierungen sowohl antibakterielle Wirkung hatten, als auch ähnlich zellkompatibel wie reines Magnesium sind. Hydroxylapatit als Degradationsprodukt wurde auf reinem Magnesium durch anorganische Mineralisierung gebildet. Die zelluläre Mineralisierung durch Osteoblasten war auf den Silberlegierungen höher als auf reinem Mg, wuden jedoch durch eine Erhöhung des Silbergehalts vermindert. Obwohl die Degradation der Legierungen hauptsächlich durch mikrogalvanische Korrosion gesteuert warden, hatten auch die angewandten physiologischen Umgebungsbedingen einen deutlichen Einfluss. Die anorganische Mineralisierung, getrieben durch HCO_3^-, Ca^{2+}, SO_4^{2-} and HPO_4^{2-} /H_2PO^{4-} Ionen führten zur Bildung dichter $Mg_xCa_y(PO_4)(OH)_z$ Schichten. Diese Schichten konnten den Degradationsprozess deutlich verlangsamen, wenn die Degradationsgeschwindigkeit niedriger als 3.2 mm/a war. Proteine adsorbierten auf der Oberfläche der Legierungen und verlangsamten ebenfalls die Degradation. Zusätzlich wurden Silber-Nanopartikel gebildet, die mit den Proteinen assoziierten.

Contents

1. State of art

1.1 Magnesium alloys as biodegradable implant materials

There are approximately 25 grams of magnesium in an adult human body and two-thirds of the magnesium is located in the skeleton [1]. Magnesium is osteoinductive and has good biocompatibility with human body [2]. The human body can tolerate relative high amount of magnesium without adverse reactions [2]. Moreover, unlike permanent implants [3, 4], magnesium and its alloys have the advantage of biodegrading in situ [5-7]. The biodegradable magnesium implants can be dissolved gradually in physiological environment. This eliminates the necessity of a revision surgery to remove implants from the human body again [8], so patients avoid a secondary operation. The risk of additional infections is also reduced. However, biodegradable materials in most of the clinical applications are mainly polymeric or ceramic materials, e.g., DL-PLA (polylactic acid) and HA (hydroxyapatite), which have inadequate mechanical properties when used for load-bearing parts [8]. Compared to currently applied biomaterials, magnesium alloys have higher ductility than synthetic HA and higher strength than the PLA [9]. Moreover, magnesium alloys have many other advantages. They have high strength/weight ratio and the Young's modulus (E) is 41-45 GPa which nears the E of the natural bone [7, 8, 10, 11]. This Young's modulus matches human cortical bones well compared to the currently applied permanent materials, e.g., stainless steel 361L or Ti6Al4V [8, 12, 13]. Hence, magnesium alloys minimize the stress shielding effect and support the bones to self-repair and bond [8-10]. Moreover, magnesium alloys exhibits better biocompatibility than PLA which was described to cause inflammation of the surrounding tissues [14]. Hence, magnesium alloys are promising to be applied as biodegradable implant materials.

The first application of biodegradable magnesium implants is reported for the 19th century [15]. Pure magnesium (pure Mg) was applied as biodegradable implant to fix a bone fracture [15, 16]. Until now, many studies were carried out on magnesium and its alloys, to promote the application as biodegradable implants. Binary, ternary and even quaternary magnesium alloys were developed, such as Mg-Ag, Mg-Ca, Mg-Zn, Mg-Zn-RE and Mg-Y-RE-Zr etc. [11, 17-22]. The screws made of magnesium alloys were designed to show a reasonable degradation rate *in vivo* (Fig. 1.1). Some magnesium and its alloys have already been developed into biodegradable bone fixtures and bone scaffolds used in orthopedic surgery [23]. Bone fixtures are used to fix the fractured parts to promote the healing of bone tissues. The scaffolds provide temporary support to bone tissue reconstruction and are expected to be replaced by new bones

with time [2]. For example, vascularized bone graftings were fixed by biodegradable magnesium screws to treat osteonecrosis of the femoral heads of patients [24]. Mg-Ca-Zn screws were used to treat distal radius fractures in 53 patients [25]. In coronary angioplasty, magnesium alloys were applied as vascular stents. Coated stents can not only expand the vessels but also elude drugs as local treatment of the lesion area [26-28]. It will degrade completely after healing the lesion area of coronary obstructions [9, 15, 29-32].

Fig. 1.1: MAGNEZIX® compression screws in different sizes. From left to right: MAGNEZIX® CS 2.0, MAGNEZIX® CS 2.7, MAGNEZIX® CS 3.2, MAGNEZIX® CS 4.8 (*reproduced with permission from SPRINGER [33]*).

However, there are still some issues that need to be solved before the magnesium alloys are widely applied as biodegradable implant materials, such as low inherent strength, unsatisfactory degradation rate, and the resulting problems of insufficient mechanical integrity, cytocompatibility and histocompatibility [34]. For example, in orthopedic applications, the magnesium alloys need to possess high enough strength to experience tension and compression stresses during a minimum of 3-4 months service, in which new bones will form and restore most of the original strength [9, 35]. However, the mechanical properties of magnesium alloys are still low for bone fixation [19].

The application of magnesium alloys as biomedical devices is also limited by their fast degradation rate in physiological fluids [7, 36-40]. The service period of magnesium implants is shorter than the healing time of the fracture bones [8, 10-12]. They lose strength because of the fast degradation rate and local pitting before the healing of bone tissues [35]. The magnesium implants collapse before the tissues are completely healed [8, 41-45]. Hence, the mechanical integrity of implants is an important indicator of orthopedic applications. Researchers did the mechanical integrity tests on the porous pure Mg and extruded Mg-Zn alloys. The mechanical integrity dropped drastically even after only several percent weight loss [19, 46, 47]. For most of the available magnesium alloys, satisfying results still cannot be described. Low mechanical integrity caused by the fast degradation rate and local pitting prevented the application progress

of magnesium alloys as biodegradable implants [19, 46]. Hence, magnesium alloys should possess suitable high initial strength and good ductility as they will deteriorate gradually during the degradation process [19, 48]. It is not only a matter of mechanical loss during degradation but also a problem of the tissue healing. The degradation rate of magnesium alloys is too high for cells in the physiological conditions in which the pH value is 7.4-7.6 and many chloride ions exist. As a result of high degradation rate, many hydrogen gas bubbles generate and accumulate to form gas pockets to separate tissues during the degradation. The collective effect of gas bubbles and alkalization of local position may delay the healing of bones and could be deleterious to the surrounding tissues [7, 10, 49, 50].

Overall, magnesium alloys should provide sufficient strength in a specific period until the healing of tissues. Meanwhile, the degradation should be low enough and homogeneous. The key point is to improve the mechanical properties as well as degradation resistance. These properties are mainly related to the microstructure of magnesium alloys. Therefore, to develop new magnesium alloy with good inherent mechanical properties, low degradation rate and uniform degradation property, the optimization of microstructure is necessary.

1.2 Degradation of magnesium alloys *in vitro* and *in vivo*

The fast degradation rate of magnesium alloys leads to detrimental influence to the human tissues, organisms and mechanical integrity [49]. The fundamental reason is that magnesium alloys have much negative electrode potential and are apt to degrade in electrolytic aqueous environment. To slow down the degradation rate and eliminate the detrimental interaction, it is essential to reveal the degradation mechanism [51], especially in physiological conditions.

Numerous studies have been conducted to understand the degradation mechanism [37, 52-54]. There are various solutions for *in vitro* immersion tests including NaCl (Sodium Chloride Solution), HBSS (Hank's Balanced Salt Solution), SBF (Simulated Body Fluid) and DMEM (Dulbecco's Modified Eagle Medium) etc. [45, 55-59]. The degradation rates obtained on the basis of these solutions could be quite different [9]. For the inorganic substances, the degradation rate is generally considered to be related to ions, such as chloride, carbonate, sulfate, phosphate and calcium ions, in the physiological environment (Fig. 1.2) [60, 61]. The breakdown potential decreases if the chloride concentration increases [62]. The carbonate and sulfate ions in physiological environment attack magnesium alloys, thus accelerating magnesium dissolution. Some studies mentioned that a higher concentration of HCO_3^- ions

induced more effective protection layer in SBF solution [56]. The phosphates and calcium ions play key role in the formation of hydroxyapatite (HA) and other magnesium/calcium phosphates salts in SBF solution [19, 40, 54, 56]. Some synergetic effects of these ions on the degradation behavior of magnesium and its alloys were evaluated [40, 54, 60].

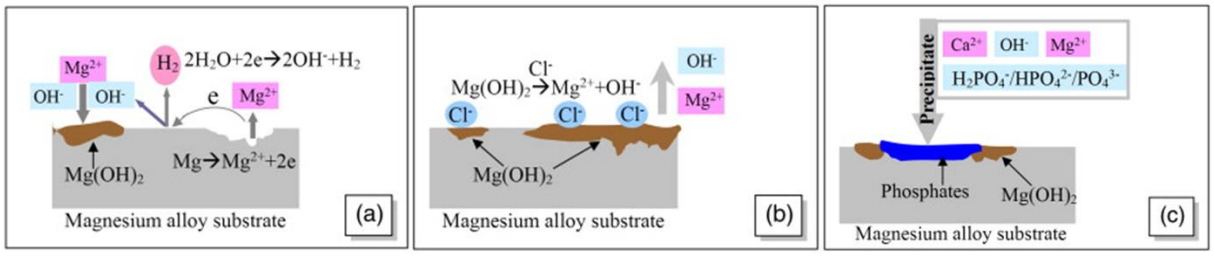

Fig. 1.2: Schematic illustration of reactions between magnesium alloy and SBF: the galvanic reaction between substrate and H_2O (a), the dissolution of $Mg(OH)_2$ (b) and the precipitate of phosphates (including HA and other magnesium-substituted calcium phosphates) (c) (*reproduced with permission from ELSEVIER [61]*).

In the presence of albumin, the potential range of the passivation region of magnesium and its alloys could be extended [62]. In the study of permanent metals as implants, the influence of BSA (bovine serum albumin) to degradation is complex. Several studies stated that BSA adsorption can reduce or accelerate the corrosion of permanent metals. The theories of the formation of BSA passive films and metal dissolution are the main explanations to those results [63-68]. In the study on magnesium and its alloys, it has been reported that the addition of albumin in SBF delayed degradation rate, since a protein layer adhered to the surface and acted as a barrier between magnesium alloys and physiological environment [39, 43, 69]. However, other studies mentioned that proteins increased the degradation of magnesium alloys. The reason should be that the proteins contain various metal cations that accelerated the degradation rate to some extent [21, 70]. Electrochemical experiments showed that the synergistic effect of insoluble salt formation and protein adsorption retarded magnesium degradation [54, 71]. Moreover, magnesium alloys possesses a much higher degradation rate *in vitro* than *in vivo* [6], especially when no proteins exist *in vitro*. Magnesium alloys exhibited different degradation rate in different parts of the body [72]. Therefore, the physiological environment strongly affects the degradation behavior as the microstructure of magnesium alloys [57, 73-75].

Hence, it is essential to evaluate the degradability of magnesium alloys in physiological

conditions to understand the degradation mechanism [10, 76]. The application of appropriate solutions is important for the degradation evaluation *in vitro* [54]. In degradation process, the influences between magnesium alloys, inorganic substances, proteins and cells are mutual. However, few studies revealed the degradation mechanism by evaluating the interaction between the degradation, proteins and cells.

1.3 Infections associated with implants and treatment by silver

The clinical application of biodegradable implants and prosthesises has shown rapid growth to keep with the demands of a rapidly aging population. But implant-associated infection is becoming an increasingly prevalent problem with respect to the modern healthcare system and prolonged hospital nursing. Both biodegradable and permanent implants have the potential of infections. Related study investigated the infection rates among 2114 patients treated with bioabsorbable osteosynthesis devices. In a comparison with metallic osteosynthesis devices (3111 ankle fracture patients), there was no significant difference between the infection rates of the bioabsorbable fixation group (3.2%) and metallic fixation group (4.1%) [77]. For humans, the overall implant-associated infection rate is estimated to be approximately 5% in the clean surgical procedure [78, 79].

This is a common post-operative infection and can cause biofilm formation on the implants or osteomyelitis [80-86]. The formation procedure of biofilms on implants is illustrated (Fig. 1.3). Biofilms are resistant to antibiotics and can protect bacteria from host immune mechanisms. Once a biofilm has formed, the only treatment is to remove the implants and the diseased tissues [87-89], so it is necessary and urgent to deal with this problem. Prevention is the preferred method to address the growing problem of implant-associated infections [90, 91].

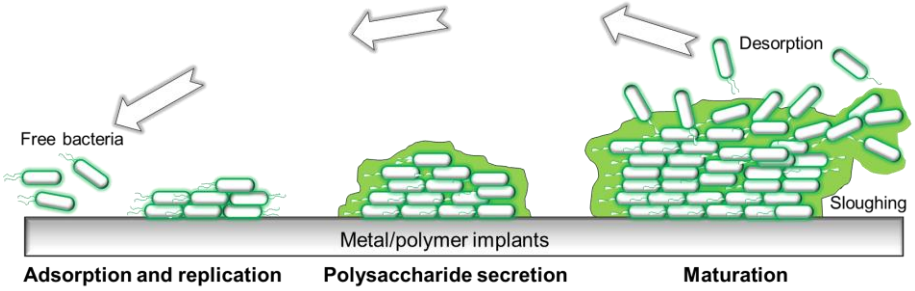

Fig. 1.3: Formation procedures of biofilms on implants.

Compared to permanent implants, magnesium alloys as biodegradable implant materials have the advantage of not requiring removal after bone tissue healing [10]. Therefore, additional infections caused by a second surgery can be avoided. Moreover, pure Mg, as a promising metal for biodegradable orthopedic implants, exhibits some antibacterial effects due to the alkaline pH value produced during degradation [92-94]. In the early stage, the alkaline environment is adverse to the survival and reproduction of bacteria [95, 96]. Moreover, pure Mg induced osteoblasts and suppressed bacteria in an infected rabbit tibial model [97]. However, some other studies revealed that metallic magnesium as biodegradable implant materials is permissive for bacterial biofilms formation *in vivo* even though it exhibits some antibacterial properties *in vitro* [98]. The reason should be that the antibacterial effect may be inadequate in the local dynamic environment, e.g., the human body, which will influence the resistance to infection and affect osteomyelitis treatment [8, 97]. The other cause is that the degradation rate of pure Mg and its alloys *in vivo* is lower than that *in vitro* [6, 99, 100]. In this case, a high pH cannot be maintained, so it sounds unrealistic for pure Mg or magnesium alloys to achieve effective inhibition to bacteria. Even if a very high pH was applied by increasing the degradation rate to eliminate bacteria, the surrounding tissues would also be influenced.

With the emergence of multi-resistant bacteria, how to avoid or treat orthopedic implant-associated infection and biofilm formation is a complicated issue [85]. Many methods have been studied, e.g., coating and surface morphology, to endow permanent implants or magnesium alloys the function of suppressing bacteria or reducing bacterial adhesion [101-105]. Studies tried to handle this issue by coating or mixing silver on permanent implants [106, 107]. Considering the great demand for medical devices to increase life expectancy, novel biodegradable magnesium alloys with better antibacterial properties are desirable. The addition of silver (Ag) into magnesium provides us another idea to improve the antibacterial properties of magnesium alloys.

Silver has effective broad-spectrum antimicrobial properties and has been used to treat burns and chronic wounds for centuries [108]. Silver nano-particles (AgNPs) and silver ions can bind to proteins and the membrane of bacteria. They interfere with DNA expression, create reactive oxygen species (ROS) and affect thiol group compounds that exist in respiratory enzymes to inhibit respiratory processes [101, 109, 110]. A principle of silver reacting with bacteria was shown (Fig. 1.4). The emergence of antibiotic-resistant strains of bacteria has promoted the use of metallic silver to prevent infections of indwelling devices [101]. There are cases of silver applications that focus on the antibacterial properties, e.g., wound dressing, bone cement and

megaprosthesis [107, 111, 112]. Silver-coated megaprosthesis can release silver ions and reduce the infection rate compared to the group without silver [107].

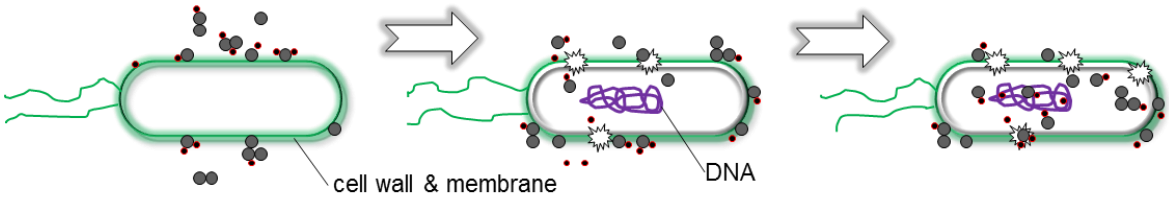

Fig. 1.4: Antibacterial principle of silver nano-particles and silver ions to *Escherichia coli* as an example.

However, the accumulation of a high amount of silver in the human body can cause argyria or argyrosis, which results from the deposition of significant amounts of insoluble silver precipitates in the dermis of the skin and the cornea or conjunctiva of the eyes [113, 114]. However, no pathological damage to tissues can be observed. The threshold amount of silver that can evoke argyria ranges from 3.8 to 5 g or even 10 g over the whole lifetime of adults [115]. The total body silver concentration that can cause argyria is 1 g for children under 10 years old [116]. Hence, the application of silver in the human body should be under these limitations. In clinical course, the amount of silver coated on megaprosthesis ranges from 0.4 to 1.69 g in adult patients [107]. However, no relevant evidence shows that such a low amount of silver in the human body or chronic silver exposure can cause pathological changes of any tissue or organ [113-115, 117]. Moreover, the loss of cell viability *in vitro* due to metallic silver or silver compounds is dose-dependent [118-120]. Metallic silver has a lower risk of toxic effects compared to soluble silver compounds [121].

To endow effective antibacterial properties of magnesium alloys, the silver is preferred to be alloyed with magnesium. Silver can dissolve into magnesium or form intermetallic compounds with magnesium [122], thus the magnesium-silver (Mg-Ag) alloys could possess long-term and broad-spectrum antibacterial properties during degradation, compared to drug-release coating. Previous studies identified that the addition of silver into magnesium can achieve better antibacterial properties than pure Mg [17]. Therefore, it can be assumed that the antibacterial properties can be improved with the increase of silver content in magnesium. The multi-functional Mg-Ag alloys should have good antibacterial properties and are supposed to reduce infections and biofilm formation on implants effectively.

1.4 Thermomechanical processing of magnesium alloys

In general, the microstructure has a major influence on the mechanical properties and degradation behavior of metallic materials. The problems of low mechanical properties and high degradation rate of as cast magnesium alloys are related to the microstructure which refers grains and second phases. The microstructure of as cast magnesium alloys can be changed by further processing. However, the processing at ambient temperature is hindered by poor cold workability due to insufficient slipping systems, which is a fundamental problem of magnesium alloys [123], so the processing should be carried out at elevated temperature.

Microstructure regulation through thermomechanical processing has been developed extensively [124]. Magnesium alloys have low stacking fault energy (LSFE) [125]. Thermomechanical processing provided the possibility to improve mechanical properties via dynamic recrystallization (DRX). Generally, thermomechanical processing can result in fine grains. Grain refinement leads to not only higher strength at ambient temperature but also better elongation and ductility [32, 126, 127]. The fine-grained materials also exhibit enhanced workability at elevated temperatures [124], which is important for further processing of Mg-Ag alloys. The formation of new grains via dynamic recrystallization during the thermomechanical processing follows the mechanisms including nucleation by bulging, sub-grain rotation and twinning [125, 128, 129]. Moreover, thermomechanical processing can adjust the quantity and dispersion of precipitates well.

Microstructure of magnesium alloys after thermomechanical processing is usually in non-equilibrium state with defects. The grains have a tendency to grow during the subsequent heating. An annealing treatment which leads to static recrystallization (SRX) is often needed after hot working. The static recrystallization is also an effective method to control the microstructure of magnesium alloys. It involves the formation of new fine grains by migrating of high angle grain boundaries, which is driven by the stored energy after plastic deformation [130-132]. As a result of these recrystallizations, grain refining can improve both mechanical strength and ductility of magnesium alloys [133-136]. In recent years, more attention was paid on the static recrystallization during annealing after hot deformation [137, 138]. In most cases, it is stated that grain growth occurred in the subsequent annealing after hot working [139-141]. Some studies calculated the formulation between grain size, annealing time and temperature [136, 142]. In general, the grains of metallic materials enlarge with the increase of annealing time and temperature until equilibrium [139, 143]. Therefore, the annealing time and

temperature should be carefully controlled. Otherwise, abnormal grain growth will take place [139], especially, when the annealing temperatures near the melting point are applied [144, 145]. The deterioration in the final mechanical properties could happen during the annealing of plastic deformed magnesium alloys. From another perspective, the static recrystallization is operative to control the mechanical properties [146-148].

The microstructure control of the grain refinement and the dispersion of precipitates in matrix by extrusion can improve the mechanical properties of magnesium alloys [149]. Equal channel angular pressing (ECAP) is an efficacious technique of fabricate ultrafine grained (UFG) metallic materials without remarkable geometrical change of bulk materials [150, 151]. A very small grain size less than 1 μm of magnesium alloy could be obtained by ECAP. A good combination of high strength and high ductility at room temperature was attained via grain refinement. Recent studies showed that the degradation rate of ZM21 magnesium alloy was retarded by fine grains after hot extrusion and ECAP as well as that of AZ31 after ECAP plus rolling [32, 127]. The ECAP is an efficient way to reduce the degradation rate of ZE41A and AZ31 magnesium alloys [59, 127, 152].

The innovative friction stir processing (FSP) technique [153] appears to be a very promising processing method for broadening the industrial application of magnesium alloys. During this process, the material undergoes extreme levels of plastic deformation and thermal exposure, which normally leads to significant microstructure refinement and principal textural changes in the center of the so-called ‘‘stirred zone”. The FSP parameters have great influence on microstructure, hardness and mechanical properties of magnesium alloys [154]. The electrochemical impedance spectroscopy (EIS) and salt spray test results demonstrated that the stirred zone exhibited higher pitting corrosion resistance than the base AZ31 material [155].

Rolling is another feasible processing to change the microstructure of magnesium alloys. The rolling and annealing at high temperature refers to both dynamic recrystallization (DRX) and static recrystallization (SRX). It influences the mechanical properties and degradation rate much. The high degradation tendency of the as cast Mg-1Ca was remarkably reduced by the rolling process due to microstructure refinement [156]. However, the primary rolling can result in a strong basal texture [144, 157-159], which will cause anisotropic plastic behavior [160-163]. Recrystallization via annealing is an efficient method to weaken the basal texture and results in a relative homogeneous microstructure of magnesium alloys [163-165].

2. Motivation and objectives

It is desirable to develop Mg-Ag alloys with the advantage of antibacterial properties against wide range of bacteria, to deal with the infections and osteomyelitis in orthopedic implant operations. The requirements of Mg-Ag alloys as multi-functional biodegradable implant materials include high initial strength, low enough degradation rate, homogeneous degradation, good cytocompatibility and effective antibacterial properties.

- The mechanical properties and degradation behavior are related to microstructure and composition of magnesium alloys. Magnesium and its alloys have poor formability at room temperature because of lacking slip systems, so the microstructure should be changed by thermomechanical processing at elevated temperature. In this thesis, the microstructures of Mg-Ag alloys with varied silver content were purposely treated by several different thermomechanical processing, to increase mechanical strength and slow down degradation rate. The thermomechanical processing includes hot extrusion, ECAP, FSP and rolling with subsequent annealing. The influence of microstructure and silver content on the mechanical properties and degradation behavior of Mg-Ag alloys *in vitro* was studied.
- It is anticipated that the antibacterial properties under harsh dynamic conditions could be increased by alloying silver metal with pure Mg as much as possible. The Mg-Ag alloys can release silver continuously to provide long-term and broad spectrum antibacterial properties compared to drug-release coating on magnesium alloys. It is expected that the infections can be prevented successfully when Mg-Ag alloys are applied as bone implant materials in the future. Meanwhile, the Mg-Ag alloys should not show obvious cytotoxicity to human primary osteoblasts. Moreover, the corresponding cells should be able to synthesize HA to participate in the reconstruction of bone tissues.
- The degradation behavior of Mg-Ag alloys is not only influenced by microstructure and silver content but also the degradation environment. It is necessary to shed a light on the mechanism occurring during the whole degradation procedure in reasonable solutions before trying to reduce it. Mg-Ag alloys will serve in physiological conditions, so it is needed to reveal the effect of inorganic substances and proteins on the degradation behavior of Mg-Ag alloys.

Therefore, the effects of microstructure and the silver content on mechanical properties, degradation behavior, cytocompatibility, mineralization, antibacterial properties and degradation

mechanism of Mg-Ag alloys *in vitro* are in the focus of this thesis. The ultimate aim is to find ways or techniques to improve the mechanical properties, slow down the degradation rate and obtain relative homogeneous degradation morphology as well as good cytocompatibility and antibacterial properties of Mg-Ag alloys as bone implant materials.

3. Experiments

3.1 The principles of major instruments in characterization

3.1.1 X-ray fluorescence and X-ray diffraction

X-ray fluorescence (XRF) spectrometry is widely applied for the routine determination of the major elements as well as many important trace elements. When the specimen is excited by a primary X-ray or gamma rays beam, the interaction of X-rays with atoms will cause the ionization of inner shell orbital electrons via “photo-electric effect” (Fig. 3.1). In this status, the atoms are unstable. They will decay immediately to a more stable electronic configuration via the transition of shell electrons to fill the vacancies. At the same time, excess energy is released as secondary "fluorescence" X-rays. The intensity of this characteristic fluorescence radiation is proportional to the atomic concentration of the respective element after correction.

This phenomenon can be used for Ag (wavelength 0.05599 nm) analysis in magnesium without interference by the nearest elements Palladium (Pd, wavelength 0.05859 nm) and Cadmium (Cd, wavelength 0.05357 nm) [166]. This wavelength dispersive X-ray fluorescence spectrometry (WDXRF) in this study has high precision. It can analyze the elements from Beryllium (Be) to Uranium (U) in the concentration range from sub-ppm-level to 100%.

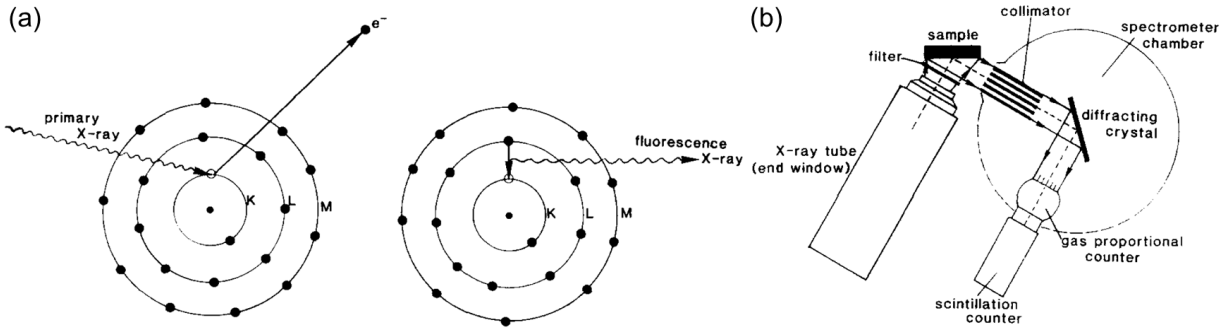

Fig. 3.1 Photoelectric ionization of an inner shell electron leading to X-ray fluorescence (K-line) (a), schematic arrangement of a wavelength dispersive X-ray fluorescence spectrometer (b) (*reproduced with permission from ELSEVIER [167]*).

For X-ray diffraction (XRD, Fig. 3.2), when a crystal is irradiated by an X-ray beam with a comparable wavelength λ, the X-ray diffraction can be observed at specific angles 2θ if the Bragg’s Law ($n\lambda = 2d\sin\theta$) is satisfied. The "n" is an integer and the X-ray wavelength λ is fixed. The diffraction angle θ is determined by a goniometer. According to the Bragg’s Law, the crystal

lattice constants (d) can be identified. According to the obtained lattice constants, the phases can be identified in the database.

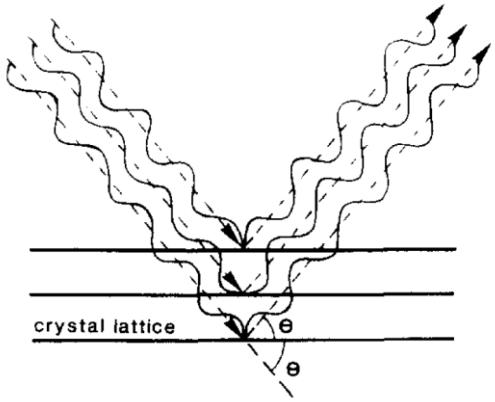

Fig. 3.2 Bragg diffraction from a crystal grating showing incident X-ray photons having a wavelength that satisfies the Bragg equation for constructive interference in the diffracted beam for an angle of incidence θ (*reproduced with permission from ELSEVIER [167]*).

3.1.2 Electron beams and scanning electron microscope

Electron beams are widely used in material characterization. When the primary electron beam hits the specimen, several different signals are generated (Fig. 3.3). The signals include secondary electrons, back-scattered electrons, transmitted electrons, auger electrons, characteristic X-rays and photons.

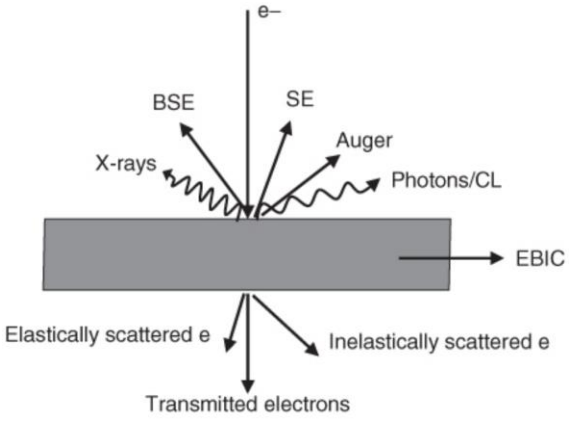

Fig. 3.3 Overview of the signals generated when an electron beam interacts with a (relatively) thin specimen. In the case of a thick specimen there are no transmitted electrons and the signal gets absorbed within the material (*reproduced with permission from WILEY [168]*).

Scanning electron microscope (SEM, Fig. 3.4a) obtains images by scanning the surface using a

focused electron beam. In secondary electron (SE) mode (Fig. 3.4b), the electrons are released from the very close surface, so the images have very high resolution. In back-scattered electrons (BSE) mode, the electrons are reflected from the samples via elastic scattering. They come from deeper position of the samples. The BSE images have less resolution than the SE images, but the BSE images can distinguish the distribution of different elements in the samples. As an accessory device of SEM, the energy dispersive X-ray spectroscopy (EDS) is a qualitative and quantitative X-ray microanalytical technique, which can provide the information of elemental composition of samples.

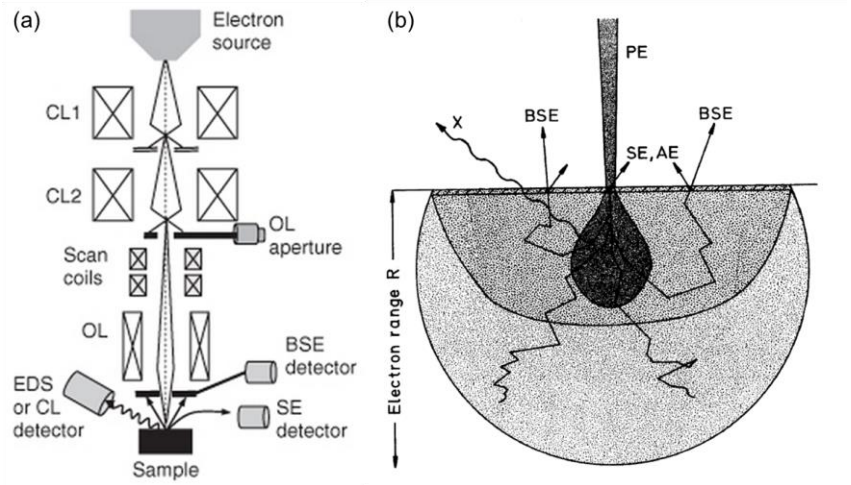

Fig. 3.4 Simplified schematic cross-sections of SEM (a) (reproduced with permission from WILEY) [168], origin and information depth of secondary electrons (SE), back-scattered electrons (BSE), Auger electrons (AE) and X-ray quanta (X) in the diffusion cloud of electron range *R* for normal incidence of the primary electrons (PE) (b)(*reproduced with permission from SPRINGER*) [169].

3.1.3 Fluorescence microscopy and stainings

A basic requisition for fluorescence microscopy (Fig. 3.5) is that the objects of interest can emit fluorescence. The fluorescence is the emission of light in nanoseconds, after the absorption of light which has typically shorter wavelength than the emitted one. The difference of wavelength between the primary and emitted lights, which is called the “Stokes shift”, is an interesting phenomenon that makes fluorescence applied widely. By filtering out the primary light and allowing the emitted fluorescence to go through the fluorescence cube, only the objects that emit fluorescence are observed. There is a big advantage of this method compared to absorption techniques in which substances are stained with agents that can absorb light: the absorption techniques hardly can be used to distinguish the difference between small object and

its background. However, for the fluorescence method, even single fluorescent molecule could be observed if its background has no auto fluorescence.

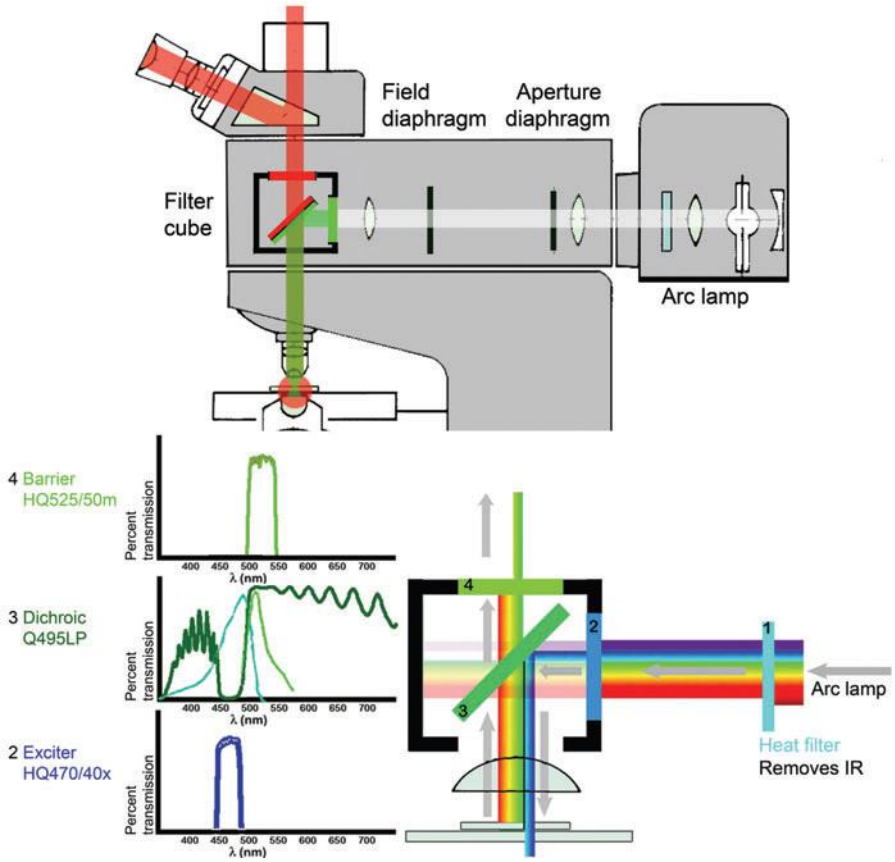

Fig. 3.5 The fluorescence microscope. (a) Epi-illumination fluorescence microscopes use the objective both to illuminate and image the specimen. Shown is an upright microscope with the slide at the bottom. The light source, in this case an arc lamp, sends full-spectrum light to the specimen by way of a fluorescence cube that selectively illuminates the specimen with a wavelengths that excite a particular fluorophore (shown, green light to excite rhodamine). The red fluorescence that is excited sends photons in all directions and a fraction are collected by the objective and sent through the cube to the eye or camera port above. The cube has two filters, the dichroic mirror and barrier filter, to prevent the exciting wavelengths from reaching the detector. (b) The details of a cube designed by Chroma Technologies to excite and detect enhanced green fluorescent protein. The three main components (labeled 2, 3 and 4) have specific spectral features that are ideal for green fluorescent protein. Note that the dichroic mirror splits between reflection and transmission right between the absorption and emission peaks of the green fluorescent protein, which are superimposed in blue and green, respectively (*reproduced with permission from NATURE METHODS [170]*).

For the LIVE/DEAD® Viability/Cytotoxicity Kit (Molecular Probes, Eugene, USA), the polyanionic dye calcein is well retained within live cells, producing an intense uniform green fluorescence in live cells. EthD-1 enters cells with damaged membranes and undergoes a 40-fold enhancement of fluorescence upon binding to nucleic acids, thereby producing a bright red fluorescence in dead cells. However, EthD-1 can be excluded by the intact plasma membrane of live cells. In mineralization assay, the principle of OsteoImage™ Assay is based on the specific binding of the fluorescent OsteoImage™ Staining Reagent to the hydroxyapatite.

3.2 Preparation of materials

The Mg-Ag alloys containing 6, 8 and 10 wt.% silver are denominated as Q6, Q8 and Q10, respectively, according to ASTM B275 [171]. The procedures of casting and thermomechanical processing are shown in Fig. 3.6. The designation of different samples is displayed in Fig. 3.7.

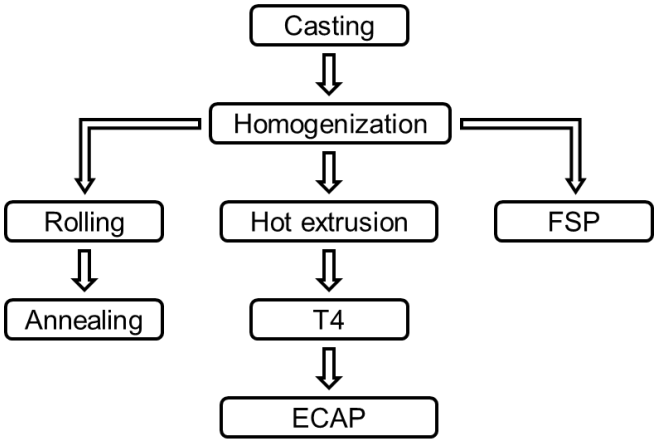

Fig. 3.6: Casting, heat treatment and different thermomechanical processing.

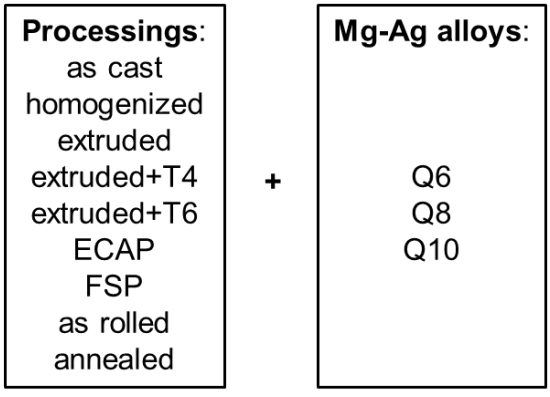

Fig. 3.7: The abbreviations of different samples.

3.2.1 Cast procedure of Q6, Q8 and Q10

Magnesium (99.99 wt.%, Xinxiang Jiuli Magnesium Co., Ltd, Xinxiang, China) and silver granules (99.99 wt.%, ESG Edelmetall-Handel GmbH. & Co. KG, Rheinstetten, Germany) were used for the preparation of Q6, Q8 and Q10 alloys by permanent mould direct chill casting in the Magnesium Innovation Center in Helmholtz-Zentrum Geesthacht. Pure Mg was cut into small pieces and placed into a steel crucible with the corresponding amount of silver. The metals were molten at 750°C in steel resistance furnace with the protection of the mixed gas (98% argon (Ar) and 2% sulfur hexafluoride (SF_6)) and stirred at 200 rpm for 30 min. After the temperature of the melt dropped to 730°C, it was poured into a permanent steel mold (diameter ø=120 mm) which was coated inside with the mold release agent, hexagonal boron nitride (Büro für Angewandte Mineralogie Dr. Stephan Rudolph, Tönisvorst, Germany). There were two types of mold, the cylindrical one (ø120×200 mm) for hot extrusion and the cuboid one (250×110×55 mm) for rolling and FSP. After keeping for 15 min at 680°C, the mold was cooled by dipping it into flowing water gradually at a speed of 100 cm/min until the molten Q6, Q8 and Q10 solidified. Pure Mg was cast into cylindrical ingots.

3.2.2 Simulation of Mg-Ag phase diagram

The Mg-Ag phase diagram in literatures has obvious difference (Fig. 3.8) [172], which is adverse to the parameter setting of the thermomechanical processing and data analysis. To solve this problem, a new Mg-Ag phase diagram (Fig. 3.9) was simulated via Pandat™ 8.1 software (CompuTherm LLC, Madison, USA), as a reference for thermomechanical processing and microstructure analysis.

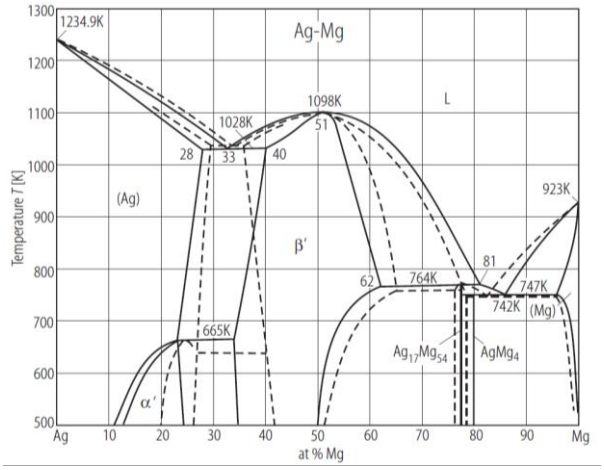

Fig. 3.8: The difference of Mg-Ag phase diagrams in two publications (*reproduced with permission from SPRINGER [122, 173]*).

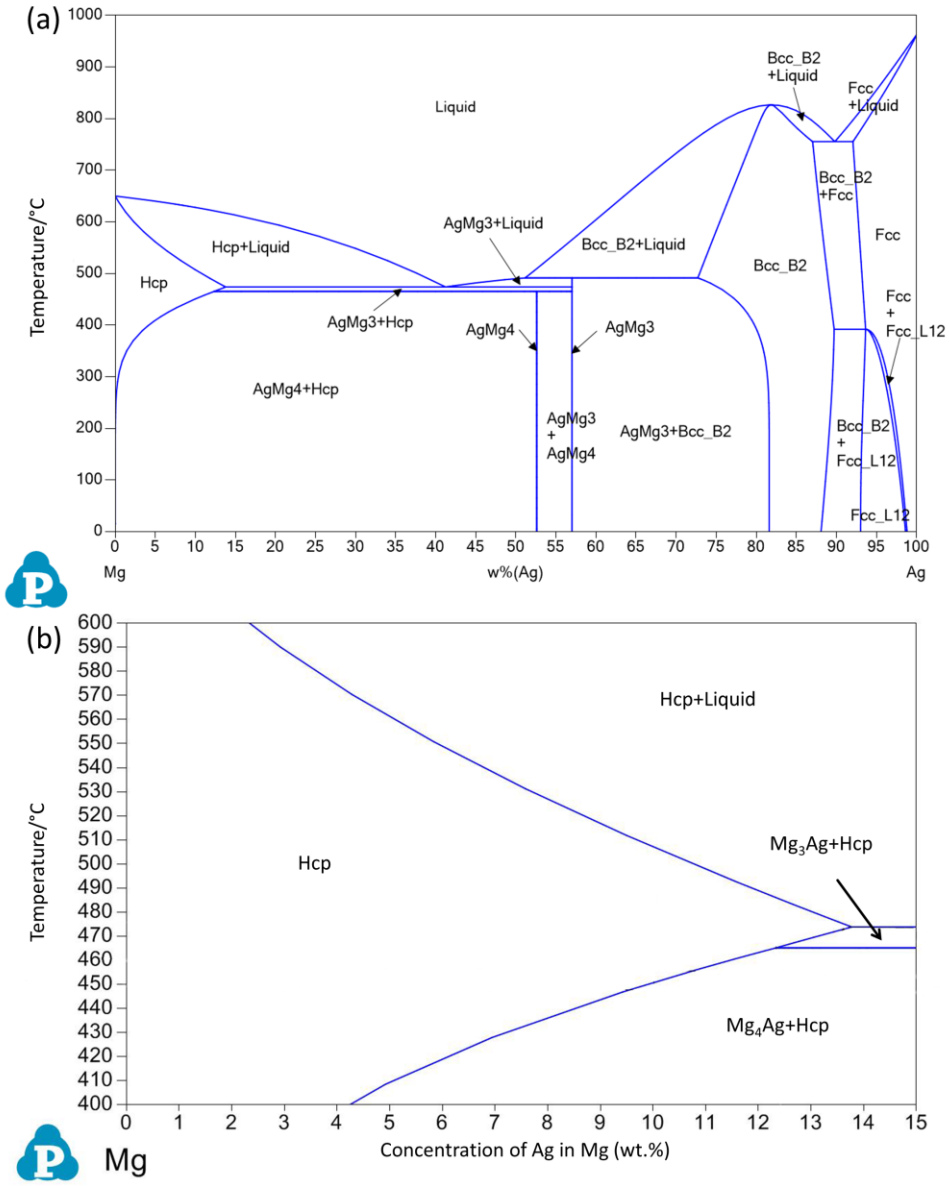

Fig. 3.9: Simulated whole Mg-Ag phase diagram (a) and partial Mg-Ag phase diagram (b) via Pandat^{TM} 8.1 software.

3.2.3 Quality control and homogenization of ingots

The main reason for the low corrosion resistance of Mg and its alloys is internal galvanic attack due to impurities or alloying elements [174]. The tops (5 cm) and bottoms (2 cm) with shrinkages and impurities were removed from the ingots. The samples were grinded on P320, P500, P800, P1200 and P2500 sandpapers (Hermes WS-Flex 18 C, Hamm, Germany). Several areas were chosen to check the composition and impurities in the ingots by X-ray fluorescence spectrometer (Bruker AXS S4 Explorer, Bruker AXS GmbH., Germany) and with a Spark

Analyser (Spectrolab M, Spektro, Germany). The chemical composition of the as cast ingots is collected in Table 1. It is concluded that impurity levels are in the tolerable range from the point view of the corrosion rate [175].

Table 1 Chemical composition of Q6, Q8 and Q10 in wt.%

Mg-Ag alloys	Ag	Fe	Cu	Ni	Si	Be
Q6	6.1 ± 0.4	<0.03800	<0.00420	<0.00113	<0.00540	<0.000040
Q8	8.1 ± 0.3	<0.00207	<0.00170	<0.00107	<0.01700	<0.000042
Q10	10.6 ± 0.9	<0.00214	<0.00107	<0.00113	<0.00093	<0.000040

According to literatures and the simulated Mg-Ag phase diagram, the maximum solubility of silver in magnesium is lower than 15 wt.% at eutectic temperature which is the lowest melting point of a mixture of components [122]. To acquire a homogeneous microstructure and stable mechanical properties in the following thermomechanical processing, homogenization treatments were performed. According to the simulated Mg-Ag phase diagram, the homogenization treatments of ingots were carried out at about 450°C (Q6 and Q8) and 460°C (Q10) in resistance furnace (Linn Elektro Therm AK 40. 06, Bad Frankenhausen, Germany) for at least 8 hours with the protection of Argon (Ar). They were quenched by dipping into 20°C water. After that, the cylindrical ingots were machined into smaller one (⌀100×200 mm) for hot extrusion. The cuboid ingots were cut into two pieces from the center along the length direction and machined into slices (200×100×20 mm) for rolling.

3.3 Thermomechanical processing of Mg-Ag alloys

The thermomechanical processing includes general hot extrusion, equal channel angular pressing (ECAP), friction stir processing (FSP), and the rolling with subsequent annealing, which are described in the following paragraphs. Some heat treatments (solid solution (T4) and aging (T6)) were also conducted on the basis of thermomechanically processed materials.

3.3.1 Hot extrusion and heat treatments

The Q6, Q8 and Q10 ingots were heated up (285°C for Q6 and 300°C for Q8 and Q10) and processed by hot extrusion (Strangpresszentrum Berlin, Berlin, Germany). They were transferred into the container of the hot extrusion machine (Fig. 3.10). The diameter and temperature of ingots, container and steel die are listed, as well as extrusion ratio and punch speed (Table 3.1). After the hot extrusion, the extruded bars were cooled in air. The top (100 cm)

and bottom (100 cm) of the extruded bars were cut off, since defects and impurities, e.g., lubricant and oxidation, existed in the center of these parts.

T4 treatments were conducted by placing them in a steel box filled with Ar and keeping them in a resistance furnace (Vulcan™ A-550, DENTSPLY CERAMCO, USA) at about 450°C (Q6 and Q8) and 460°C (Q10) for 8 h. Then, the Mg-Ag alloys were quenched. T6 treatments were carried out at 200°C for 5 hours.

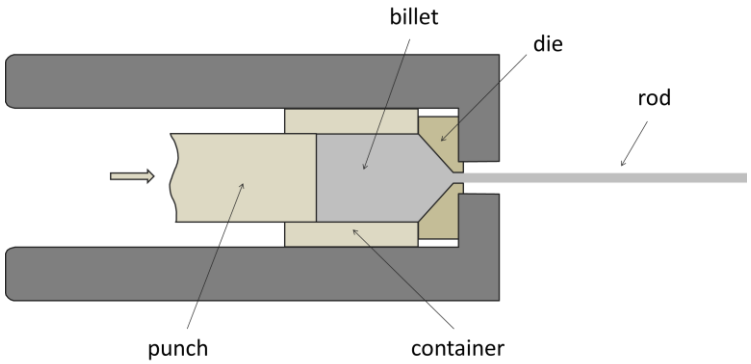

Fig. 3.10: Schematic illustration of hot extrusion.

Table 3.1: The applied parameters in hot extrusion.

Parameters		Q6	Q8	Q10
Billets	Diam. (mm)	100	100	100
	T (°C)	285	300	300
Container	Diam. (mm)	125	125	110
	T (°C)	300	300	300
Die	Diam. (mm)	12	12	12.5
	T (°C)	300	300	300
Extrusion ratio		108	108	72
Punch speed (mm/s)		0.7	0.7	0.7

3.3.2 Equal Channel Angular Pressing

The equal channel angular pressing (ECAP) was carried out in the department of materials engineering (Prof. Yuri Estrin's group) in Monash University in Australia. The extruded Q6 and Q8 except for Q10 were processed by ECAP (Fig. 3.11) after T4 treatments at 450°C for 8 hours. The extruded+T4 Q10 already possesses much high degradation rate, so it was not considered

to be processed further by ECAP. The diameter of the equal channel was 12 mm and the angles φ and ψ are 90° and 0°, respectively. The samples were heated to 250°C first and then pressed by a 7 ton pressure. A total of 4 passes were carried out to obtain an ultrafine microstructure.

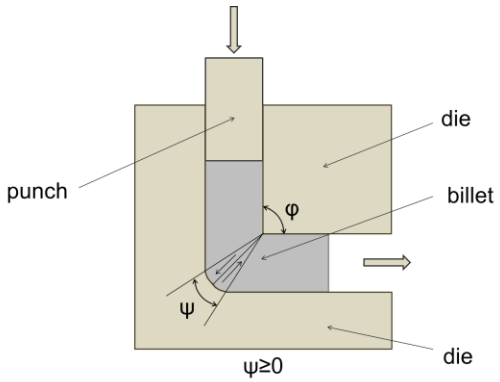

Fig. 3.11: Schematic illustration of equal channel angular pressing.

3.3.3 Friction Stir Processing

The cuboid ingots of Q6 and Q8 were applied for FSP (Fig. 3.12) in the division of materials mechanics in Helmholtz-Zentrum Geesthacht. The upper and lower surfaces were processed by AMStech AW3SL electrical discharge machine (EDM) and milled to ensure that the two surfaces are parallel. Hermes P800 sandpapers were used to clean the surface to remove potential copper, zinc and iron impurities introduced by EDM and milling. The ingots were screwed on the table of FSP machine (HZG Gantry System, Helmholtz-Zentrum Geesthacht, Germany). A tool (probe of ø 8×8 mm with a shoulder ø = 20 mm) made of hot working steel (MP159) was applied. The parameters were 12 kN pressure, 2000 rpm of the tool, and 200 mm/min forward speed. Some water was used to cool the ingots fast after processing. Before the next processing, the tool was always cooled in the water and cleaned by ethanol. The same areas of the ingots were chosen to ensure similar thermal conditions during processing every time.

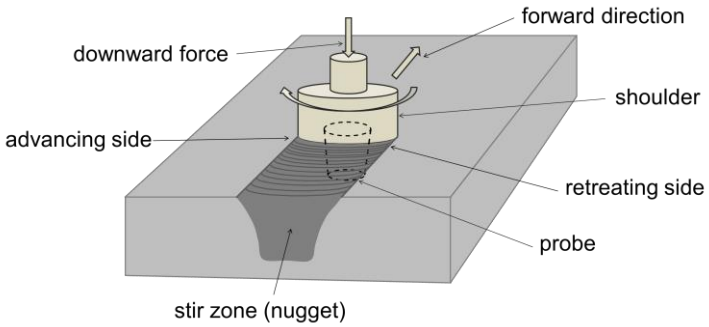

Fig. 3.12: Schematic illustration of friction stir processing.

3.3.4 Rolling and annealing

The Q6 and Q8 slabs were applied to the rolling on a Metz M205 dual cold-rolling mill (Fig. 3.13) in Magnesium Innovation Center in Helmholtz-Zentrum Geesthacht. Rolling temperature varied between 350, 400 and 450°C. The rolling speed was 10 m/min. The rolling schedule consisted of 13 passes with varied degree of deformation per pass. The formulation is:

$$\varepsilon_t = -\ln(t_{n+1}/t_n) \qquad \text{Eq. 3.1}$$

The *t* is the thickness of the sample and n the number of the actual pass. During the rolling, 4 passes with ε_t = 0.1 were applied followed by 9 passes with ε_t = 0.2. Between each two passes the samples were reheated for 15 min in an air-circulating furnace at rolling temperature. This condition is referred to as the "as-rolled condition". Different annealing treatments were applied as indicated in the results using an air circulating furnace. In general annealing, a part of the as-rolled sheets was annealed for further 30 min at the respective rolling temperature. In short time annealing, a part of the as rolled sheets were annealed in the furnace for 20 s, 30 s, 40 s, 50 s, and 60 s at 350, 400 and 450°C for Q6 and 450°C for Q8. This condition is referred to as the "annealed condition".

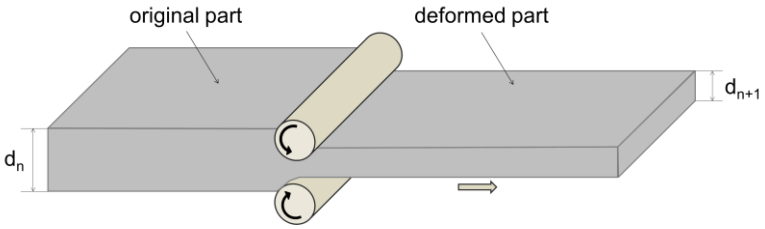

Fig. 3.13: Schematic illustration of rolling.

3.3.5 Sample preparation

The as cast samples were cut by hand saw from the center of the ingots. The extruded rods were cut into discs (ø 10×1.5 mm) (Henschel KG, Munich, Germany). The ECAP Mg-Ag alloys were machined into discs (ø10×1.5 mm) by electrical discharge machine (EDM). The stirred zones (nugget) in FSP were confirmed by grinding, polishing and etching until the appearance of the microstructure with fine grains. The stirred zones were cut off by EDM. Brittle fracture occurred on the top surface of the stirred zone because of lower harness and defects in this part [176], so the top part of the stirred zones with defects and impurities were removed via grinding on sandpapers. The samples of the as rolled and annealed sheets were cut by an electric band saw from the center parts and then grinded.

3.4 Microstructure analysis

3.4.1 Metallography preparation

The Q6, Q8 and Q10 samples except for the as cast alloys were embedded in Demotec 30 (Demotec metallografie, Nidderau, Germany). After the plastic was set, the samples were grinded on sandpapers from P220 to P2500 to remove the plastic deformation layers which were caused by cutting. Then, the samples were polished on rubber cloth with water-free OP-S (oxide polishing suspensions, Cloeren Technology GmbH, Wegberg, Germany) for 30 min at least. The residual OP-S on the polished surface was removed via distilled water and pure ethanol. The surfaces were blown dry by compressive air.

The composition of etching solution differs with the silver content of Mg-Ag alloys and their status. The chemicals in etching solution include ethanol, glacial acetic acid and picric acid (Sigma-Aldrich Chemie GmbH, Steinheim, Germany). These are typical chemicals used for metallographic analysis of magnesium alloys. The amount of distilled water and acetic acid in etching solution varied with silver content. The etching time of Q6, Q8 and Q10 alloys was also different (1.5 s for Q6, 1 s for Q8 and 0.5 s for Q10). For Q6 and Q8 alloys other than the ECAP and FSP alloys, the etching solution consisted of 100 mL ethanol, 20 mL distilled water, 6.5 mL glacial acetic acid and 12-15 g picric acid (99%). For Q10, the ethanol and glacial acetic acid in the etching solution were 120 and 2 mL, respectively. The glacial acetic acid in the etching solution for ECAP and FSP samples increased to 10 mL. Assistent^{TM} cotton sticks (Thermo Fisher Scientific, Schwerte, Germany) were applied to clean the surface of ECAP and FSP samples during etching. The ECAP and FSP samples were observed by optical microscope (Leica 020-520.008 DM/LM, Wetzlar, Germany) in normal mode. The metallography of other samples was observed by optical microscope in polarizer mode. The grain size of samples was calculated via linear intercept method by drawing a set of randomly positioned lines on metallographic images and counting the number of times that lines intersect grain boundaries, via the software Olympus AnalySIS Pro (Olympus Soft Imaging Solutions, Münster, Germany).

3.4.2 SEM analysis

In SEM (scanning electron microscope) characterization, the samples were cleaned in distilled water followed by pure ethanol. After drying, they were stuck on a small conductive platform coated with N650 planocarbon (Plano GmbH, Wetzlar, Germany). After totally drying of the N650 planocarbon, the samples were placed in a scanning electron microscope (SEM, TESCAN vega 3 SBU, Brno, Czech Republic). The distribution of precipitates in different Mg-Ag

alloys was observed in BSE (back-scattered electron) mode. The images with different magnification were taken to characterize the uniformity and quantity of second phases or precipitates in Mg-Ag alloys. The quantification of second phases or precipitates was obtained via ImageJ software (version 1.46r, Wayne Rasband, National Institute of Health, USA) by calculating the area ratio of them in SEM images.

3.4.3 X-ray Diffraction

Mg-Ag alloys were grinded on Hermes sandpapers to ensure that the surface is flat. The types of phases were confirmed by Bruker X-ray diffraction (XRD) system (Bruker AXS Microanalysis GmbH, Berlin, Germany). Cu tube with 1.5418 [Å] was applied. The 2θ ranged from 20 to 80º. The movement of each step was 0.01º with duration of 0.5 s.

3.5 Mechanical analysis

3.5.1 Hardness measurements

All of the samples were embedded into Demotec 30 for hardness measurement. They were grinded on sandpapers from the mesh P320 to P2500 to remove the deformation layers caused by cutting and to ensure the flatness. The measurements of hardness were carried out in HV5 mode (49.03 N load) on a micro-hardness tester (Emcotest Prüfmaschinen, Kuchl, Austria). At least five points of each sample were chosen to be measured to obtain a mean value.

3.5.2 Tensile tests

The as-cast, homogenization, and thermomechanically processed Mg-Ag alloys were machined to standard samples for tensile tests. The round tensile specimens of as-cast, homogenization, extrusion and extrusion+T4 alloys have a total length of 60 mm, a gauge length of 42 mm, a measuring length of 36 mm and a diameter of 6 mm. The flat tensile specimens of FSP and ECAP alloys have a total length of 23 mm, a gauge length of 15 mm, a measuring length of 12 mm, a width of 2 mm and a thickness of 1.5 mm. The flat tensile specimens of rolling alloys have a total length of 165 mm, a gauge length of 75 mm, a measuring length of 50 mm, a width of 12.5 mm and a thickness of 1.8 mm. The standard deviation is 0.1 mm. The tensile tests of samples (n=5) except for the FSP and ECAP samples were conducted on a Zwick-Roell Universal Testing Machine Z050 (Zwick-Roell, Ulm, Germany). The preloading force was 2 MPa and the strain rate was 0.001/s. The tensile tests of FSP and ECAP samples (n=5) were carried out on a Zwick-Roell Testing Machine M10 (Zwick-Roell, Ulm, Germany) with a strain rate 0.001/s. Fiedler-LASER was applied to measure the distance during the tensile tests. The

maximum force loading of this machine was 5 kN.

3.6 Degradation behavior

3.6.1 The pH, osmolality and degradation rate

An optimized *in vitro* test setup was applied for the immersion tests [69, 177]. The samples were weight using a precise electronic scale (SCALTEC Scaltec SBA32, Göttingen, Germany) before immersion tests followed by sterilization in solution (70% ethanol and 30% double distilled water) for 30 min in ultrasonic bath (Sonorex RK 510S, Bandelin, Berlin, Germany). The samples were placed in multi-well plates until dry. The plates with samples were filled with cell culture medium (CCM), Dulbecco's modified Eagle's medium (DMEM) DMEM-Glutamax™ (Life Technologies™, Darmstadt, Germany) with 10% FBS (Fetal Bovine Serum, PAA laboratories, Linz, Austria) according to the weight of the samples (0.2 g/mL). The DMEM is extensively used for *in vitro* biocompatibility assays, as it is a culture medium suitable for the growth of most cell types, including osteoblasts, fibroblasts and tumour cells, in many different species, such as human, mouse and rabbit [178]. Cell culture conditions (5% CO_2, 20% O_2, 37°C and 97% rH (relative humidity)) in the CO_2 humidified incubator (Thermo Scientific Heraeus BBD 6220, Langenselbold, Germany) were applied for the immersion tests. The medium was changed by fresh one after 48 and 120 hours. The immersion tests continued for 7 days. All the operations above were performed in a sterile environment. The pH and osmolality of the replaced medium were measured via a pH meter (Sentron ArgusX, Roden, Netherlands) and an osmometer (Gonotec 030-D, Berlin, Germany), respectively. The degradation products on samples were removed by chromic acid (Sigma-Aldrich Chemie, Taufkirchen, Germany) solution (180 g/L in distilled water). After that, the samples were rinsed in double distilled water and pure ethanol and then put in a vacuum box (P<200 mbar, 37°C) (Salvis Lab Vacucenter, Salvis AG, Rotkreuz, Switzerland) for 30 min. The weight of samples was measured again after the removal of degradation products.

The mean degradation rate (MDR) was calculated according to the relation [179]:

$$\mathrm{MDR} = \frac{8.76 \times 10^4 \cdot \Delta g}{A \cdot t \cdot \rho} \qquad \text{Eq. 3.2}$$

where Δg, A, t and ρ stand for weight loss (g), surface area (cm^2), time (h) and density of Mg-Ag alloys, respectively. The densities were confirmed by buoyancy in pure ethanol according to

Archimedes' principle.

3.6.2 Morphology analysis

The morphologies of samples after immersion tests were characterized by TESCAN scanning electron microscope (SEM) in secondary electron (SE) mode after the removal of degradation products by chromic acid (180 g/L in distilled water).

3.7 Cytocompatibility tests

3.7.1 MTT assay

Human primary osteoblasts were selected for cytotoxicity evaluation considering the application of Mg-Ag alloys as bone implant materials. The human primary osteoblasts came from patients undergoing total hip arthroplasty (Schön Klinikum Eilbek, Hamburg, Germany) with local ethical committee agreement. The human primary osteoblasts were cultured in DMEM GlutaMAX™ (Dulbecco's modified Eagle's medium, Life Technologies™) with 10% FBS (Fetal Bovine Serum, PAA laboratories, Linz, Austria). The pure Mg, extruded Q6, extruded Q8, extruded+T4 Q6 and extruded+T4 Q8 discs were sterilized ultrasonically in 70% ethanol solution for 30 min. Extracts of pure Mg and Mg-Ag alloys for the MTT assay were prepared by immersing samples into CCM (0.2 g/mL) for 3 days under cell culture conditions and filtered (0.2 μm). The concentrations of Mg, calcium (Ca) and Ag in the extracts were measured via inductively coupled plasma mass spectrometry (ICP-MS; Agilent 7700x ICP-MS, Waldbronn, Germany) at GALAB Laboratories in Hamburg in Germany. The extracts were further characterized by measuring their pH and osmolality at room temperature using an ArgusX pH meter (Sentron, Roden, Netherlands) and a Gonotec 030-D cryoscopic osmometer (Gonotec, Berlin, Germany), respectively. A 50 μL aliquot of CCM containing 2,000 human primary osteoblasts was seeded into each hole of 96-well plates. These plates were transferred into incubator and kept for 24 hours to ensure that the human primary osteoblasts attached to the bottom. The 10% and 20% concentration extracts were prepared by adding CCM. Then, the old CCM in 96-well plates was replaced with fresh CCM (control group), primary extracts (100%), low concentration extracts (10% and 20%) (n=6 for each extract). Three days later, 10 μL 3-(4,5-dimethylthiazol-2-yl)-2,5-diphenyl-tetrazolium bromide solution (MTT; Sigma-Aldrich, Steinheim, Germany) was added into each well. The 96-well plates were incubated for 4 hours. Then, 100 μL SDS (sodium dodecyl sulfate)-lysis buffer (Sigma-Aldrich Co. LLC, Steinheim, Germany) was filled into each well. The multi-well plates were incubated overnight. Finally, the values were measured using an ELISA

multi-well plate reader (Tecan, Maennedorf, Switzerland) and the background value was subtracted.

3.7.2 Live/Dead staining and adhesion tests

In Live/Dead staining, the pure Mg, extruded Q6, extruded Q8, extruded+T4 Q6 and extruded+T4 Q8 discs were placed in 12-well plates after the discs incubated in CCM under the cell culture conditions for 24 hours. A total of 10^5 human primary osteoblasts were seeded on the surface of each disc. To ensure that the human primary osteoblasts attached to the surface, the seeded samples were kept in the incubator for 30 min. Then, the 12-well plates were slowly filled with 3 mL of fresh CCM in each well. The cells were cultured for 9 days. The CCM was changed by fresh one every 3 days. The pH and osmolality of the replaced medium were measured. Live/Dead staining was conducted every 3 days. The discs were washed gently in sterilized and distilled water and transferred into wells filled with LIVE/DEAD® Viability/Cytotoxicity Kit (Molecular Probes, Eugene, USA) according to the manufacturer's protocol. After incubation for 20 min, the distribution and viability of human primary osteoblasts on the pure Mg and Mg-Ag discs were observed via fluorescent microscope (Nikon ECLIPSE Ti-S, Tokyo, Japan).

In cell adhesion tests, the procedures to prepare SEM samples with human primary osteoblasts were as follows: (1) fixation in 2.5% glutaraldehyde solution in buffer (Sigma-Aldrich Co. LLC, Steinheim, Germany) for 2 hours; (2) staining in 1% osmium tetroxide (Sigma-Aldrich Co. LLC, Steinheim, Germany) for 30 min; (3) dehydration for 1 hour using increasing concentrations of 2-propanol (EMSURE®, Darmstadt, Germany) (20%, 40%, 60%, 80% and 100%) and (4) critical point drying (CPD, Leica EM CPD030, Bal-TEC AG, Balzers, Liechtenstein). Then, the samples were placed on a SEM sample holder coated with N650 planocarbon (Plano GmbH, Wetzlar, Germany) until dry. The samples with cells were observed via scanning electron microscope (SEM).

3.8 Mineralization assay and DAPI staining

As biomaterials, Mg-Ag alloys should meet the cytocompatibility requirements. However, if the Mg-Ag alloys were applied as bone implant materials, the mineralization behavior of corresponding cells on Mg-Ag alloys should be evaluated. Biomineralization by cells plays an important role in the reconstruction of bone tissues.

HUCPV (human umbilical cord perivascular) cells and human primary osteoblasts which were used in mineralization assay and DAPI staining were isolated from the human umbilical cord and the replaced femoral head of the hip joint, respectively, with the permission of local ethical committee. The α-MEM (Eagle's minimal essential medium, Life Technologies™) with 15% SC-FBS (Stemcell technologies, Vancouver, Canada) and DMEM GlutaMAX™ with 10% FBS were used to culture HUCPV cells and human primary osteoblasts, respectively. Pure Mg, extruded+T4 Q6 and extruded+T4 Q8 discs were put into multi-well plates which were coated with agarose. They were preincubated for 24 h in CCM. The pure Mg discs and the wells with only cells were set as positive control groups to determine the formation of hydroxyapatite (HA). A total of 10^5 human primary osteoblasts or 5×10^4 HUCPV cells were seeded in the wells or on the surface of discs. Each well was filled with 3 mL CCM and the medium was changed by fresh one every 3 days. The cells were cultured for 3 weeks. In mineralization assay, the staining was conducted via OsteoImage™ Mineralization Assay (Lonza, MD, USA) followed by DAPI staining every week.

Before staining, the discs were washed gently in PBS (phosphate buffered saline) and put into empty wells. 1 mL 3.7% formaldehyde was added into the well with Mg-Ag disc or control group. The Mg-Ag discs and control groups were kept for 15 min in formaldehyde followed by rinsing gently in 1 mL diluted Lonza wash buffer (1:10). Then, the Mg-Ag discs and control groups were stained in 0.5 mL diluted staining reagent (1:100) at room temperature. To avoid light interference on staining, the multi-well plates were covered with aluminum foil and kept for 30 min. After the diluted staining reagent was removed, the discs and control groups was washed 3 times using diluted wash buffer and kept for 5 min at the third time. After the new diluted wash buffer was added into wells, the mineralization was characterized via a fluorescence microscope (Nikon ECLIPSE Ti-S, Tokyo, Japan). The Mg-Ag discs and control groups were rinsed in PBS and immersed by 1 mL DAPI staining solution in each well. The samples were kept for 15 min at 37°C in the dark. Then, the DAPI staining solution was replaced by fresh PBS. The images of cells and in situ mineralization were recorded via fluorescence microscope.

3.9 Antibacterial tests

The antibacterial tests were conducted in the Institute for Bioprocessing and Analytical Measurement Techniques e.V. (iba) in Heilbad Heiligenstadt with the help of technician Juliane Zirm.

3.9.1 Bacteria preparation

The biofilm tests were conducted in a bioreactor system (BioFlo®/CelliGen® 115 (New Brunswick™, Eppendorf AG, New Brunswick, USA) which provided a circumstance for bacterial growth and a chance of initial biofilm formation on discs as shown in Fig. 3.14. This dynamic system had a cross-flow condition in the chambers, which ensured that the bacteria went through the surfaces of the discs. The flow rate of the medium in chamber was 0.3 mL/min. These conditions allow the possibility of initial biofilm formation on the discs [180]. During the running time of 15 hours, the temperature and pH were 37°C and 7.2, respectively. All the parameters mentioned above were controlled by the bioreactor system. Reference discs (titanium (Ti)) were always used as an internal control for the tests. The pure Mg, extruded Q6, extruded Q8, extruded+T4 Q6 and extruded+T4 Q8 discs were treated with 25.0 kGy gamma sterilization (BBF Sterilisationsservice GmbH, Kernen, Germany) before the biofilm tests [179]. The whole test was performed in a microaerophilic and sterilized environment to ensure bacterial activity. Bacteria culture medium (BCM) is nutrient broth (pH=7.2) which consisted of 3 g meat extract, 5 g peptone (Sigma-Aldrich Co. LLC, Steinheim, Germany) and 1 L distilled water. Phosphate buffered saline (PBS, pH=7.4) was prepared with 8 g NaCl, 0.2 g KCl, 1.47 g Na_2HPO_4, 0.24 g KH_2PO_4 (Sigma-Aldrich Co. LLC, Steinheim, Germany) and 1 L double-distilled water.

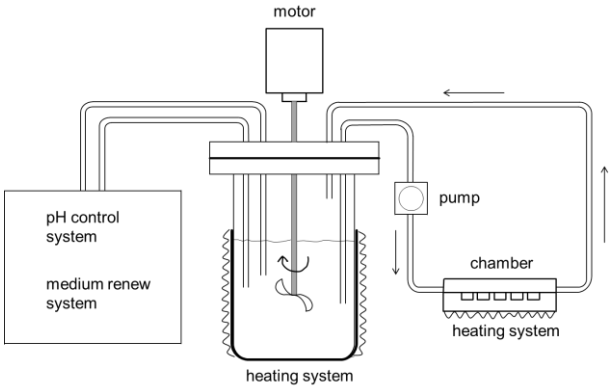

Fig. 3.14: Schematic illustration of bioreactor system (*reproduced with permission from HINDAWI [181]*).

Staphylococcus aureus (*S. aureus*, DSM no. 20231) and *Staphylococcus epidermidis* (*S. epidermidis*, DSM no. 3269) were used in the biofilm tests. These bacteria are commonly found in implant-associated orthopedic infections or osteomyelitis [82, 87, 182, 183], although there are contentions about which is the most common bacteria isolated from clinical infections,

especially implant-associated infections [83, 86, 184]. The bacteria were provided by the Leibniz Institute DSMZ-German Collection of Microorganisms and Cell Cultures in Germany. After the bacteria were cultured overnight, they were mixed and imported into the bioreactor system after checking their viability. The density and ratio of the mixed bacteria in medium were 10^6 /mL and 1:1, respectively.

3.9.2 Biofilm assay and bacterial viability

After the bioreactor system ran for 15 hours, all of the discs were removed from the chamber and labeled by adding LIVE/DEAD® BacLight™ Bacterial Viability Kit (Thermo Fisher Scientific Inc. (Life Technologies), Eugene, USA). The discs were observed by confocal laser scanning microscope (CLSM, LSM 710, Carl Zeiss Microscopy GmbH, Jena, Germany). The images of the whole surface and the local details of the discs were taken by CLSM. The other discs (n=12 for each type of sample) were rinsed gently in distilled water, placed in glass bottles with PBS and transferred to an ultrasonic bath (Sonorex Super 10P, BANDELIN electronic GmbH & Co. KG, Berlin, Germany). The bacteria were removed from the surfaces of the discs by a plastic scraper under sonication. The PBS solutions containing bacteria were diluted, placed on a counting chamber and counted using a fluorescence microscope (BX51, Olympus Optical Co. (Europa) GmbH, Hamburg, Germany).

3.9.3 Surface and morphology analysis

The pretreatment procedures of the samples with bacteria were the same with that in adhesion tests above. The surface condition of the discs was observed by SEM. Three-dimensional (3-D) images were merged using three SEM images with different tilt angles (0°, 7° and 15°) before and after the removal of degradation products.

3.10 Degradation environment

The degradation behavior was analyzed using the extruded Q6, extruded Q8, extruded+T4 Q6, extruded+T4 Q8, extruded+T6 Q6, extruded+T6 Q8, and nine kinds of modified HBSS solutions in physiological conditions. Aiming at mimicking the buffering capability of body fluid, the main inorganic substances and fetal bovine serum were added into HBSS. From solution 1 to solution 7, the composition approached the main composition of DMEM with 10% FBS, gradually. The purpose is to reveal the role of major inorganic substances and the influence of proteins on the degradation of Mg-Ag alloys. The mean degradation rates were calculated according to Eq. 3.2. The corresponding degradation products and extracts were characterized.

3.10.1 Solution preparation and immersion tests

Nine kinds of solutions were prepared as displayed in Table 3.2. 1% Penicillin/Streptomycin (P/S) was added into these solutions to avoid bacterial contamination afterwards. The solution 7 has a similar inorganic composition and proteins compared to DMEM with 10% FBS (Table 3.2 and 3.3). The pH and osmolality of solutions in cell culture conditions (5% CO_2, 20% O_2, 37°C and 97% rH (relative humidity)) were characterized by a ArgusX pH Meter (Sentron, Roden, Netherlands) and a Gonotec 030-D cryoscopic osmometer (Gonotec, Berlin, Germany), respectively. The extruded Q6, extruded Q8, extruded+T4 Q6, extruded+T4 Q8, extruded+T6 Q6 and extruded+T6 Q8 discs (n=3) were sterilized in 70% ethanol solution for 30 min in ultrasonic bath. They were transferred into clean bench and put in multi-well plates which were filled with solutions. The multi-well plates were kept in cell culture conditions for 7 days in the immersion tests. After 48 and 120 hours, the extracts were obtained to measure their pH and osmolality and replaced by fresh solutions. When the immersion tests were finished, the discs were rinsed in distilled water followed by pure ethanol for several seconds and kept in vacuum box at 37°C for 30 min until dry. Then, the images of discs were taken by optical microscope (Leica WILD M3Z, Heerbrugg, Switzerland). Degradation products of each disc were removed by 5 mL chromic acid (180 g/L in distilled water). The immersion time of discs in chromic acid was determined by the thickness of degradation products. After the removal of degradation products, the morphologies of discs were characterized by SEM. The weight of discs was obtained via a precision electronic scale (Scaltec SBA32, Goettingen, Germany) before sterilization and after the removal of degradation products. The mean degradation rates were calculated according to the Eq. 3.2.

Table 3.2: The solution composition in the immersion tests.

Solutions	Composition
1	HBSS + 10% FBS + 39.9 mM $NaHCO_3$
2	HBSS + 10% FBS + 1.8 mM $CaCl_2 \cdot 2H_2O$
3	HBSS + 10% FBS + 39.9 mM $NaHCO_3$ + 1.8 mM $CaCl_2 \cdot 2H_2O$
4	HBSS + 10% FBS + 0.8 mM $MgSO_4 \cdot 7H_2O$
5	HBSS + 10% FBS + 39.9 mM $NaHCO_3$ + 0.8 mM $MgSO_4 \cdot 7H_2O$
6	HBSS + 10% FBS + 1.8 mM $CaCl_2 \cdot 2H_2O$ + 0.8 mM $MgSO_4 \cdot 7H_2O$
7	HBSS + 10% FBS + 39.9 mM $NaHCO_3$ + 1.8 mM $CaCl_2 \cdot 2H_2O$ + 0.8 mM $MgSO_4 \cdot 7H_2O$
8	HBSS + 10% FBS

9	HBSS

Table 3.3: The inorganic composition in mM of HBSS and DMEM (*n=1 or 2).

Solutions	**K^+**	**Ca^{2+}**	**Na^+**	**Mg^{2+}**	***$H_nPO_4^{(3-n)-}$**	**Cl^-**	**HCO^{3-}**	**SO_4^{2-}**
HBSS	5.8	-	142.4	-	0.8	143.3	4.2	-
DMEM	5.3	1.8	155.3	0.8	0.9	117.5	44.1	0.8

3.10.2 Analysis of degradation products and extracts

The degradation products were characterized by XRD in small angle mode (5º), EDS (Energy Dispersive X-ray Spectroscopy) and SEM in BSE mode to verify the chemical composition and elemental distribution. The XRD settings were 2θ (5º-85º), angle of generator (5º) and steps (0.01º and 0.5 s).

The extracts of each disc was centrifuged at 1500 rpm for 5 min (Hettich Zentrifugen Rotina 420, Tuttlingen, Germany) and filtrated through filter paper (0.2 µm). Dynamic light scattering (DLS, SPECTROLIGHT™ 300, Xtal Concepts, Hamburg, Germany) was applied to analyze the size of proteins in the extracts. The container was cleaned carefully using compressive nitrogen gas and filled with 10 µL extract. The settings of measurements were 10 s duration and 20 repetitions at least at 20°C. Diluted HNO_3 (10%, 0.5 mL) was added into extract (1 mL). The extract was kept for 2 hours at room temperature to identify the existence of silver metal.

3.11 Statistical analysis

Statistical difference of Vickers hardness values was determined by ANOVA (Kruskal-Wallis One Way Analysis of Variance on Ranks, with Dunn's post-hoc test against extruded magnesium as control) in Origin 9.0G (OriginLab Corporation, MA, USA). The Dunn's test is used to pinpoint which specific means are significant from the others, after significant difference in means is confirmed by ANOVA. Statistical analysis of the data in cytocompatibility and antibacterial parts was also performed by ANOVA with the Tukey's post-hoc test. The Tukey's test is used for larger numbers of pairwise comparisons.

Statistical analysis of correlations in discussion part was conducted by SigmaPlot (Version 13, Systat Software, Erkrath, Germany) to obtain Pearson correlation coefficient (PCC). In the statistics, the PCC reflects the linear correlation between two variables (X and Y), which is a value between +1 and −1. The "1" is total positive linear correlation, "0" is no linear correlation,

and "−1" is total negative linear correlation. The graphs presented the results as the mean values with the standard deviation (SD) as the error bars.

4. Results

4.1 Microstructure

The microstructure of Mg-Ag alloys has big influence on mechanical properties and degradation behavior. In this part, to reveal the microstructure influences to mechanical properties and degradation behavior, different microstructures were prepared by casting, heat treatments and several thermomechanical processing including hot extrusion, ECAP, FSP and the rolling with subsequent annealing. In the annealing procedure, a series of temperatures and time were applied to observe the microstructure changes. The grain sizes were measured and the second phases/precipitates were identified and calculated.

4.1.1 Grain size

The dendrites can be observed from the as cast Q6, Q8 and Q10 (Fig. 4.1). With the increase of silver in as cast Mg-Ag alloys, the grains became smaller. In the as cast Q6 and Q8, the microstructures showed irregular columnar grains. The as cast Q10 consisted of more homogeneous equiaxial grains, which was related to the silver content and casting procedures. Homogenization treatment at 450°C (Q6 and Q8) and 460°C (Q10) for 8 hours at least made all second phases dissolved into matrix. After homogenization treatment, the grain shape of homogenized Q6 and Q8 showed microstructure inheritance from the as cast Q6 and Q8, respectively. However, the homogenized Q10 had obvious grain growth called secondary recrystallization, since a higher solvus temperature was applied to ensure complete dissolution of second phases.

Hot extrusion made the microstructures of Mg-Ag alloys even more homogeneous than the as cast and homogenized Mg-Ag alloys (Fig. 4.1). There were many small equiaxed grains and precipitates existing near the grain boundaries after recrystallization. The low temperature and high strain ratio during extrusion promoted precipitation at the grain boundaries. These precipitates in the extruded Mg-Ag alloys were more abundant and larger when silver content was higher. Affected by the silver content and hot extrusion parameters, the extruded Q8 and Q10 got finer grains than the extruded Q6. On the base of the extruded alloys, T4 treatments of the extruded Q6, Q8 and Q10 at 430°C eliminated these precipitates which dissolved into the matrix again. For Q10, a temperature of 430°C was not sufficient to dissolve all precipitates into the matrix in 16 hours, so a higher solvus temperature at 450°C was applied. This led in turn to an increase of grain size. After T4 treatments, the alloy with higher silver content obtained larger

grains since the T4 temperature was closer to the melting temperature. However, they still have equiaxed grains which are smaller than the grains of the as cast and homogenized Mg-Ag alloys (Fig. 4.4). The metallography of extruded pure Mg was shown, which was set as a reference for Mg-Ag alloys (Fig. 4.1).

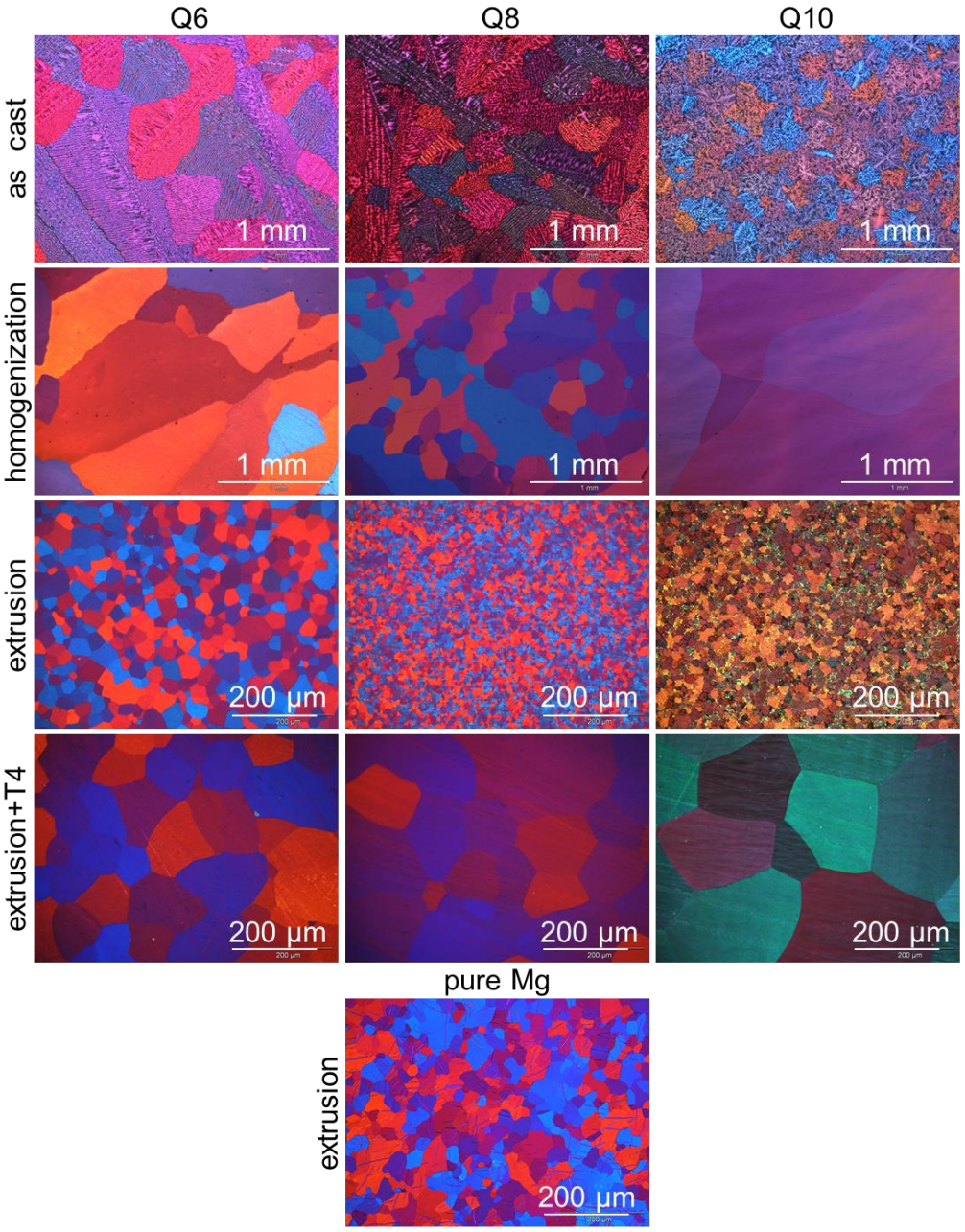

Fig. 4.1: Polarized optical metallography of Q6, Q8 and Q10 after casting, homogenization, hot extrusion and extrusion+T4. The polarized optical metallography of extruded pure Mg is set as a reference of Mg-Ag alloys.

After T4 treatments of the extruded Q6 and Q8 rods, the ECAP was carried out. The Q10 was not considered because of high degradation rate even after hot extrusion and T4. Ultrafine grains with less than 1 µm were obtained (Fig. 4.2). However, a high amount of precipitates in Q6 and Q8 also separated out and the precipitates increased with silver content. Some parts of the ECAP Q6 and ECAP Q8 had no full recrystallization because of inhomogeneous deformation. The grains in FSP Q6 and FSP Q8 were also pretty small but they were still bigger than that of the ECAP Q6 and ECAP Q8. However, no precipitates can be observed in the FSP Q6 and FSP Q8.

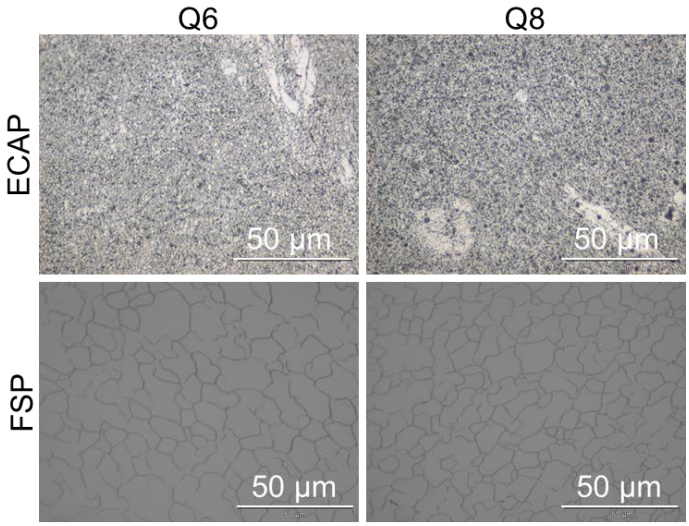

Fig. 4.2: Optical metallography of Q6 and Q8 after ECAP and FSP.

At 350 and 400°C, only Q6 was processed by the rolling, since the degradation rate of Q6 was already very fast in such condition. The Q8 and Q10 had much higher degradation rates if the rolling at such temperature was done. The rolling processing was carried out on the basis of homogenized Q6 and Q8 slices. As displayed in Fig. 4.3, the grains in the as rolled Q6 and annealed Q6 became bigger with the increase of temperature. At 450°C, the Q8 got slightly finer grains than the Q6. The grains in the as rolled Q6 and Q8 or annealed Q6 and Q8 were smaller than that in the corresponding extruded+T4 Q6 and Q8.

The summary of grain sizes of different Mg-Ag alloys compared to the extruded pure Mg is shown (Fig. 4.4). The ECAP Q6 and ECAP Q8 possess ultrafine grains and have the smallest grains than other Mg-Ag alloys. The FSP Q6, FSP Q8, extruded Q8 and extruded Q10 also have pretty small grains. The homogenized Q6, homogenized Q8 and homogenized Q10 have much bigger grains which range from 125 µm to 2.3 mm.

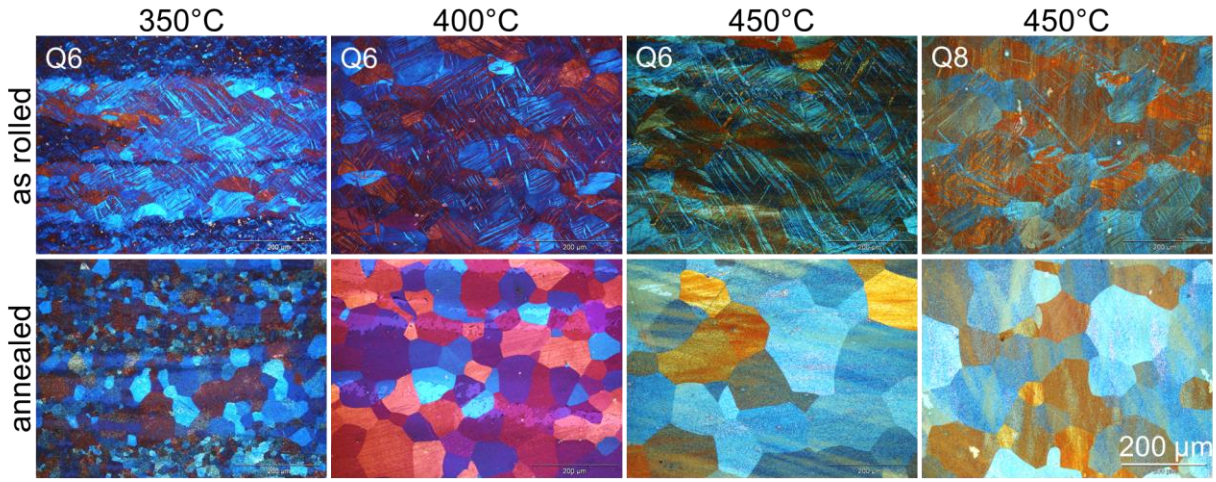

Fig. 4.3: Polarized optical metallography of Q6 and Q8 after rolling and general annealing for 30 min.

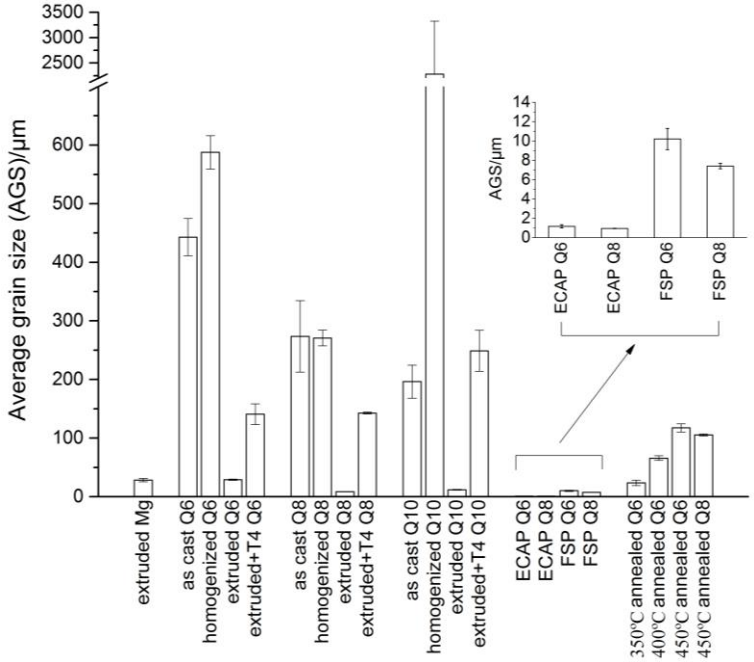

Fig. 4.4: Average grain size (AGS) of Q6, Q8 and Q10 after casting, solution treatments and thermomechanical processing compared to the extruded pure Mg.

In the short time annealing of the as rolled Q6 (Fig. 4.5 a), a full static recrystallization of Q6 rolled at 350°C finished after annealing for 20 s at 350 or 400°C. The grains grew larger with time during the short time annealing. The grains in Q6 rolled at 400°C had the same trend during the annealing at 350 or 400°C with time. However, the Q6 rolled at 400°C had low static recrystallization rate when the short time annealing was carried out at 350°C (Fig. 4.5 b). After 20 s, there were still twins and only partial static recrystallization occurred.

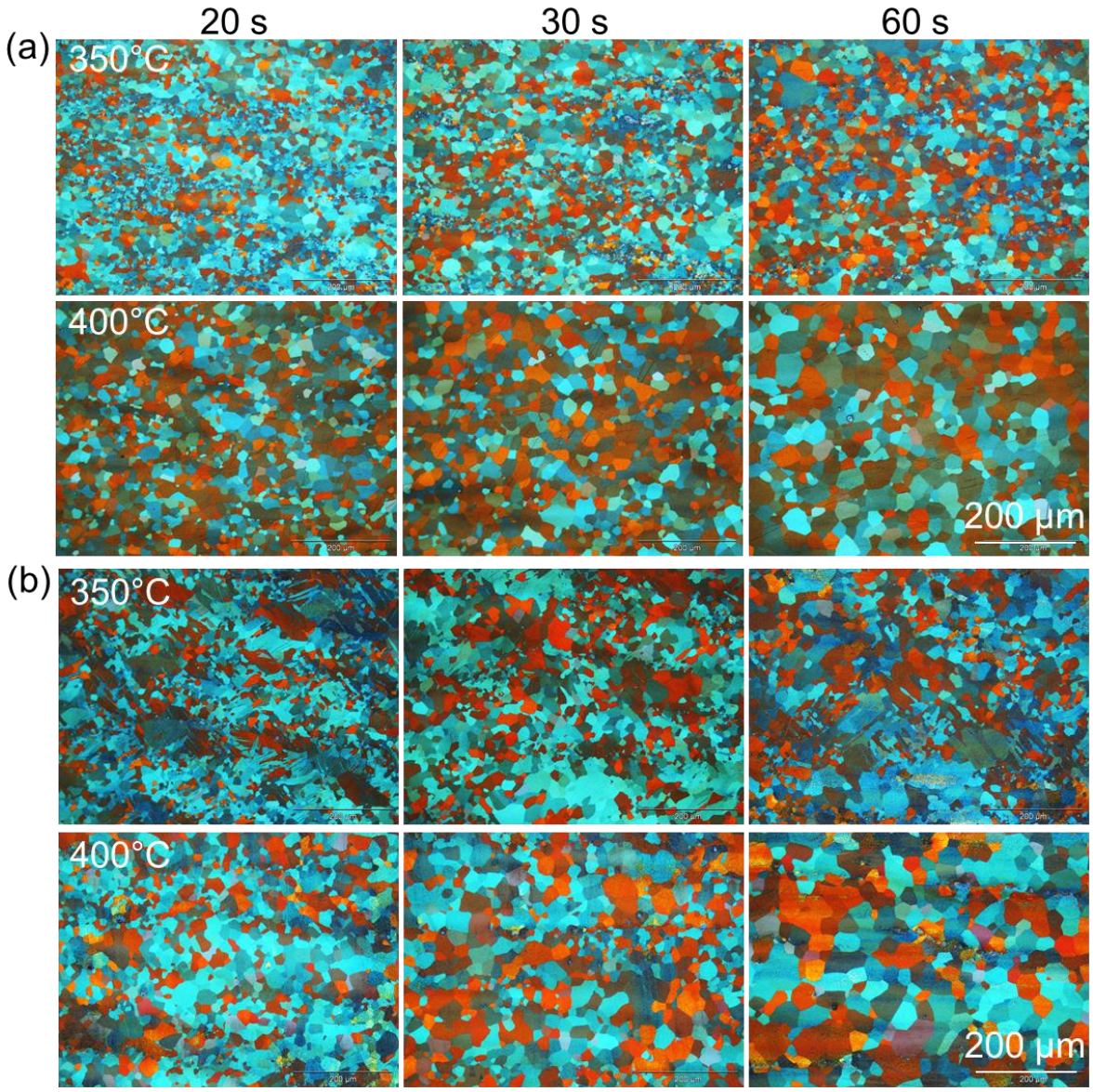

Fig. 4.5: Short time annealing of as rolled Q6. The Q6 rolled at 350°C (a) and the Q6 rolled at 400°C (b) were annealed at 350 or 400°C.

For the Q6 and Q8 rolled at 450°C (Fig. 4.6), the grain size decreased continuously with time in 60 s since the static recrystallization was ongoing when the annealing temperature was 400°C. There were still twins in these alloys even after annealing for 30 s. Only a partial static recrystallization in twins and grain boundaries happened. When the annealing temperature was 450°C, the recrystallization rate was faster. The grains of Q6 and Q8 increased with time. However, the recrystallization rate in Q8 was always slower than that in the Q6, no matter the annealing temperature was 400 or 450°C.

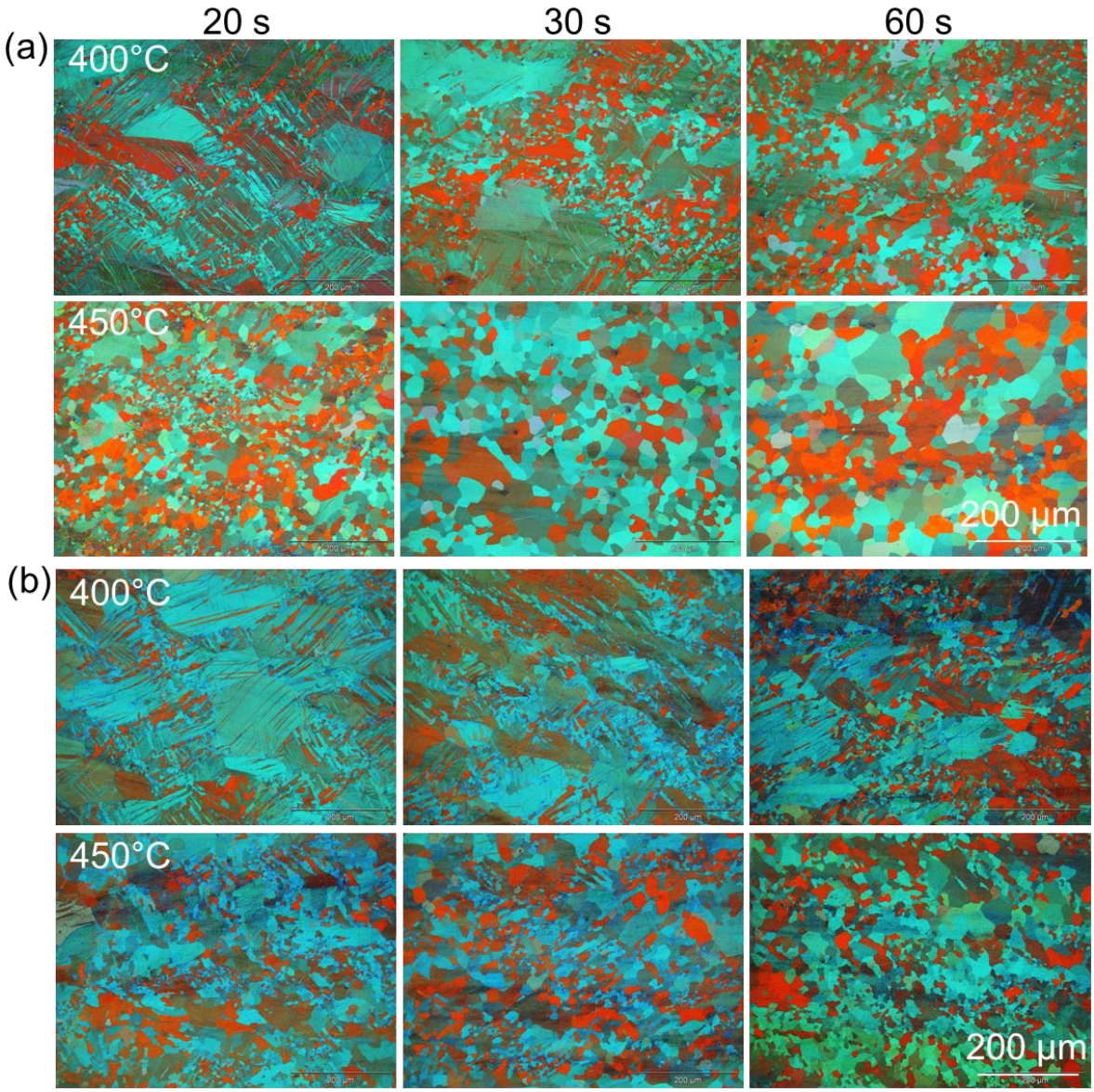

Fig. 4.6: Short time annealing of as rolled Q6 and Q8. The Q6 (a) and Q8 (b) rolled at 450°C were annealed at 400 or 450°C.

The grains of Q6 rolled at 350 or 400°C grew during short time annealing at 350 or 400°C from 20 to 60 s (Fig. 4.7a). The grains were larger when the Q6 was annealed at a higher temperature. However, the grains in the Q6 and Q8 rolled at 450°C were decreasing when the annealing temperature was 400°C (Fig. 4.7b). The static recrystallization was still ongoing in the annealing for 60 s. After general annealing for 30 min, the Q6 rolled at 400°C had obvious bigger grains than the one after short time annealing, rather than the Q6 rolled at 350°C. The grains of Q6 rolled at 350°C were inhomogeneous because the grains were restricted by precipitation. After general annealing at 450°C for 30 min, the Q6 and Q8 had much bigger

grains than the short time annealed alloys. The higher annealing temperature always results in larger grains in Q6 and Q8. Annealing at lower temperature than the rolling temperature caused a slower recrystallization rate.

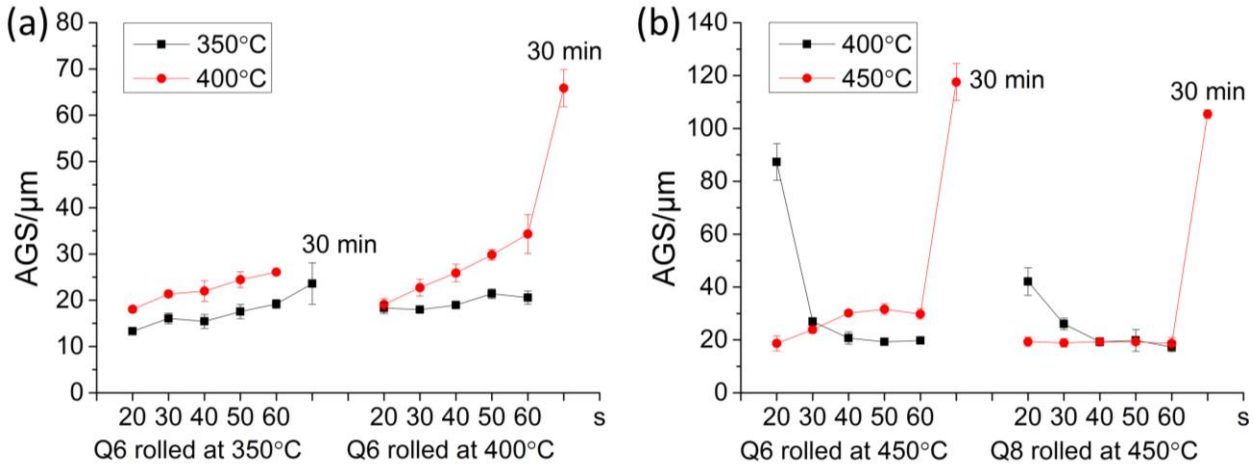

Fig. 4.7: Grain size variation during the short time annealing of Q6 rolled at 350 or 400°C (a), and Q6 and Q8 rolled at 450°C (b).

4.1.2 Second phases and precipitates

The as cast, extruded and ECAP alloys with high silver content obviously have a high amount of second phases or precipitates as well as the Q6 rolled at 350 and 400°C (Fig. 4.8, 4.9 and 4.10). The second phases exist in the dendrites of the as cast Q6, Q8 and Q10. The Q10 has some precipitates at the grain boundaries because of high silver content and low cooling rate after casting. The amount of second phases changed with the silver content. Homogenization eliminated all the second phases.

In the extruded Q6, only a few second phases can be observed along the grain boundaries. However, with the increase of silver content, more and more precipitates formed near the grain boundaries and even at the grains. These precipitates in the extruded Q8 and extruded Q10 were larger than that in the extruded Q6. After T4 treatments, nearly no precipitates can be observed in their SEM images.

In the ECAP processing (Fig. 4.9), many precipitates separated out since the temperature was lower than the corresponding solvus temperature of silver in magnesium. Many dislocations occurred and therefore promoted the formation of precipitates and recrystallization. However, the severe deformation and heat input via FSP induced a full and fast recrystallization in the

stirred zone. No precipitates can be seen in the FSP Q6 because of fast cooling rate. Only a few small precipitates formed at the grain boundaries of FSP Q8, even though there was a strong precipitation tendency.

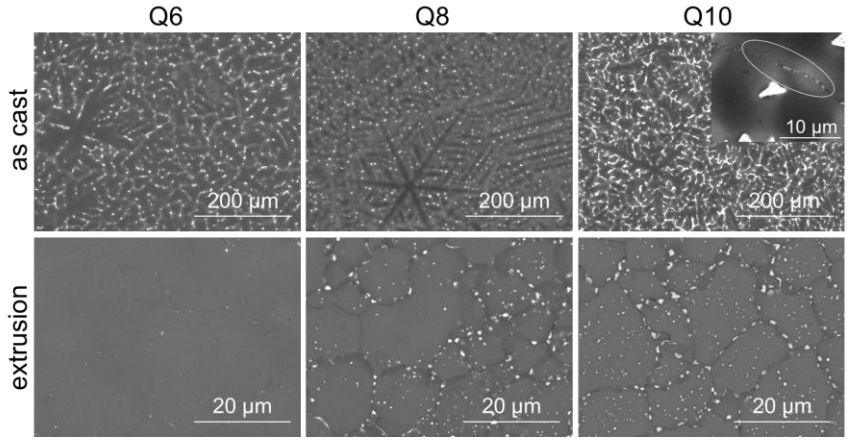

Fig. 4.8: Distribution of second phases and precipitates in the as cast and extruded Q6, Q8 and Q10.

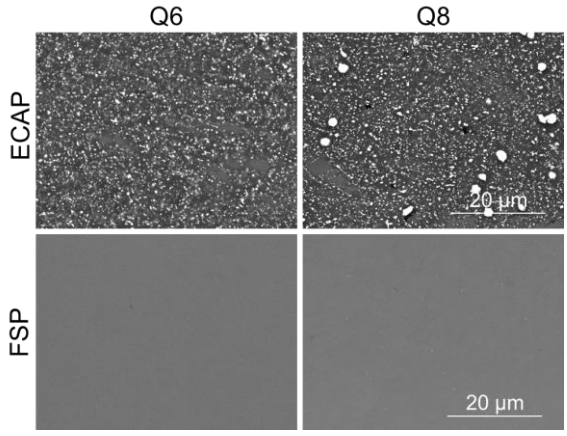

Fig. 4.9: Distribution of precipitation $Mg_{54}Ag_{17}$ in Q6 and Q8 after ECAP and FSP.

In Fig. 4.10 micrographs taken by scanning electron microscopy are listed to reveal the appearance and morphology of precipitates. Many precipitates exist in Q6 which was rolled and annealed at 350 or 400°C (Fig. 4.10a). The precipitates were separated out during the repeated rolling and annealing procedures. In Fig. 4.11, the precipitate strips distribute along the rolling direction, which means that the distribution of silver element is not homogeneous. The areas with precipitates are rich in silver. The precipitates in the Q6 rolled at 400°C are less compared to that in the Q6 rolled at 350°C. No precipitation was observed in the Q6 and Q8 which were rolled and annealed at 450°C (Fig. 4.10b).

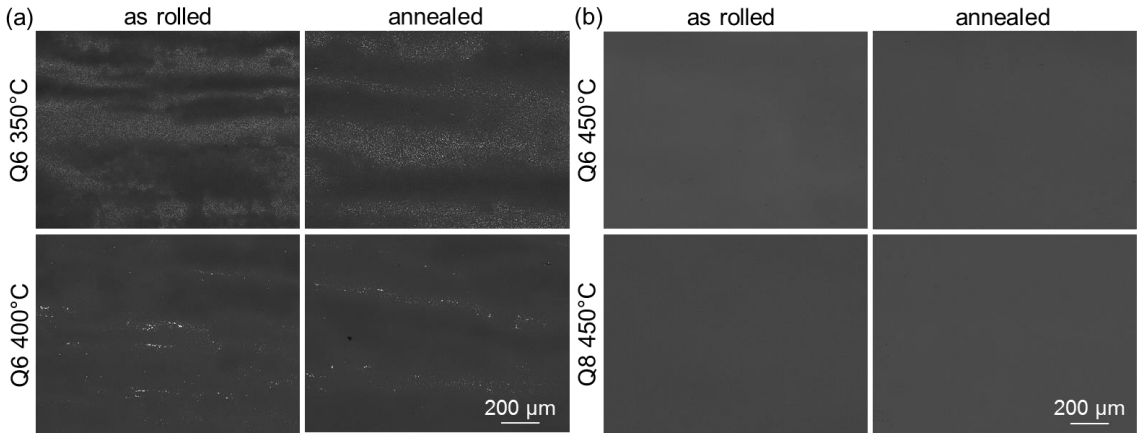

Fig. 4.10: SEM images of Q6 in BSE mode after rolling and annealing at 350 and 400°C for 30 min (a), SEM images of Q6 and Q8 in BSE mode after rolling and annealing at 450°C for 30 min (b).

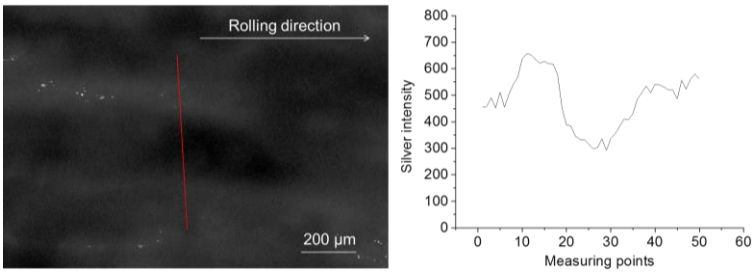

Fig. 4.11: Homogeneity analysis of silver element via line scanning of EDS in Q6 rolled at 350°C.

According to the XRD patterns in Fig. 4.12a, no second phases in these Mg-Ag alloys were detected by XRD. Only the α-Mg exists, since most of the silver dissolved into the matrix. However, we can determine that the second phases or precipitates mainly consist of $Mg_{54}Ag_{17}$ (Fig. 4.12b). Moreover, the type of second phases and precipitates is different from the one (Mg_4Ag) in the simulated Mg-Ag phase diagram.

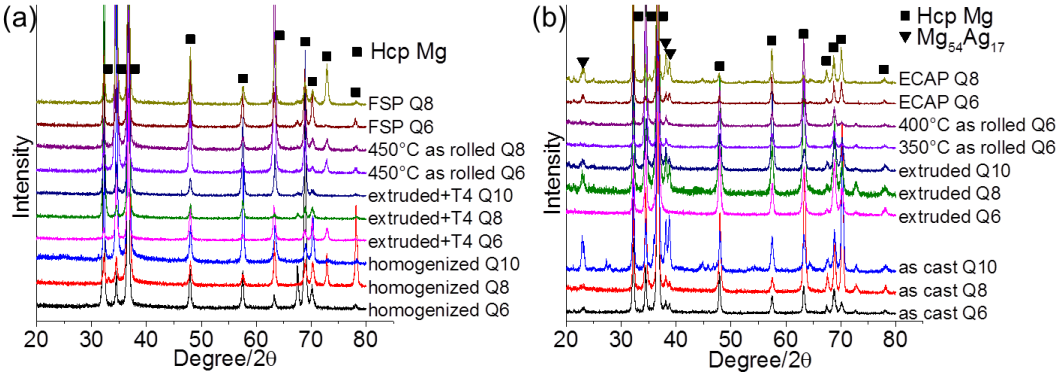

Fig. 4.12: XRD patterns of the Mg-Ag alloys without second phases (a) and the Mg-Ag alloys with second phases (b).

The amount of second phases or precipitates is shown in Fig. 4.13. The as cast Q10, ECAP Q6 and ECAP Q8 have more second phases or precipitates than the other Mg-Ag alloys. With the decrease of silver content or increase of rolling and annealing temperature, the quantity of second phases or precipitates decreased.

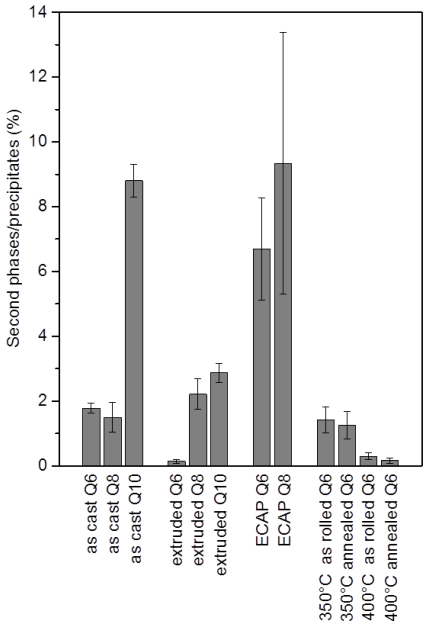

Fig. 4.13: Quantity of second phases or precipitates in Mg-Ag alloys after casting, hot extrusion, ECAP, and the rolling with subsequent annealing.

4.2 Mechanical properties

High mechanical strength and ductility are the requirements of Mg-Ag alloys as biodegradable implant materials. In this part, it is aimed to find out the relationships between microstructure and mechanical properties, to promote the mechanical properties. Vickers hardness, tensile properties and fracture surfaces were characterized and analyzed. Statistical analysis of hardness for the comparison of Mg-Ag alloys against pure Mg is listed. The changes of hardness with different annealing temperature and time are displayed.

4.2.1 Vickers hardness

The hardness values of Q6, Q8 and Q10 with different microstructures are displayed in Fig. 4.14. The hardness of the extruded pure Mg was set as a reference. The statistical values of hardness of different Mg-Ag alloys compared to the extruded pure Mg are shown in Table 4.1. Although the extruded pure Mg has fine grains, the hardness is still lower than that of the Mg-Ag alloys.

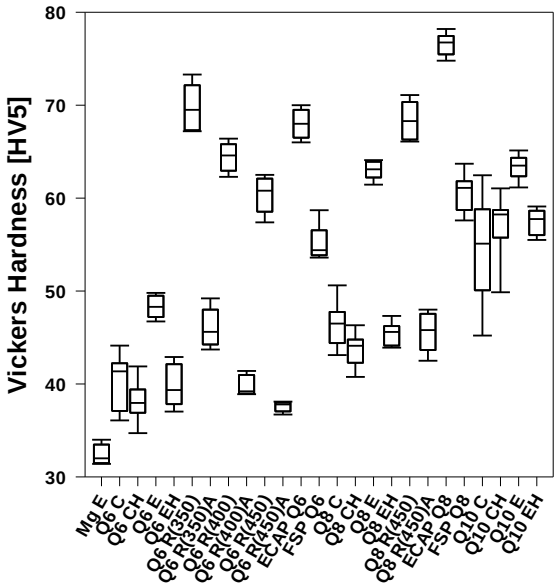

Fig. 4.14: Hardness of Q6, Q8 and Q10 after casting (C), homogenization (H), hot extrusion (E), rolling (R, with rolling temperature in brackets), annealing (A), ECAP and FSP.

Table 4.1: Statistical values for the comparison of Mg-Ag alloys against the extruded pure Mg. Not listed treatments did not show significant differences. Significance level: *** = $p<0.001$; ** = $p<0.01$; * = $p<0.05$.

Alloy and processing	Difference of ranks	Q-value	Significance level
ECAP Q8	178.00	5.789	***
350°C as rolled Q6	169.30	5.249	***
450°C as rolled Q8	166.90	5.175	***
ECAP Q6	165.90	5.144	***
400°C as rolled Q6	151.80	4.707	***
Extruded Q10	145.80	5.301	***
Extruded Q8	143.50	5.218	***
FSP Q8	127.75	4.154	***
450°C as rolled Q6	126.60	3.925	**
Homogenized Q10	113.35	4.121	***
Extruded + T4 Q10	112.83	3.669	**
As cast Q10	105.30	3.829	**
FSP Q6	104.00	3.225	*
Extruded Q6	85.60	3.112	*

The homogenized Q6, Q8 and Q10 have higher hardness values than the extruded pure Mg, which means that lattice distortion caused by dissolving of silver into matrix contributed to the increase of hardness. The as cast Q6, Q8 and Q10 also showed higher hardness than the extruded pure Mg, which resulted from second phases strengthens. The hardness of the as cast Mg-Ag alloys increased with the amount of second phases. The as cast Q10 has higher hardness than that of the as cast Q6 and Q8. Moreover, fine grains also contribute to the improvement of hardness. The FSP Q6 and Q8 have the similar hardness values with the as cast Q10. Hence, ECAP Q8 shows the highest hardness among all of the Mg-Ag alloys because of fine grains and many precipitates.

The as rolled Mg-Ag alloys have higher hardness than all of the annealed alloys because of work hardening. After general annealing for 30 min at the rolling temperature, the hardness of as rolled Q6 and Q8 dropped, obviously. Moreover, the hardness of the as rolled or annealed Q6 dropped with the increase of temperature, since the grains grew. Moreover, the hardness of annealed Mg-Ag alloys increased gradually with the increase of silver content. In total, the silver content and grain size influenced the hardness of annealed Mg-Ag alloys. The hardness values of as delivered materials decreased after solution treatment or annealing. All homogenization treatments led to the decrease of hardness, which resulted from grains enlargement and second phase elimination. To show these trends more clearly, selected thermomechanical states are depicted in Fig. 4.15.

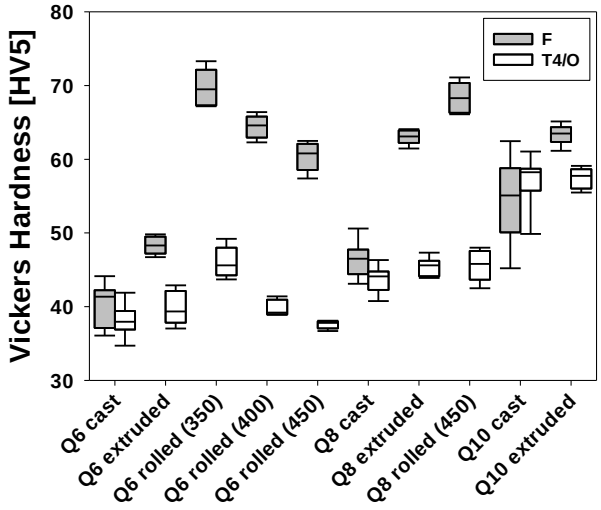

Fig. 4.15: Comparison of the hardness values in the as delivered (F) and solution treated/annealed (T4/O) state (denominations according to according to ASTM B275 [171]).

4.2.2 Hardness variation with annealing

The hardness of Mg-Ag alloys dropped gradually with the annealing time (Fig. 4.16). The general annealing for 30 min caused more obvious dropping of hardness than the short time annealing. However, the Q6 rolled at 350°C did not show this trend since the grains and precipitates were not homogeneous (Fig. 4.16a). The areas with finer grains and more precipitates have a higher hardness. The Mg-Ag alloys annealed at low temperature have higher hardness than that annealed at high temperature. The hardness shows substantial dropping after annealing at 450°C for 30 min (Fig. 4.16b). This is in accordance with the changes of grain size in short time annealing (Fig. 4.7).

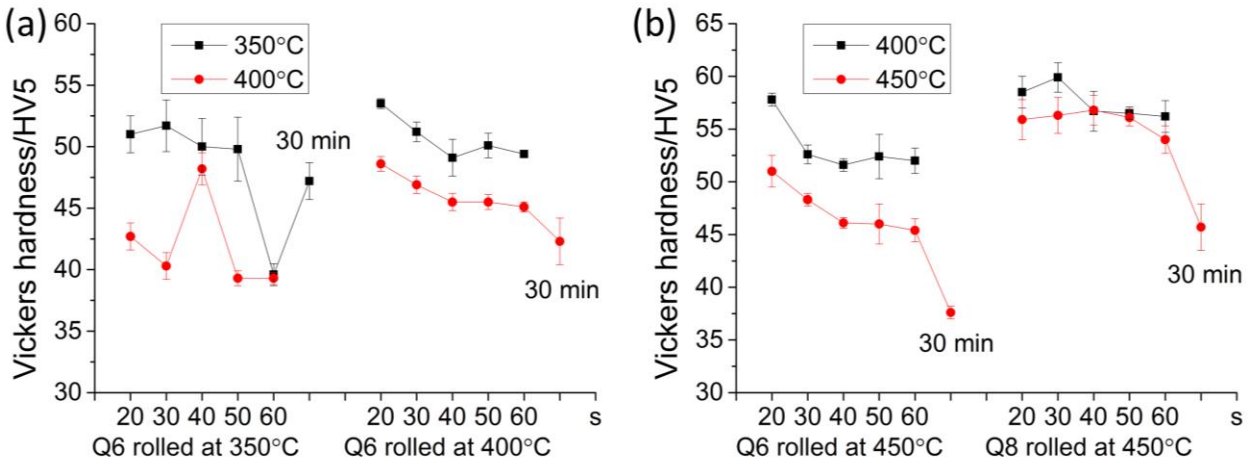

Fig. 4.16: Hardness variation of Q6 and Q8 during short time annealing. The Q6 rolled at 350 and 400°C was annealed at 350 and 400°C (a). The Q6 and Q8 rolled at 450°C were annealed at 400 and 450°C.

4.2.3 Tensile properties

The yield strength and ultimate strength of as cast Q6 and Q8 are not stable as well as the homogenized Q6 and Q8 (Fig. 4.17). The yield strengths of the as cast Q6, Q8 and Q10 has no obvious difference, but the as cast Q10 has a bit higher ultimate strength than the as cast Q6 and Q8. After homogenization, this trend is still observable. However, the dissolving of second phases deteriorated the yield strengths of Q6 and Q8.

After hot extrusion, the Mg-Ag alloys with higher silver content showed higher yield strength and ultimate strength. Fine grains and homogeneous distribution of precipitates in the extruded Mg-Ag alloys improved both yield strength and ultimate strength. After extrusion+T4 treatments,

there was only a small decrease of yield and ultimate strength of the extruded Q6 and Q8. After ECAP, the yield strength of Q6 was much highly improved. However, the yield strength of ECAP Q8 had obvious increase compared to the extruded+T4 Q8. It is still lower than that of the extruded Q8. The ultimate strength of ECAP Q8 is generally the same with that of the extruded+T4 Q8. The FSP Q6 has equivalent yield strength with the as cast Q6 and homogenized Q6, but its ultimate strength is higher than them. The FSP Q8 has showed slightly improved yield strength than the as cast Q8 and homogenized Q8. Its ultimate strength reached the same level with the ultimate strength of the extruded Q8. The thermomechanical processing, hot extrusion, extrusion+T4, ECAP, FSP and the rolling with subsequent annealing, enhanced the elongation of Q6 and Q8.

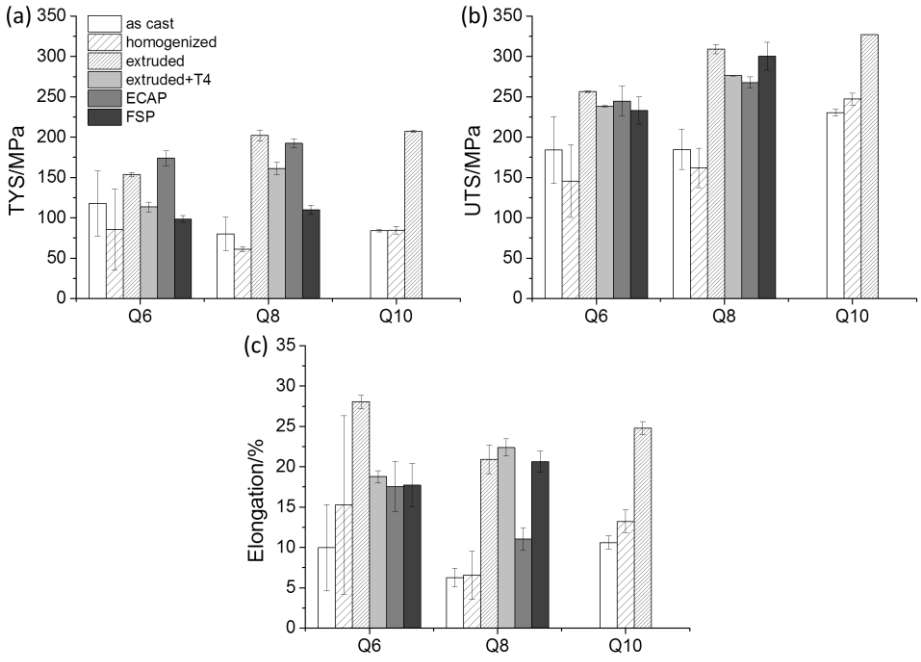

Fig. 4.17: Tensile properties of Q6, Q8 and Q10 after casting, homogenization and thermomechanical processing. The yield tensile strength (YTS), ultimate tensile strength (UTS) and elongation at break were displayed in (a), (b) and (c), respectively.

The fracture surfaces consist of many cleavages and dimples, where smaller grains induced smaller cleavages (Fig. 4.18). Most of the dimples distribute along the grain boundaries because of precipitates in that place. The precipitates exist in the dimples where a large number of dislocations plugged. Normally, the cracks formed and developed here during deformation. The small and big particles in SEM images are precipitates. Tear ridges are observed from the

fracture surfaces, so the fracture mode is quasi-cleavage fracture. The fracture surfaces of FSP Q6 and Q8 are consisted with many small cleavages and dimples. They are more homogeneous and smaller than that on the fracture surfaces of the extruded Q6 and Q8 alloys. No precipitates can be observed on the fracture surfaces of FSP Q6 and Q8 (Fig. 4.19).

The short time annealed Q6 and Q8 alloys obtained better tensile strength compared to the general annealed alloys (30 min), even though the ductility was sacrificed to some extent (Fig. 4.20). The yield strength after short time annealing is much higher that of the Q6 and Q8 alloys after general annealing. The changes of yield strength range from 66 to 84 MPa. The ultimate strength also increased compared to that of the general annealed alloys. The changes of ultimate strength are from 31 to 79 MPa. The 350°C rolled Q6 has a substantial dropping of elongation at break compared to the general annealed Q6. After short time annealing, the Q6 rolled at 400 and 450°C still have good elongation at break along both the rolling and transversal directions, as well as the Q8 rolled at 450°C.

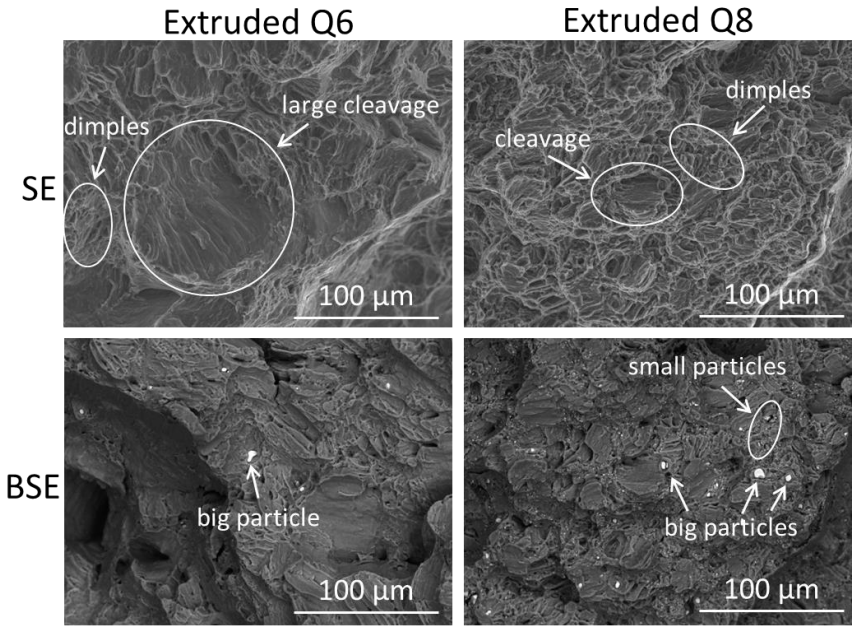

Fig. 4.18: Analysis of the fracture surfaces of extruded Q6 and Q8 after tensile tests.

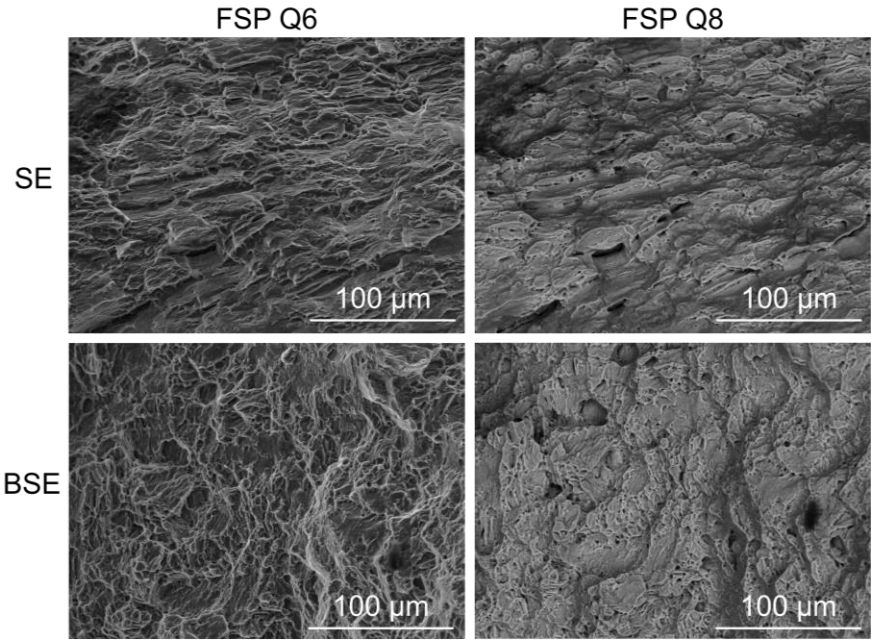

Fig. 4.19: Analysis of the fracture surfaces of FSP Q6 and Q8 after tensile tests.

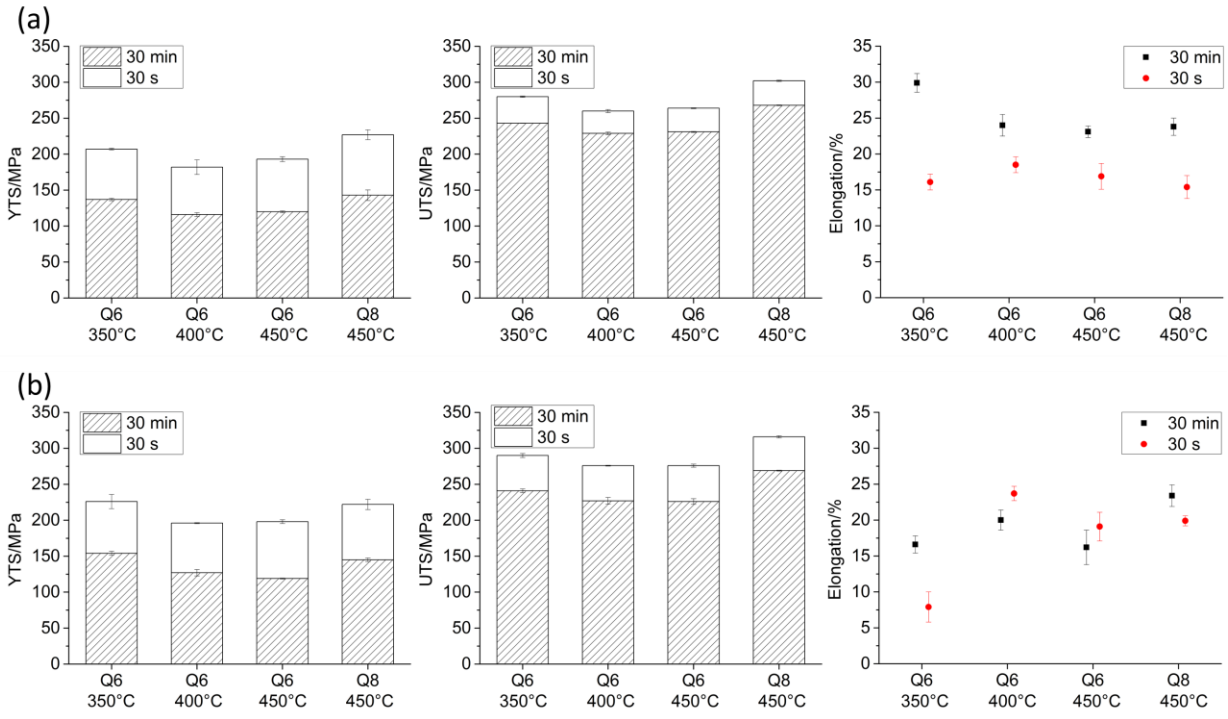

Fig. 4.20: Yield tensile strength, ultimate tensile strength and elongation of the as rolled Q6 and Q8 along rolling direction (a) and transversal direction (b) after annealing for 30 min and 30 s.

4.3 Degradation behavior

As biodegradable implant materials, Mg-Ag alloys should possess low enough degradation rate and homogeneous degradation morphology. Fast degradation rate and pitting can cause rapid loss of mechanical integrity. Moreover, fast degradation rate can result in relative high pH value and osmolality of the degradation environment, which is not conductive to the bone healing and the surrounding tissues. This part aims to find out the relationships between microstructure and degradation behavior including degradation rate and degradation morphology, to find out an ideal microstructure that can bring the satisfied degradation behavior.

4.3.1 The pH, osmolality and degradation rate

In the immersion tests, the pH values and osmolalities changed with time during the degradation procedure. The pH values indicated the concentration of OH^- ions and the osmolalities demonstrated the total ions in the immersion media. Both of them are important indicators to cells with respect to their viability.

In the first initial degradation, the pH values were high (Fig. 4.21a). Then, in most of the cases, the pH values had an increase because of increasing immersion time (48–72–168 hours), but generally a decrease was observed with time. For osmolality (Fig. 4.21b), it was more obvious, as in most of the cases the second value was lower than the first one, although the immersion time was longer. Overall, when the degradation rates of Mg-Ag alloys were fast, the pH and osmolality increments were generally high.

The degradation rates of Mg-Ag alloys are listed in Fig. 4.22. When the silver content was lower and less second phases or precipitates existed in Mg-Ag alloys, the mean degradation rate was lower. Homogenization, T4, FSP and rolling at high temperature brought low degradation rates to Q6 and Q8. The extruded Q6 also had low degradation rate instead of the extruded Q8 with many precipitates. Higher silver content caused more inhomogeneous distribution of silver in Mg-Ag alloys. The degradation rate of homogenized Q8 and homogenized Q10 was not stable. As cast Q6, Q8 and Q10 possess high degradation rates. The thermomechanical processing of ECAP and rolling at low temperature resulted in fast degradation rates of Q6 and Q8, as well as the hot extrusion of Q8 and Q10.

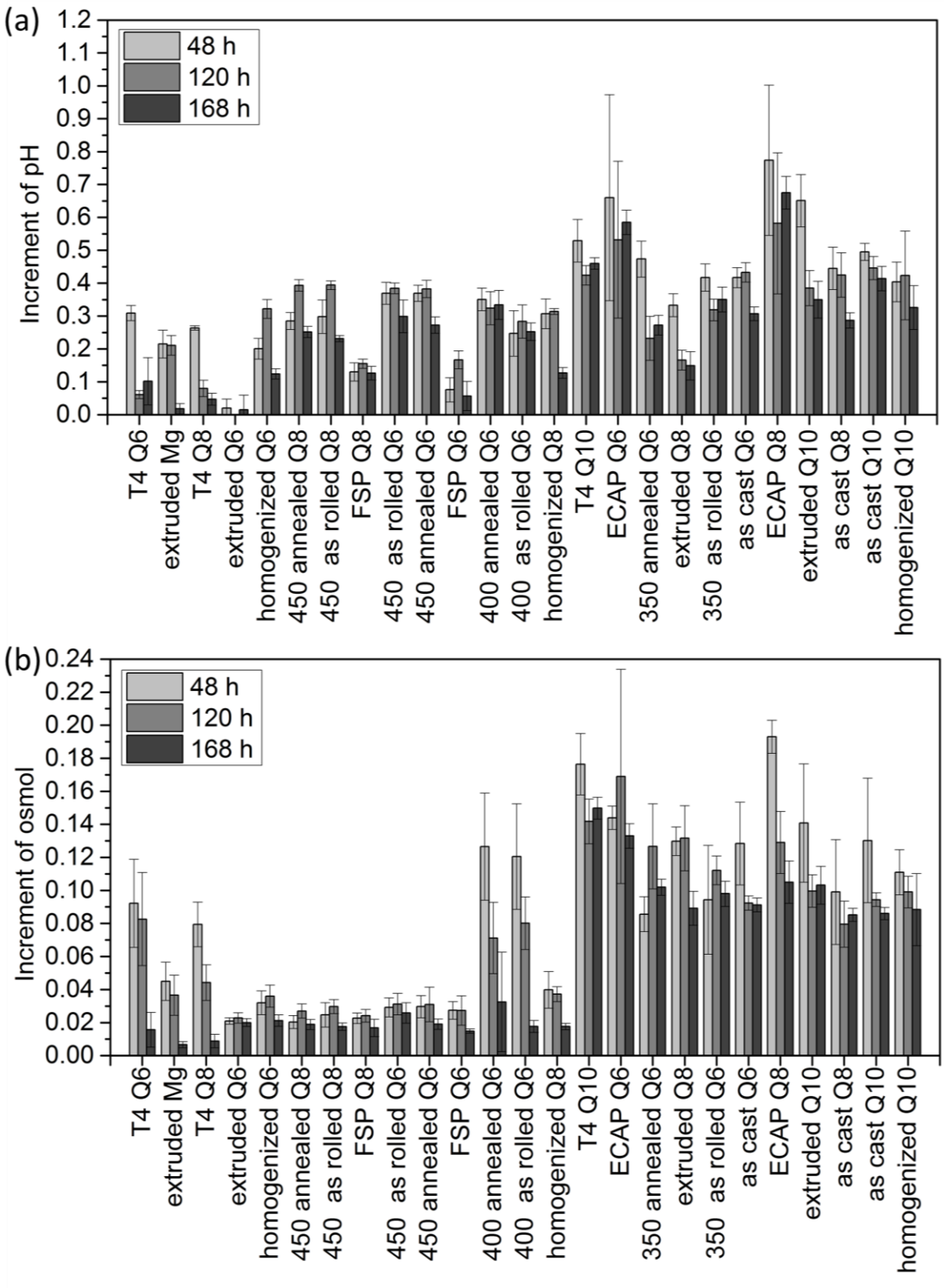

Fig. 4.21: The pH increments with time (a) and the osmolality increments with time (b) in immersion tests.

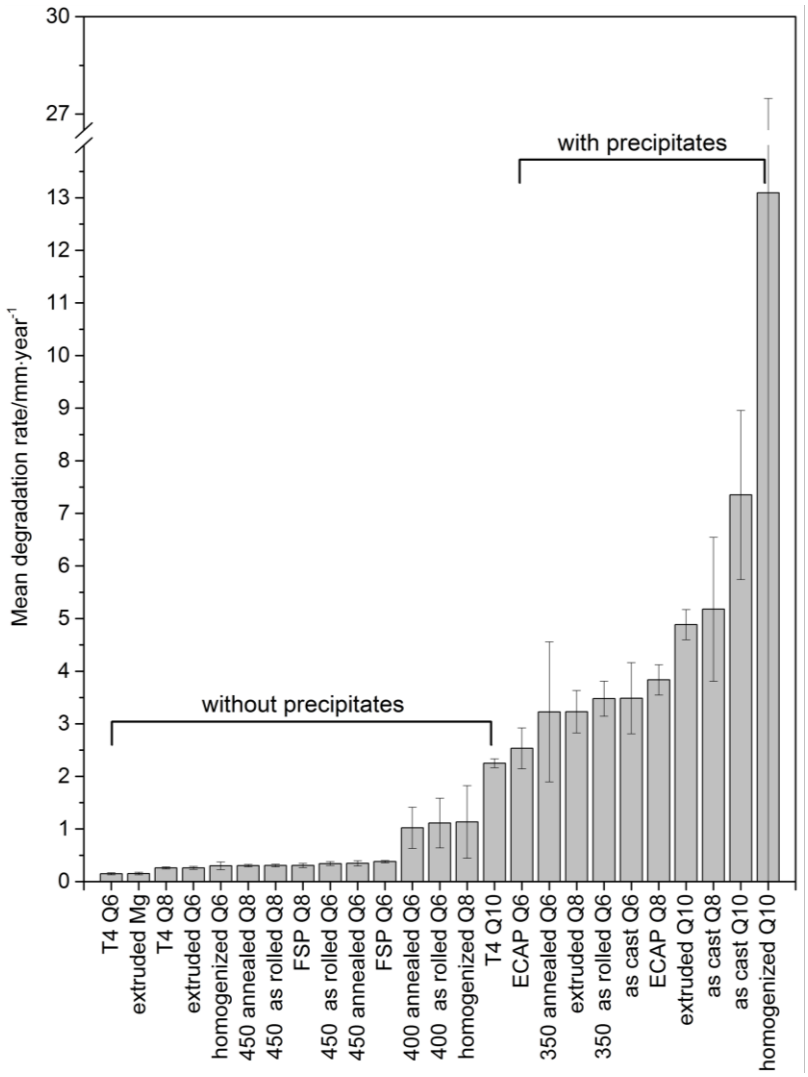

Fig. 4.22: Mean degradation rates of Mg-Ag alloys after immersion tests for 7 days.

4.3.2 Morphology

The existence and distribution of second phases or precipitates influenced the morphology of Mg-Ag alloys in the degradation. Severe local pitting was observed. The degraded surfaces became rough, e.g., the surface of extruded Q10 (Fig. 4.23). In extruded+T4 Q10, the precipitates were eliminated, so the degradation became much homogeneous. Even the raw scratches caused by grinding can be observed from the platforms. No pitting but platforms can be observed, although the degradation rate of the extruded+T4 Q10 is still very high. The FSP Q6 and FSP Q8 obtained lower degradation rate compared to the as cast alloys. The surfaces were flat without big platforms, especially the surface of FSP Q8 (Fig. 4.24).

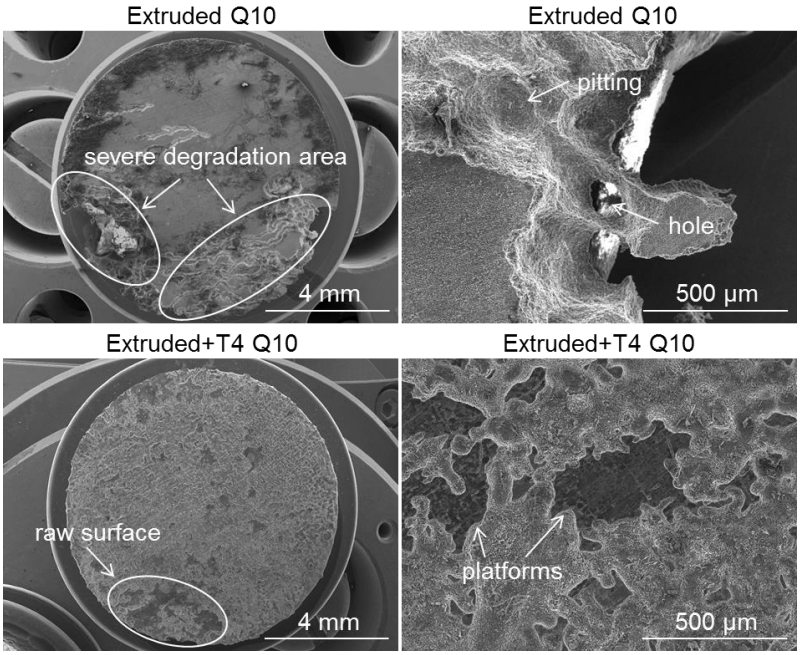

Fig. 4.23: Morphologies of the extruded Q10 and extruded+T4 Q10 after the removal of degradation products.

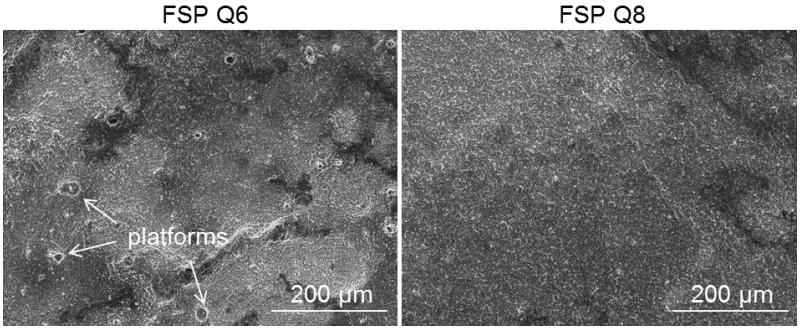

Fig. 4.24: Morphologies of FSP Q6 and FSP Q8 after the removal of degradation products.

After immersion tests and the removal of degradation products, the morphologies of the as rolled and annealed Q6 and Q8 surfaces were analyzed by SEM (Fig. 4.25). The Q6 rolled at low temperature showed severe local pitting, but the pitting was relieved with the increase of temperature. When the rolling and annealing temperature increased to 400°C, there were still pits observable in Q6, but they were restrained to smaller regions and distributed along the rolling direction. The pits should be near or on the precipitates bands. When the rolling and annealing temperature was increased to 450°C, the degradation morphologies of the annealed Q6 and Q8 were homogeneous. However, the as rolled Q6 rolled at 400 and 450°C and the as rolled Q8 rolled at 450°C showed intergranular degradation. Even grain boundaries and twins of

as rolled Q6 can be observed from the surface. The difference of precipitates distribution in the as rolled Q6 and annealed Q6 rolled at 350°C is shown in Fig. 4.26. Many very fine precipitates distribute in the twins and grain boundaries of the as rolled Q6. However, only a few small precipitates exist at the grain boundaries of the annealed Q6.

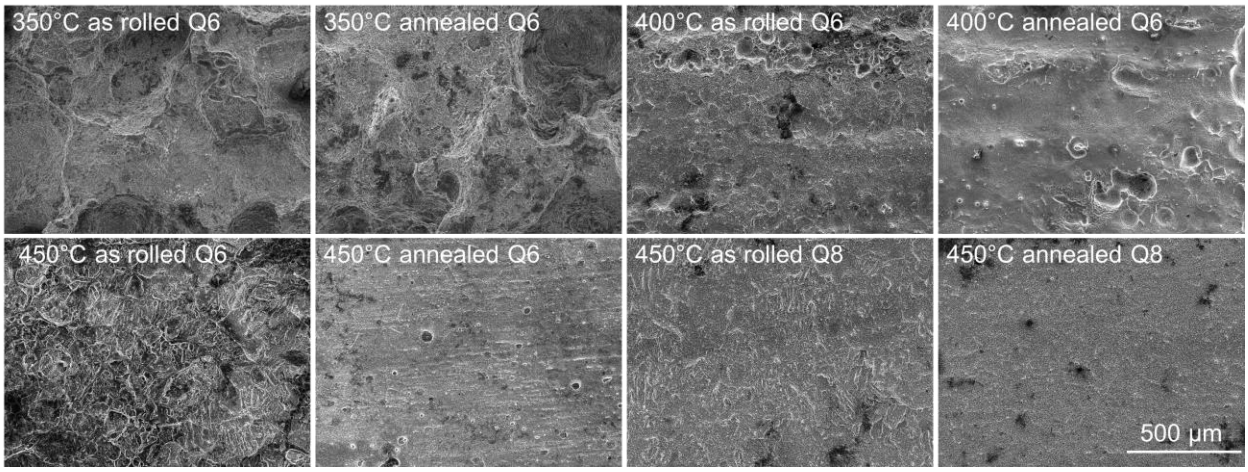

Fig. 4.25: Morphologies of the as rolled and 30 min annealed Q6 and Q8 after the removal of degradation products.

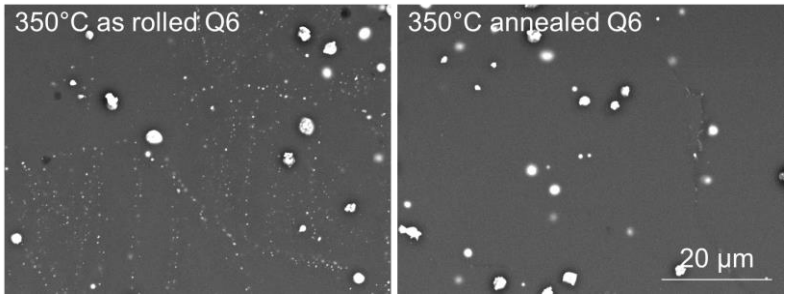

Fig. 4.26: Precipitates distribution in the as rolled and 30 min annealed Q6.

4.4 Cytocompatibility *in vitro*

As biodegradable implant materials, Mg-Ag alloys should meet biological criterions in human body. It is necessary to check the viability of cells on alloys during the degradation as an early evaluation. Concentrations of the released ions in extracts and the pH values are also need to be characterized. In this part, cytotoxicity tests were conducted by MTT assay and Live/Dead staining. It is supposed that high degradation rate is adverse to the viability of cells, so the extruded Q6, extruded Q8, extruded+T4 Q6 and extruded+T4 Q8 which have lower degradation rate were chosen to be evaluated.

4.4.1 MTT assay

The pH values and osmolalities of extracts from the pure Mg, extruded Q6, extruded Q8, extruded+T4 Q6 and extruded+T4 Q8 were elevated compared to the CCM (Table 4.2). More Mg exists in the extracts than in CCM, but the concentrations of Ca in the extracts decreased (Table 4.3). It is supposed that magnesium/calcium phosphates compounds formed in the degradation layer during degradation [7, 12, 19, 29]. The osmolalities of the extruded+T4 Q6 and Q8 extracts were lower than that of the pure Mg and extruded Q6 and Q8. The concentrations of Mg, Ca and Ag in the primary extracts from the extruded Q6 and Q8 were higher than that from the extruded+T4 Q6 and Q8.

In MTT assay, all primary extracts, including pure Mg extract, showed cytotoxicity compared to CCM because of the high pH and osmolality (Fig. 4.27). Cell viabilities in the primary extracts were below the cytotoxic limit of 75% cell viability. Most of the extracts with 20% concentration did not show any cytotoxicity according to this criterion, except for the extract from the extruded Q8, which also did not reach the level of 75%, because the silver concentration was still higher than the tolerable concentration of human primary osteoblasts. The extracts with 10% and 20% concentrations from the extruded+T4 Q8 showed good cytocompatibility as well as the other extracts with low concentrations and CCM.

Table 4.2: The increments of pH values and osmolalities of extracts from pure Mg and Mg-Ag alloys compared to CCM.

Extracts	**pH**	**Osm/kg**
Extruded pure Mg	0.815	0.107
Extruded Q6	0.920	0.110
Extruded+T4 Q6	0.955	0.066
Extruded Q8	0.895	0.104
Extruded+T4 Q8	0.965	0.068

Table 4.3: The concentrations of elements in the extracts from pure Mg and Mg-Ag alloys.

Extracts	**Extract concentration**	**Concentration (mg/L)**		
		Mg	Ca	Ag
Extruded pure Mg	primary	1210	27	<0.1
	20%	258	65.4	<0.1
	10%	139	70.2	<0.1

	primary	1280	26	1.2
Extruded Q6	20%	272	65.2	0.24
	10%	146	70.1	0.12
	primary	1010	17	0.31
Extruded+T4 Q6	20%	218.8	62.6	0.062
	10%	119.9	68.3	0.031
	primary	1150	25	104
Extruded Q8	20%	246	65	20.8
	10%	133	70	10.4
	primary	930	15	0.64
Extruded+T4 Q8	20%	202.8	62.2	0.128
	10%	111.9	68.1	0.064
Cell culture medium (CCM)		20	75	<0.1

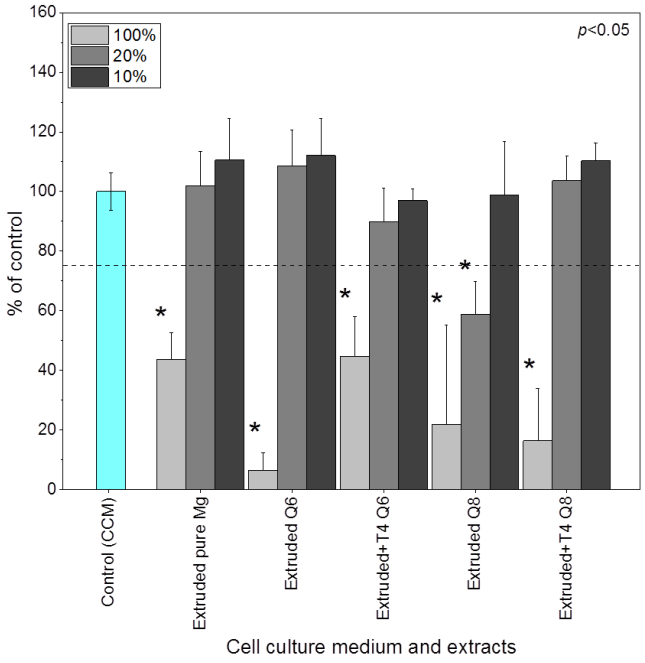

Fig. 4.27: Viabilities of human primary osteoblasts determined by MTT assay in the primary extracts and low concentration (20% and 10%) extracts from the pure Mg, extruded Q6, extruded Q8, extruded+T4 Q6 and extruded+T4 Q8. The dotted line marks 75% cells viability, which indicates no potential cytotoxicity [185]. The "*" indicates statistically significant difference at $p<0.05$ vs. the control group (CCM).

4.4.2 Adhesion tests and Live/Dead staining

The pH values and osmolalities of extracts from the disc preincubation for 24 hours and culture of human primary osteoblasts on the discs for 3, 6 and 9 days were measured. The pH of extracts from the pure Mg and extruded+T4 Q6 and Q8 decreased gradually with time (Fig. 4.28). The osmolality of the extract from pure Mg was stable, and the osmolality of the extract from extruded Q6 increased slightly with time. However, the osmolality of the extract from extruded Q8 remained at a high level after preincubation. This extract possessed nearly the highest pH and osmolality at all time points. The extracts from the extruded+T4 Q6 and Q8 had high osmolality after preincubation for 24 hours, but the osmolalities of these extracts decreased rapidly with time.

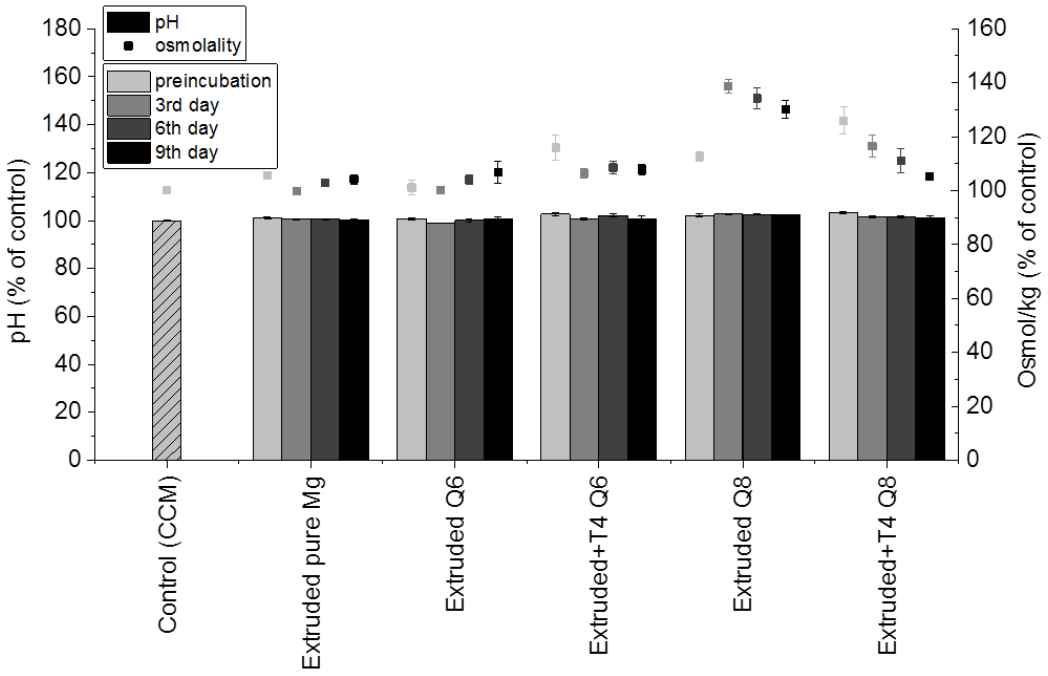

Fig. 4.28: Changes of pH values and osmolalities of extracts compared to CCM during the adhesion tests in 9 days.

In Fig. 4.29, cell layers and the details of human primary osteoblasts can be observed on the surfaces of the extruded Q6, extruded+T4 Q6 and extruded+T4 Q8, except for the extruded Q8 where there were only thick degradation products. The white areas in the images of the extruded Q6, extruded+T4 Q6 and extruded+T4 Q8 were osmium tetroxide which was introduced in the cell fixation procedure. Single human primary osteoblast can be observed on the surface of the extruded+T4 Q6 and Q8.

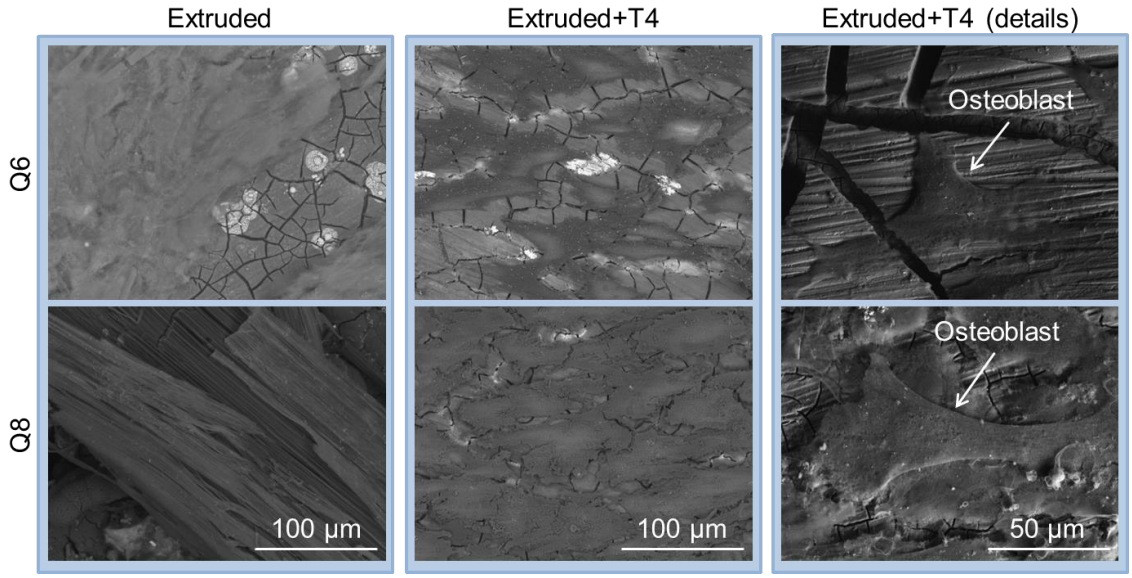

Fig. 4.29: Human primary osteoblasts layer and single osteoblast on the extruded Q6, extruded+T4 Q6 and extruded+T4 Q8. The third column has higher magnification than the second column. The arrows point out single human primary osteoblast.

The regions with the same cell density were selected for comparison after Live/Dead staining (Fig. 4.30). The degradation rates of the extruded pure Mg and extruded Q6 were much lower than that of the extruded Q8 in CCM under cell culture conditions according to the osmolalities (Table 4.2). Human primary osteoblasts survived and attached to the extruded pure Mg and extruded Q6 and extruded+T4 Q6 discs instead of the extruded Q8. After 3 days, on the pure Mg, extruded Q6 and extruded+T4 Q6, some dead human primary osteoblasts were observed. After 6 days, the number of dead human primary osteoblasts decreased slightly. After 9 days, no viability difference of human primary osteoblasts was observed on the pure Mg, extruded Q6 and extruded+T4 Q6 discs.

However, the extracts from the extruded Q8 always had the highest average pH and osmolality, which indicated a faster degradation rate than the others. The pH and osmolality near the surface of the extruded Q8 discs was high. Many bubbles formed on the surface and a large amount of silver was released. As a result, no human primary osteoblasts attached to the surface and survived on the extruded Q8 discs. After T4 treatment, the pH and osmolality of Q8 discs were lower and the Q8 discs showed better cytocompatibility than before. Human primary osteoblasts can attach and proliferate on the extruded+T4 Q8 discs as on pure Mg and extruded Q6 discs, but a slightly higher amount of dead cells was observed on the surface of the extruded+T4 Q8 in the initial stage of 3 days.

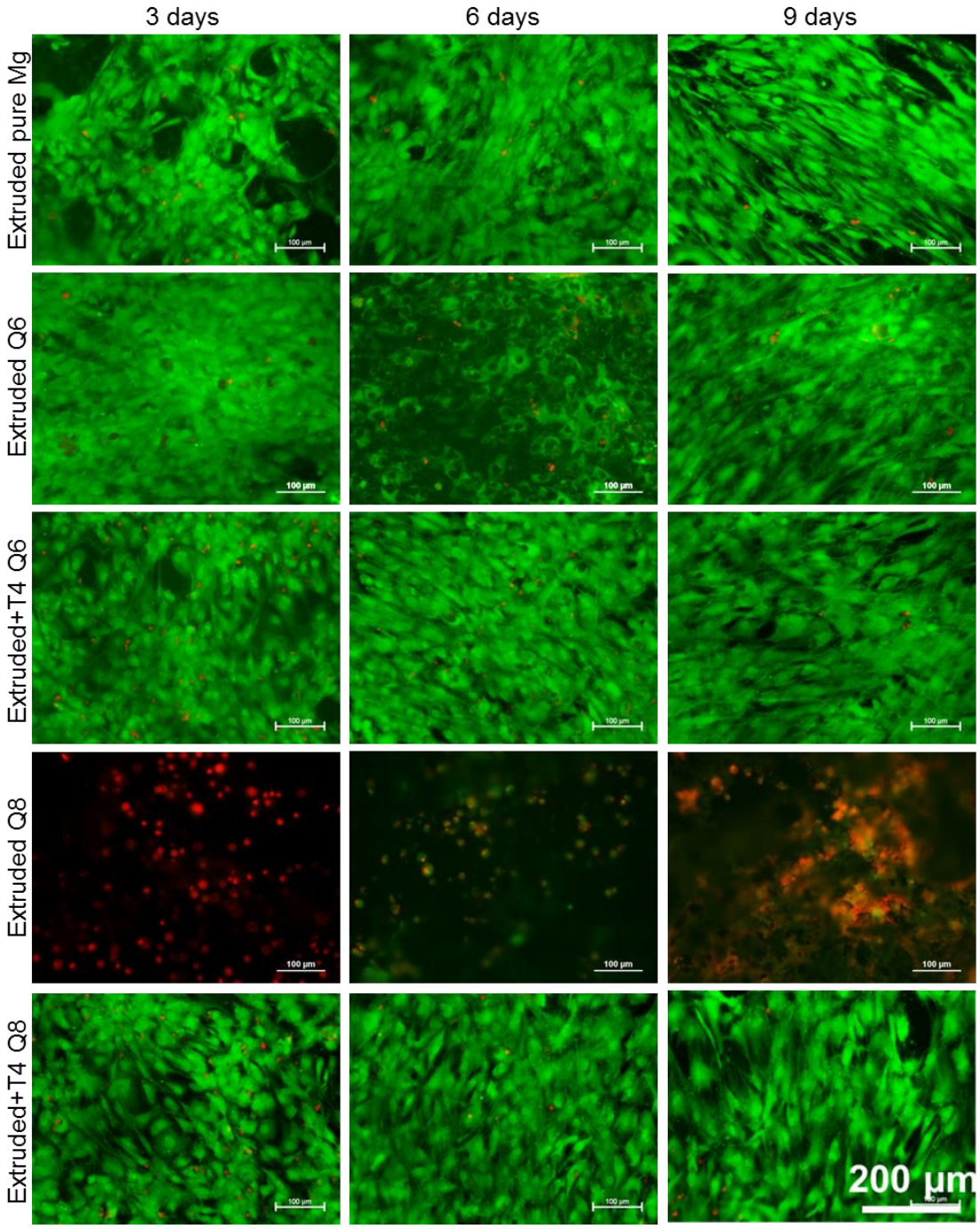

Fig. 4.30: Live/Dead staining of human primary osteoblasts on the extruded pure Mg, extruded Q6, extruded+T4 Q6, extruded Q8 and extruded+T4 Q8 after 3, 6 and 9 days.

4.5 Mineralization behavior with cells

In this part, the biomineralization behavior of cells on Mg-Ag alloys was evaluated since cells are responsible to produce HA to rebuild bone tissues during the service time. It is necessary to

evaluate the activity of HA synthesis by cells as well as inorganic mineralization. The extruded pure Mg and cells without samples were set as control groups. The extruded+T4 Q6 and Q8 which have the lowest degradation rate were chosen for the mineralization evaluation.

The green color means HA crystals in Fig. 4.31. The differentiated HUCPV cells can synthesis HA particles and produced more HA than the human primary osteoblasts. In the areas with higher density of cells, there are more HA particles than the other areas (Fig. 4.31a). The inorganic mineralization (HA) by cell culture medium and biomineralization by cells can be distinguished easily in Fig. 4.31b. Most of the HA on pure Mg was formed by inorganic mineralization. The green particles were produced by cells via biomineralization.

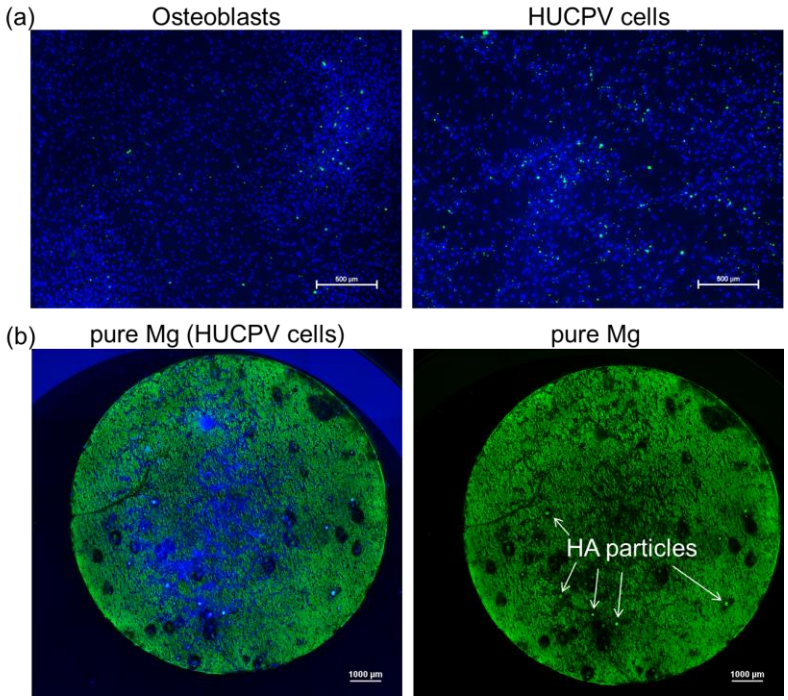

Fig. 4.31: Control groups of mineralization assay with only cells (a) and pure Mg discs (b). The scale bars are 500 µm (a) and 1000 µm (b).

One week later, nearly the entire surface of pure Mg was covered by HA (Fig. 4.32 and 4.33). The HA distributed along the scratches which were caused by grinding. However, the HA formed by inorganic mineralization was much less on the extruded+T4 Q6 and Q8 than on pure Mg. There were only green dots existing on the surface of the extruded+T4 Q6 and extruded+T4 Q8 discs, which were mainly produced by cells. Two weeks later, the HA particles increased. The DAPI staining showed that the HUCPV cells grew and proliferated well on the pure Mg, extruded+T4 Q6 and extruded+T4 Q8 discs.

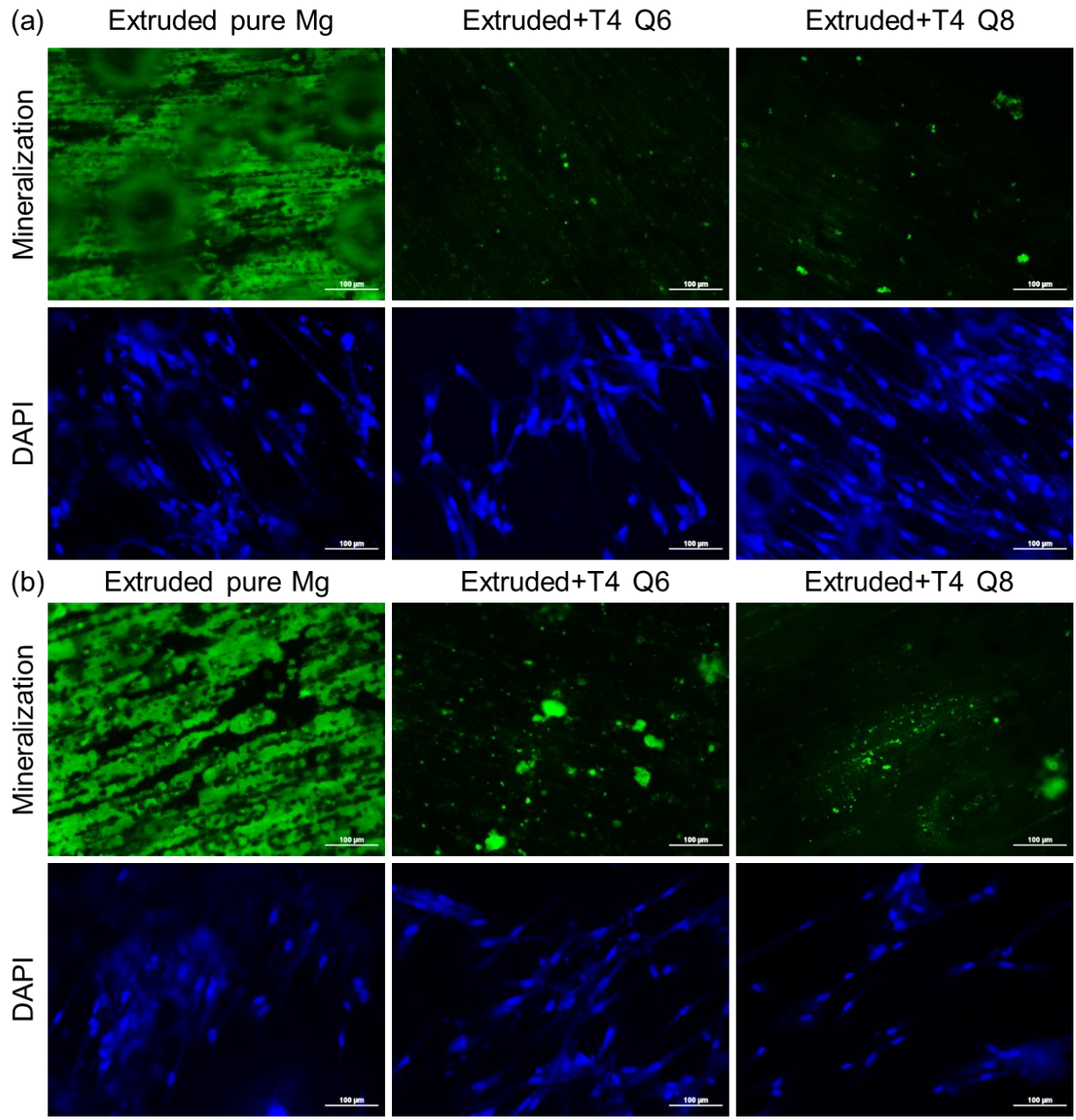

Fig. 4.32: Mineralization assay with HUCPV cells after one week (a) and two weeks (b). The scale bars are 100 µm.

The pure Mg with HUCPV cells was always covered by HA over the whole surface in three weeks (Fig. 4.33). It is interesting that more and more HA particles formed on the surface of the extruded+T4 Q6 and extruded+T4 Q8 discs with time. It was found that the productivity of HA by HUCPV cells was inhibited to some extent with the increase of silver content. The HUCPV cells synthesized more HA particles on the extruded+T4 Q6 disc than on the extruded+T4 Q8 disc. The existence of silver influenced the biomineralization procedure of HUCPV cells as well as the

inorganic mineralization.

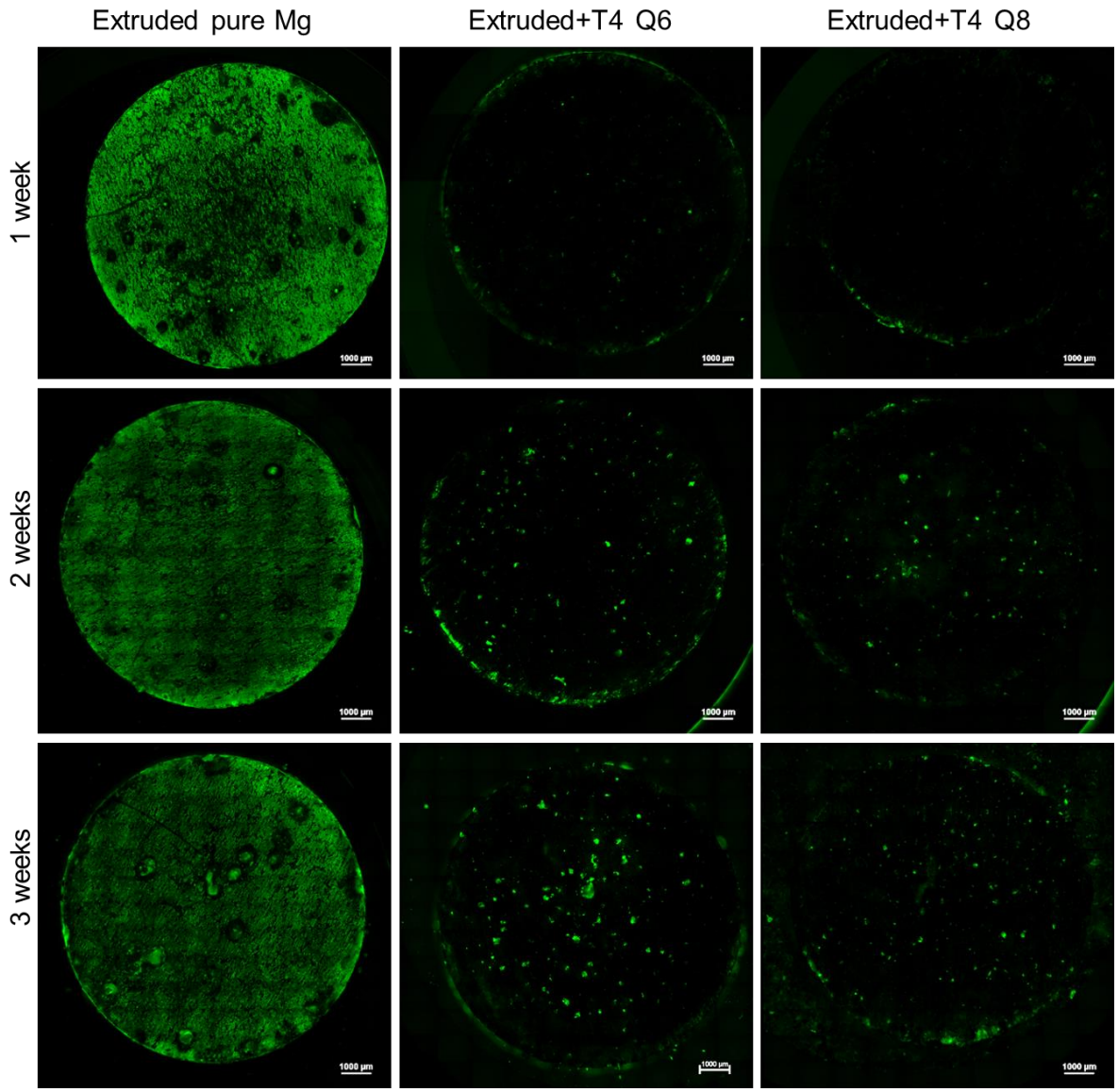

Fig. 4.33: Mineralization overview of discs with HUCPV cells in three weeks. The scale bars are 1000 µm.

Human primary osteoblasts produced less HA than the HUCPV cells on the extruded+T4 Mg-Ag alloys as well as on the pure Mg and the control group without disc (Fig. 4.31, 4.33 and 4.35). The DAPI staining showed these human primary osteoblasts grew and proliferated well on the extruded pure Mg and extruded+T4 Mg-Ag discs (Fig. 4.34). The human primary osteoblasts grew and proliferated better than the HUCPV cells on the extruded pure Mg, extruded+T4 Q6 and extruded+T4 Q8.

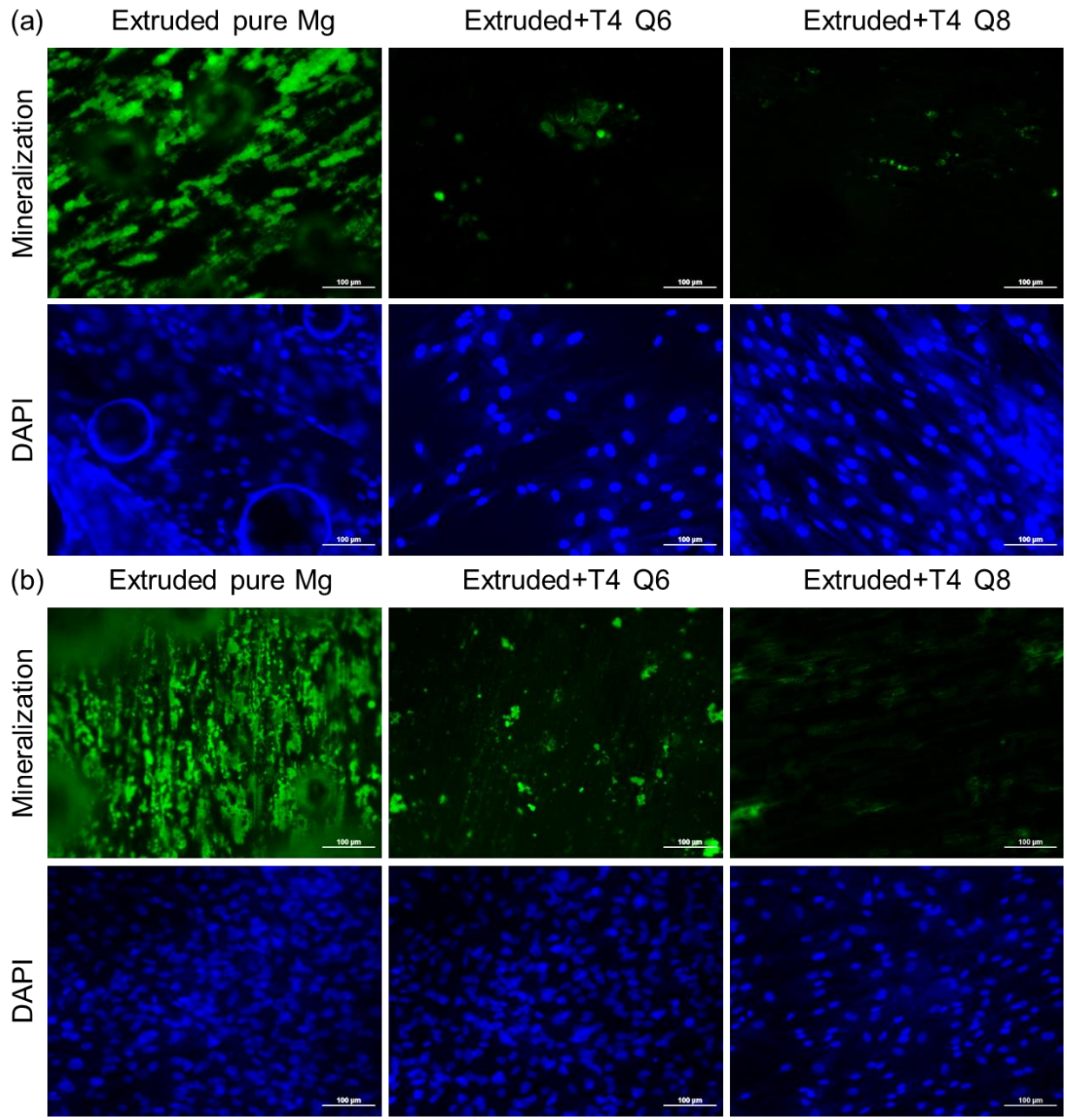

Fig. 4.34: Mineralization assay with human primary osteoblasts after one week (a) and two weeks (b). The scale bars are 100 µm.

The extruded pure Mg discs with human primary osteoblasts were covered by HA everywhere in one week (Fig. 4.35), which was mainly due to inorganic mineralization. There were only few HA particles formed by biomineralization on the extruded+T4 Q6 and Q8. Two or three weeks later, HA on the extruded pure Mg discs became more than before. The HA particles on the extruded+T4 Q6 and Q8 discs also increased slightly, especially on the edge, but the quantity was still rather less than that on the extruded pure Mg. Moreover, the human primary

osteoblasts produced more HA particles on the extruded+T4 Q6 disc than on pure Mg in 3 weeks.

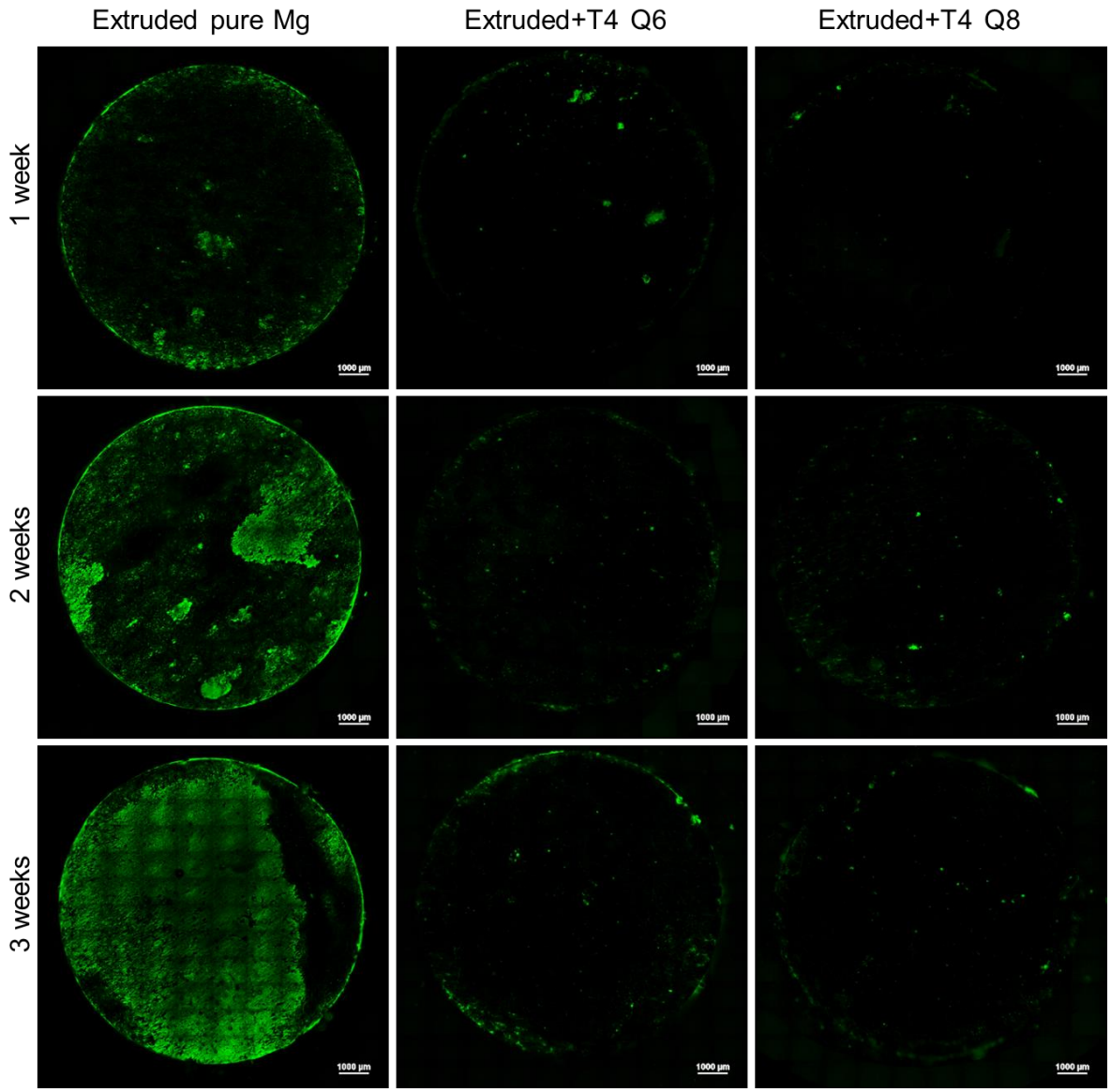

Fig. 4.35: Mineralization overview of discs with human primary osteoblasts in three weeks. The scale bars are 1000 µm.

4.6 Antibacterial properties

Alkaline pH generated by magnesium degradation is helpful to suppress bacteria. However, in dynamic human body, the pH value will be not sufficient. The alloying of silver in magnesium is supposed to deal with this problem well. The antibacterial efficiency of the extruded Q6 and Q8 and extruded+T4 Q6 and Q8 was evaluated in a flow bioreactor system which was used for

bacteria culture and provided the potential of biofilm formation. The pH influence was excluded as much as possible via pH control system automatically. In this case, the antibacterial properties were more related to the silver amount. It is assumed that a higher silver content can bring more effective antibacterial properties.

4.6.1 Bacterial viability

The extruded Q6 and Q8 showed the best antibacterial effect (Fig. 4.36). The viability of bacteria was much lower on the extruded Q6 and Q8 than on the extruded pure Mg. There was a relative high viability of bacteria on pure Mg of 50.35%. However, the bacterial viability on the extruded+T4 Q6 and extruded+T4 Q8 was 18.64% and 14.75%, respectively, which was significantly lower than that on the extruded pure Mg. In addition, more bacteria were observed on the extruded+T4 Q6 and Q8 discs than on the extruded Q6 and Q8 discs. In Fig. 4.37, the bacteria and degradation layer were observed. Some bacteria attached on the degradation layer or inside.

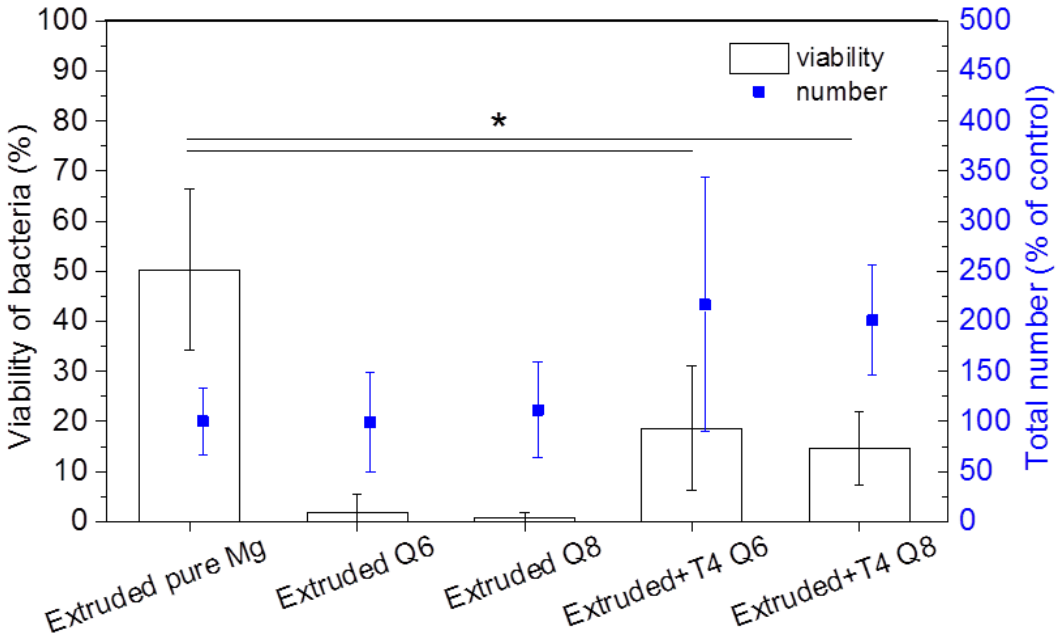

Fig. 4.36: Viability and the total amount of bacteria on the extruded pure Mg, extruded Q6, extruded Q8, extruded+T4 Q6 and extruded+T4 Q8 discs. The "*" here stands for significant difference. A *p*-value<0.05 was considered to be significant.

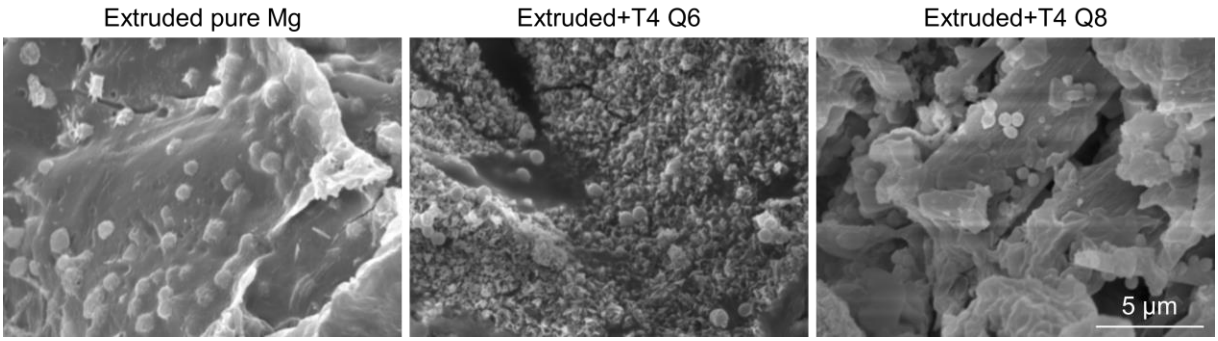

Fig. 4.37: Bacteria on the degradation layer of the extruded pure Mg, extruded+T4 Q6 and extruded+T4 Q8 discs.

4.5.2 Biofilm integrity

In the biofilm tests, incubation for 15 hours permitted the formation of an initial biofilm on Ti discs, which were set as the negative controls for internal evaluation. A nearly complete young biofilm can be observed on the Ti disc (Fig. 4.38a). A large amount of live bacteria on Ti disc can be observed clearly in the high-magnification images (Fig. 4.38b). The total amount of bacteria on the extruded pure Mg was obviously lower than that on Ti disc. The extruded Q6 and Q8 showed local pitting and had a faster degradation rate in BCM with a constant pH (7.2) than in CCM. Many dead bacteria were present on the extruded Q6 and Q8 discs based on the overview images. However, the overview of the biofilm showed no obvious difference between pure Mg and extruded+T4 Q6 and Q8. The high-magnification images showed details of live and dead bacteria. Pure Mg had more live bacteria than the extruded+T4 Q6 and Q8, which was observed from the high-magnification images (Fig. 4.38b). Most of the bacteria on the surface of the extruded+T4 Q6 and Q8 were dead.

4.6.3 Surface morphology in flow condition

The 3-D images of the extruded pure Mg, extruded+T4 Q6 and extruded+T4 Q8 discs before and after the removal of the degradation products are shown in Fig. 4.39. The surfaces of the discs with degradation products appear coarse. It is observed that many degradation products are present on the surface of the pure Mg, extruded+T4 Q6 and extruded+T4 Q8 discs. There are also some needle-like crystals on the extruded+T4 Q6 disc and many on the extruded+T4 Q8 disc, so they look very rough in the 3-D images. However, after the removal of degradation products, the peaks in 3-D images disappeared and many degradation pits were revealed, especially on the extruded pure Mg, where a porous surface was exposed. However, only shallow and broad pits are observed on the surface of extruded+T4 Q6 and Q8 discs, which

indicates more homogeneous degradation morphologies. The average roughnesses (Sa) of the extruded pure Mg, extruded+T4 Q6 and extruded+T4 Q8 are 8.68±0.8, 6.42±0.42 and 8.88±1.92. The developed interfacial areas (Sdr) of them are 37.87±1.44, 19.26±2.72 and 22.39±2.23, respectively. Therefore, the average roughnesses of the extruded pure Mg, extruded+T4 Q6 and extruded+T4 Q8 are at the same level. The developed interfacial areas of the extruded+T4 Q6 and Q8 are significantly lower than that of the extruded pure Mg at $p<0.05$. Therefore, the extruded+T4 Q6 and extruded+T4 Q8 have less contact area with the medium than pure Mg during the degradation.

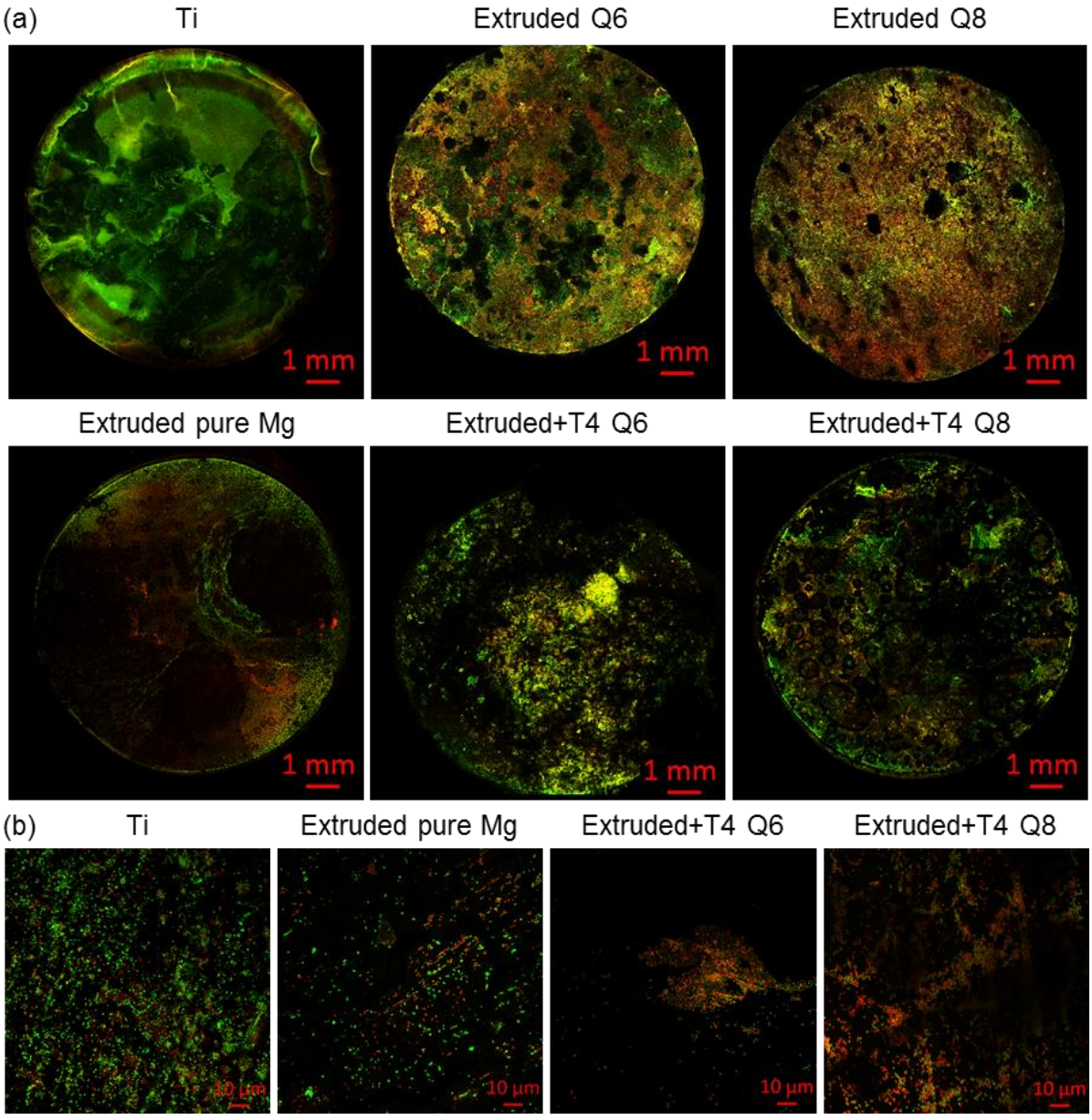

Fig. 4.38: Overview of biofilms (a) and details (b) of live and dead bacteria on discs.

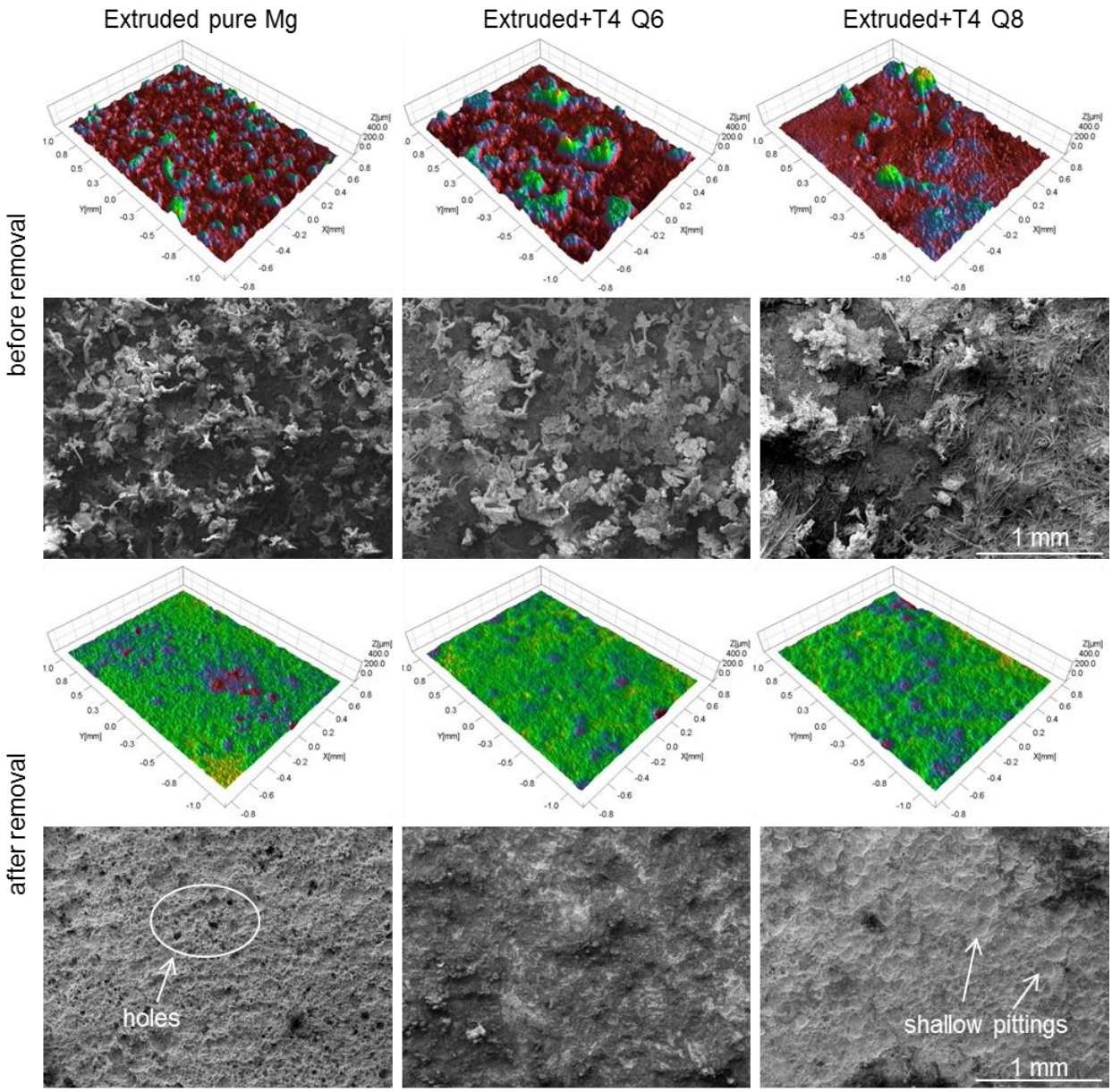

Fig. 4.39: Morphology of the degradation layers of the extruded pure Mg, extruded+T4 Q6 and extruded+T4 Q8 before and after the removal of degradation products in biofilm tests.

4.7 Degradation environment

It is known that the microstructures of Mg-Ag alloys have much influence on degradation behavior. However, the environment also has big influence on the degradation behavior. A series of Q6 and Q8 with precipitates (extruded), without precipitates (extruded+T4) and with more precipitates (extruded+T6) was set to reveal that how the degradation environment influence the degradation behavior (Table 4.4).

The immersion tests were conducted in physiological conditions, aimed to find out the influence of inorganic substances and proteins on the degradation behavior of Mg-Ag alloys. The pH values, osmolalities and degradation rates of the Mg-Ag alloys with different amount of precipitates in a series of solutions were displayed below. The corresponding degradation products and extracts were characterized.

Table 4.4: Grain size and the amount of precipitates in the extruded Q6, extruded Q8, extruded+T4 Q6, extruded+T4 Q8, extruded+T6 Q6 and extruded+T6 Q8.

Mg-Ag alloys	Grain size (μm)	Amount of precipitates (%)
Extruded Q6	29.1±1.2	0.14±0.06
Extruded Q8	8.5±0.3	2.21±0.47
Extruded+T4 Q6	140.9±17.6	0
Extruded+T4 Q8	142.8±1.6	0
Extruded+T6 Q6	29.5±0.9	0.22±0.02
Extruded+T6 Q8	8.6±0.2	2.60±1.01

4.7.1 Degradation behavior in different solutions

To reveal the influences of chemical compositions on the degradation behavior of Mg-Ag alloys, nine kinds of solutions were prepared as shown in the Table 4.5. The pH values and osmolalities of solutions in cell culture conditions were measured, to evaluate the influences of inorganic substances to degradation well.

Table 4.5: The compositions in the solutions for immersion tests.

Solutions	Composition
1	HBSS + 10% FBS + 39.9 mM $NaHCO_3$
2	HBSS + 10% FBS + 1.8 mM $CaCl_2 \cdot 2H_2O$
3	HBSS + 10% FBS + 39.9 mM $NaHCO_3$ + 1.8 mM $CaCl_2 \cdot 2H_2O$
4	HBSS + 10% FBS + 0.8 mM $MgSO_4 \cdot 7H_2O$
5	HBSS + 10% FBS + 39.9 mM $NaHCO_3$ + 0.8 mM $MgSO_4 \cdot 7H_2O$
6	HBSS + 10% FBS + 1.8 mM $CaCl_2 \cdot 2H_2O$ + 0.8 mM $MgSO_4 \cdot 7H_2O$
7	HBSS + 10% FBS + 39.9 mM $NaHCO_3$ + 1.8 mM $CaCl_2 \cdot 2H_2O$ + 0.8 mM $MgSO_4 \cdot 7H_2O$
8	HBSS + 10% FBS
9	HBSS

The pH values and osmolalities of these solutions in cell culture conditions are shown (Fig. 4.40). The solutions containing $NaHCO_3$ have higher pH values and osmolalities than the others, but similar pH values with body fluid. The HBSS (solution 9) has the lowest pH value.

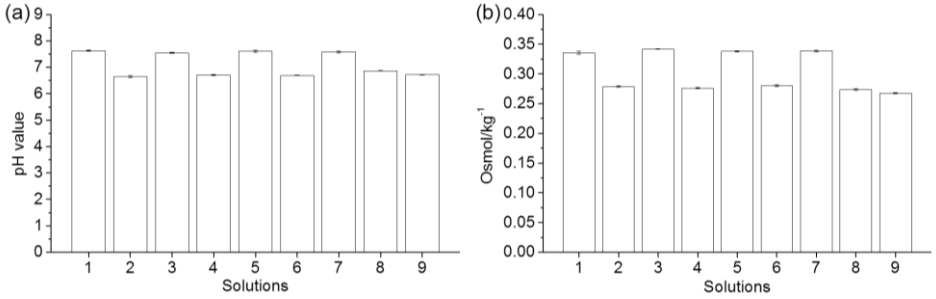

Fig. 4.40: The pH values (a) and osmolalities (b) of solutions in cell culture conditions.

In the immersion tests, the pH values and osmolalities of extracts increased by a different range (Fig. 4.41). The extracts containing $NaHCO_3$ had lower pH increment, which means that the corresponding solutions balanced the pH well. However, the pH of extracts from the solutions without $NaHCO_3$ increased drastically. The pH increments of extracts kept stable in most cases since it already reached a balanced status in immersion tests.

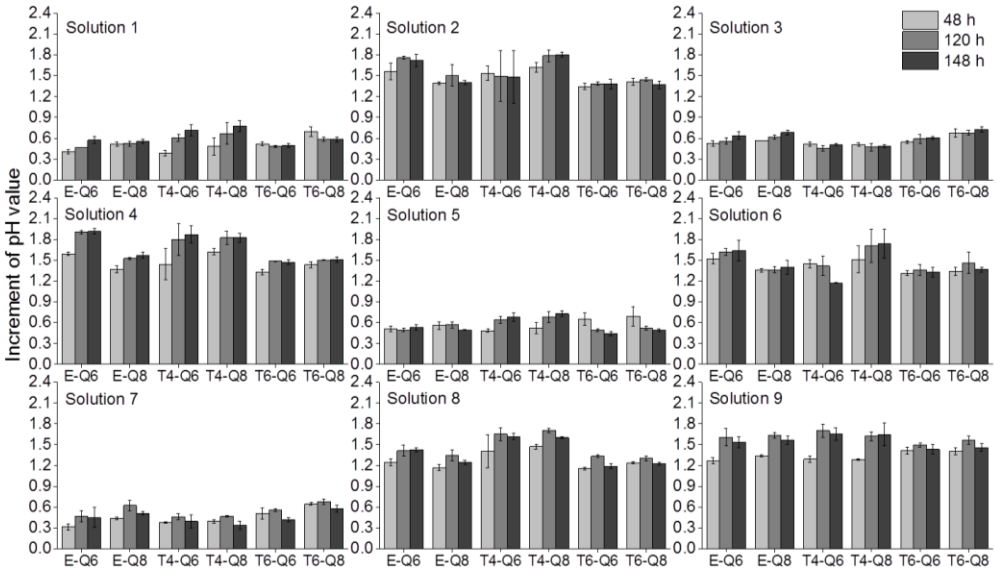

Fig. 4.41: The pH increments of extracts from different solutions with time. The Q6-E, Q8-E, Q6-T4, Q8-T4, Q6-T6 Q8-T6 stand for the extruded Q6, extruded Q8, extruded+T4 Q6, extruded+T4 Q8, extruded+T6 Q6 and extruded+T6 Q8, respectively.

The initial osmolality increments of the extracts were always higher after 48 hours than after 120 and 168 hours (Fig. 4.42). The osmolality increments of the extruded Q6, extruded+T4 Q6 and

extruded+T4 Q8 dropped gradually with time. The osmolality increments of the extruded Q8 dropped down with time, but it is still much higher than that of the extruded Q6, extruded+T4 Q6 and extruded+T4 Q8. The osmolality increments of the extracts from the extruded+T6 Q6 and extruded+T6 Q8 discs were stable and kept a high value, even though the osmolality increments of some extracts dropped slightly at the initial stage. The FBS influence was observed when we compared the osmolality increments of the extruded+T4 Q8 extracts from the solution 8 and solution 9. The extract of extruded+T4 Q8 had higher osmolality increment in solution 9 than in solution 8.

The osmolality reflects the concentration of Mg^{2+} ions in extracts, which is related to the degradation rate of Mg-Ag alloys. On the basis of HBSS with 10% FBS, the addition of $NaHCO_3$ (solution 1) or $MgSO_4 \cdot 7H_2O$ (solution 4) did not decrease the osmolality increments obviously as well as the co-addition of $NaHCO_3$ and $MgSO_4 \cdot 7H_2O$ (solution 5). The addition of $CaCl_2 \cdot 2H_2O$ (solution 2) and co-addition of $CaCl_2 \cdot 2H_2O$ and $MgSO_4 \cdot 7H_2O$ (solution 6) decreased the osmolality increments of the extruded+T4 Q6 and Q8 to some extent. The co-addition of $NaHCO_3$ and $CaCl_2 \cdot 2H_2O$ (solution 3) decreased the osmolality increments of the extruded Q6, extruded+T4 Q6 and extruded+T4 Q8, obviously. The co-addition of $NaHCO_3$, $CaCl_2 \cdot 2H_2O$ and $MgSO_4 \cdot 7H_2O$ (solution 7) decreased those osmolality increments further, which means that the existence of these chemicals can suppress degradation more effectively.

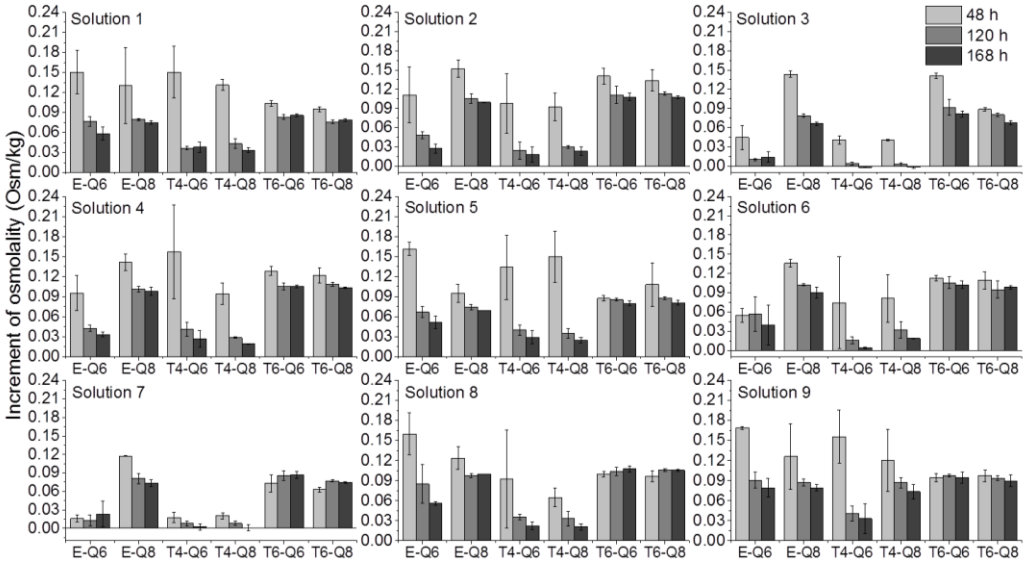

Fig. 4.42: Osmolality increments of extracts from different solutions with time. The Q6-E, Q8-E, Q6-T4, Q8-T4, Q6-T6 Q8-T6 stand for the extruded Q6, extruded Q8, extruded+T4 Q6, extruded+T4 Q8, extruded+T6 Q6 and extruded+T6 Q8, respectively.

The surface morphologies after immersion tests are shown in Fig. 4.43. The extruded Q6, extruded+T4 Q6 and extruded+T4 Q8 discs were clean and have the best integrity in solution 7, but they had more degradation products in solution 8. The extruded Q8, extruded+T6 Q6 and extruded+T6 Q8 showed severe degradation and degraded locally in solution 7, 8 and 9. The surfaces of these discs were covered by a thick white degradation layer.

The extruded Q8 had severe pitting in solution 7, and higher degradation rate in solution 8 (HBSS + 10% FBS) and solution 9 (HBSS). The extruded+T6 Q6 and extruded+T6 Q8 discs were covered by a very thick degradation layer in solution 7, 8 and 9. In solution 9, all discs degraded so fast that the thick degradation products covered the whole surfaces of discs except for the extruded+T4 Q6 disc. Overall, there were more degradation products on the corresponding discs in solution 8 and 9 than in solution 7. After the removal of degradation products, the extruded+T4 Q6 in solution 9 was integral but its surface was a bit rougher than the surfaces of the extruded+T4 Q6 and even the extruded+T4 Q8 discs in solution 7 (Fig. 4.44). Nearly no pits existed on the surface of the extruded+T4 Q6 and extruded+T4 Q8 in solution 7. However, there were shallow pits on extruded+T4 Q6 in solution 9. The extruded+T4 Q8 disc had a partial degradation in solution 9, which was consistent with the substantial rising of osmolality in solution 9.

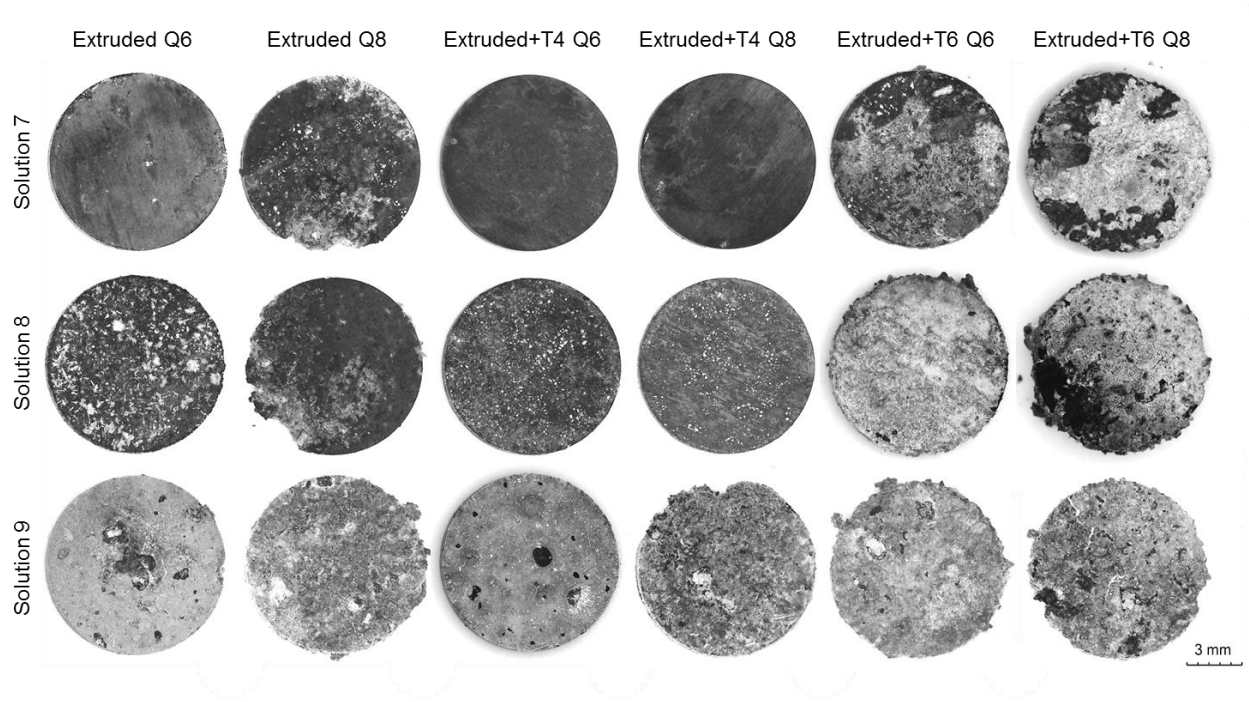

Fig. 4.43: Overview of the extruded Q6, extruded Q8, extruded+T4 Q6, extruded+T4 Q8, extruded+T4 Q6 and extruded+T6 Q8 discs after immersion tests for 7 days.

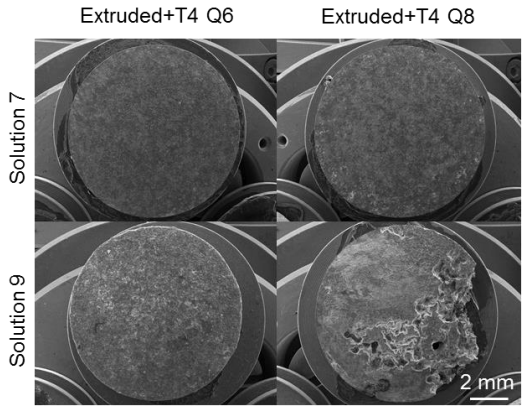

Fig. 4.44: Morphologies of the extruded+T4 Q6 and extruded+T4 Q8 after the removal of degradation products.

The solutions, precipitates and silver content influenced the degradation rates as depicted in Fig. 4.45. The extruded+T6 Q8 had the highest mean degradation rate and showed no significant difference in solution 7, 8 and 9. The extruded Q8 and extruded+T6 Q6 also possessed very high mean degradation rate, especially in solution 9 (HBSS). The degradation rates of the extruded Q8 or extruded+T6 Q6 in solution 7 and solution 8 had no significant difference. The extruded Q6, extruded+T4 Q6 and extruded+T4 Q8 had very low degradation in solution 7 (Fig. 4.45), which was only 0.23 mm/year at most. However, the degradation rate increased gradually from solution 7 to solution 9. The extruded Q6 and extruded+T4 Q8 disc had more obvious increase of degradation rate, which was up to 4.95 mm/year. But the degradation rate of extruded+T4 Q6 still kept below 1.46 mm/year.

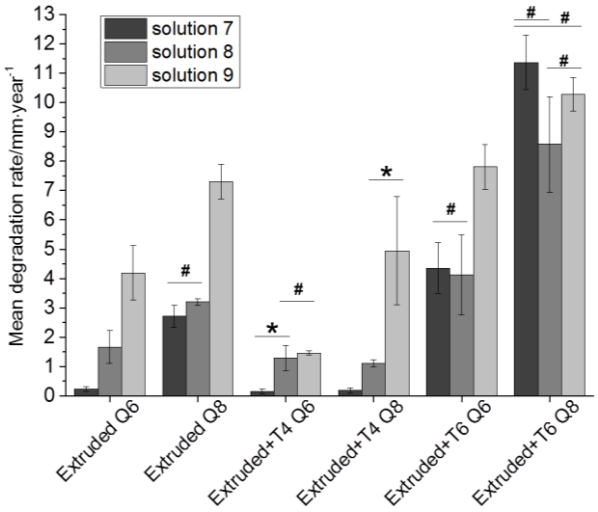

Fig. 4.45: Mean degradation rates of Mg-Ag alloys in solution 7, 8 and 9. The "*" means significant difference and the "#" means no significant difference, when $p<0.05$.

4.7.2 Degradation products and extracts

The main composition of degradation products on the extruded Q8 discs is displayed in Fig. 4.46. According to the small angle XRD patterns (Fig. 4.47a), most of the degradation products are $Mg(CO_3)(H_2O)_3$ crystals. However, according to the broad peaks of the XRD patterns, there is not only crystals but also amorphous $Mg(CO_3)(H_2O)_3$ existing in the degradation layer in the presence of FBS. Some $Mg(CO_3)(H_2O)_3$ products distribute on the extruded Q8 discs in solution 8 (HBSS + 10% FBS) and nearly no silver particles were observed (Fig. 4.46a). However, there are many silver particles in the $Mg(CO_3)(H_2O)_3$ products in solution 9 (HBSS) which has no FBS (Fig. 4.46b). After degradation, some porous silver particles were observed. This may came from the degradation of second phases (Fig. 4.46c).

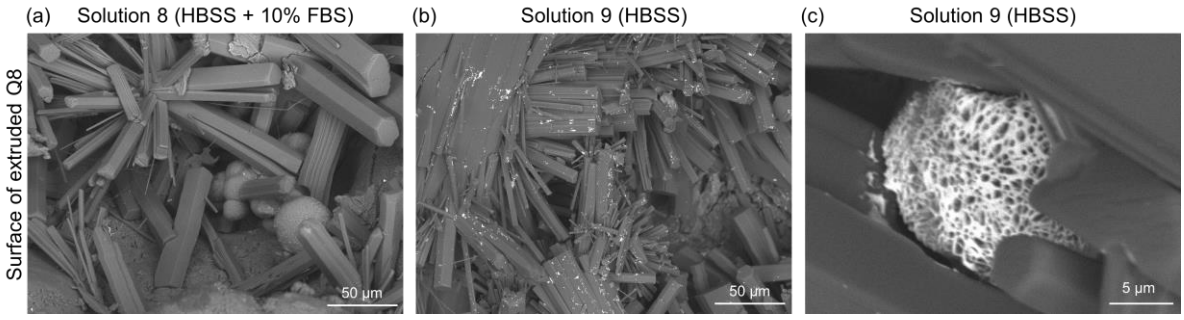

Fig. 4.46: Degradation products on the surface of extruded Q8 in solution 8 (a) and 9 (b and c).

The overviews of surface condition of the extruded+T4 Q6 are different (Fig. 4.47). The density of cracks indicated the compactness of degradation products. The EDS revealed the difference of them in chemical compositions. Magnesium/calcium phosphate compounds formed in the degradation layer of extruded+T4 Q6 in solution 7. The existence of phosphate salts made the degradation layer compact. The grinding scratches on the extruded+T4 Q6 disc in solution 7 are still observed (Fig. 4.47b). The degradation layer of extruded+T4 Q6 in solution 8 has wider cracks. No phosphate and calcium elements exist on the surface. In solution 9, the degradation layer of extruded+T4 Q6 looks even rough and loose. It seems that many crystals and silver particles exist on the layer. Hence, the phosphate compounds and FBS exhibited big influence on the degradation.

In Fig. 4.48, the degradation layer of extruded+T4 Q6 was analyzed. There were two degradation layers on the surface. The outer degradation layer was loose. Many needle-like degradation products formed this layer. The inner one looks dense with small cracks. According to the mapping pictures in Fig. 4.48, silver exists in the inner layer instead of the outer layer.

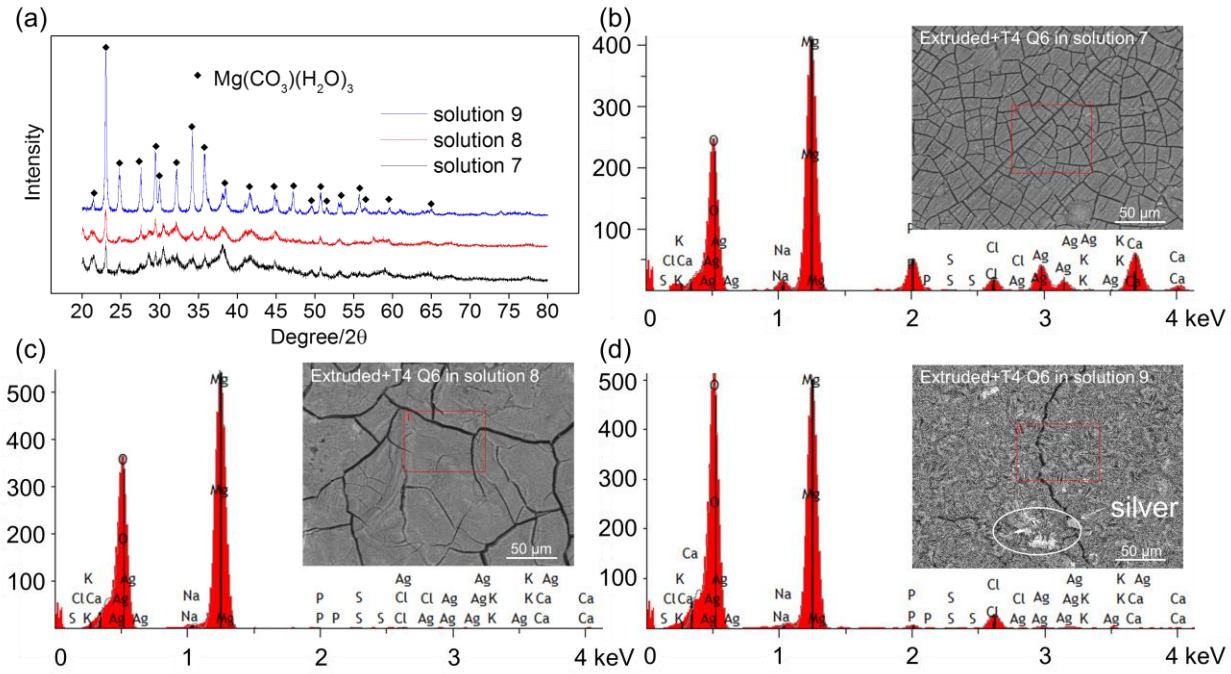

Fig. 4.47: XRD patterns of degradation products in solution 7, 8 and 9 (a), and EDS analysis of the extruded+T4 Q6 discs after immersion tests in solution 7 (b), 8 (c) and 9 (d).

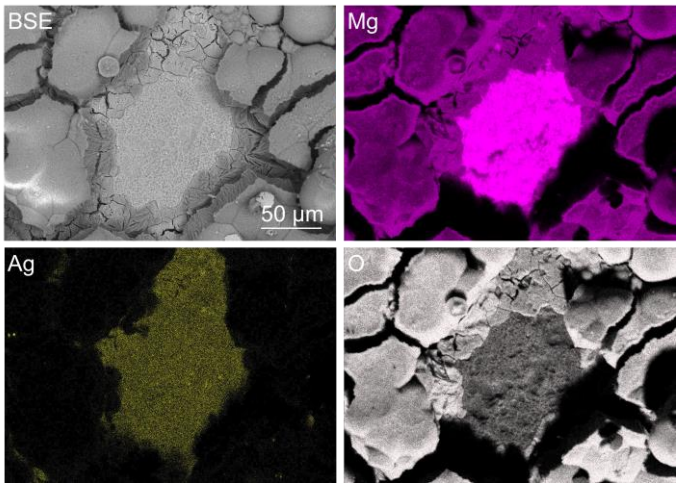

Fig. 4.48: Elemental distribution in the degradation layer of the extruded+T4 Q6.

As antibacterial implant materials, Mg-Ag alloys show antibacterial properties by releasing silver particles and ions. The status of silver has big influence on the antibacterial properties, so it is necessary to make clear its status. In Fig. 4.49a and b, when the degradation rate of Mg-Ag alloys was low or no proteins exist in the solution, no color change was observed. However, the extracts from the solutions with FBS showed the color change when the degradation rate was fast. The reason is that the released silver particles were nano-size and absorbed to the

proteins. Generally, the color of silver staining to proteins is yellow or brown. As a result, proteins-silver formed during the degradation of Mg-Ag alloys. To identify the existence of silver nano-particles in extracts, the diluted HNO_3 (10%, 0.5 mL) was added into brown extract (1 mL) and kept for 2 hours until the extract became transparent. The brown extracts were identified by the following reactions which were normally used for the decolorization of silver staining without influence on proteins [186].

$$3Ag + 4HNO_3 = 3AgNO_3 + NO \uparrow + 2H_2O \qquad \text{Eq. 4.1}$$

$$Ag^+ + Cl^- = AgCl \downarrow \qquad \text{Eq. 4.2}$$

After reaction, the color of deposition is light yellow as little Ag_2CO_3 or Ag_3PO_4 exist in the deposition. However, most of the deposition is AgCl.

As shown in DLS measurements in Fig. 4.50, there are many nano-size proteins in solution 8 (HBSS + 10% FBS). Only a few particles exist in solution 9 (HBSS) due to the existence of crystals or impurities inside. There is no change of protein size in extracts from pure Mg and extruded+T4 Q6 which have low degradation rate in solution 8. In the extruded Q8 extract, the proteins agglomerated. It means that the pH, osmolality or silver nano-particles influenced the proteins when the degradation rate was fast.

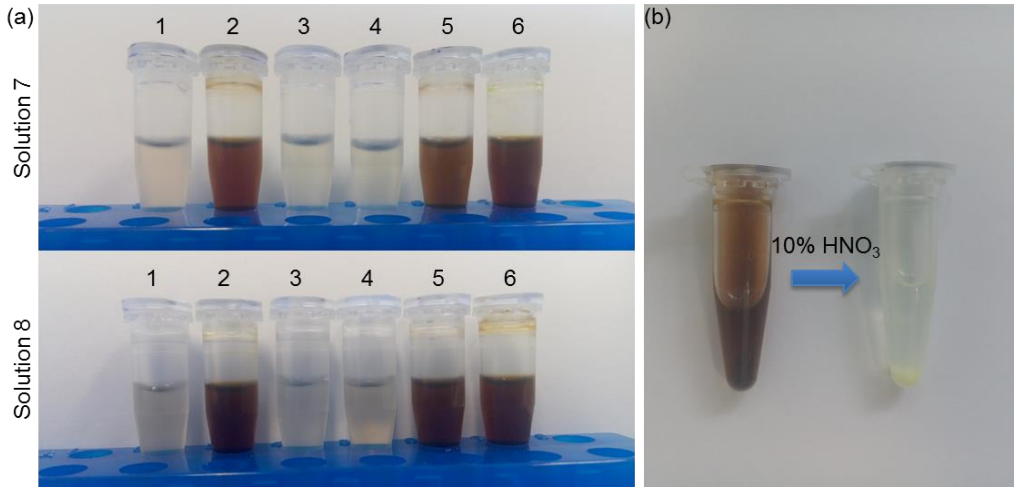

Fig. 4.49: Extracts from Mg-Ag alloys (a), identify of silver metal by addition of 0.5 mL 10% HNO_3 solution in 1 mL brown extract (b). The numbers in (a) from 1 to 6 stand for extracts from the extruded Q6, extruded Q8, extruded+T4 Q6, extruded+T4 Q8, extruded+T6 Q6 and extruded+T6 Q8.

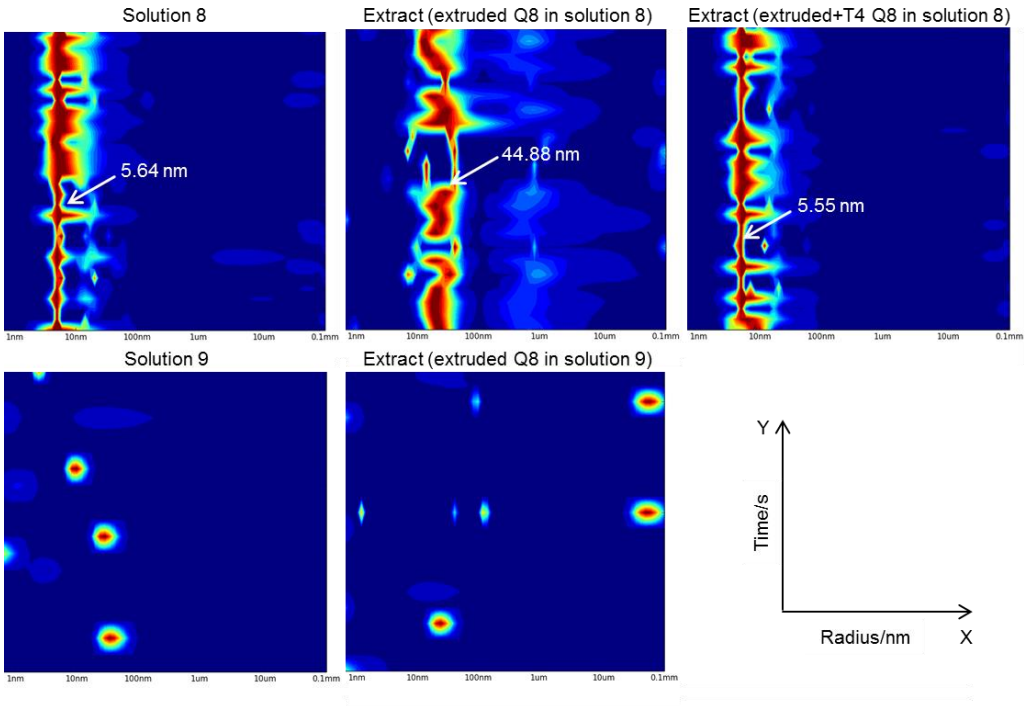

Fig. 4.50: Analysis of protein sizes by DLS. The X-axis is radius (nm) of proteins and the Y-axis is time (s).

5. Discussion

5.1 Thermomechanical processing and microstructure

For the as cast microstructure, with the increase of silver in magnesium, the amount of second phases increased and the dendrites became more obvious. Low silver solubility and constitutional supercooling were responsible for this phenomenon according to the simulated Mg-Ag phase diagram (Fig. 3.9). Moreover, the needed temperature of homogenization and solution treatment changed with silver content in Mg-Ag alloys.

In thermomechanical processing, several dynamic recrystallization (DRX) nucleation mechanisms have been proposed during the last decades [125, 128, 129, 187-189]. Magnesium alloys have low medium stacking fault energy (SFE) [125, 129]. During hot deformation, nucleation by bulging [125, 128, 188, 190], subgrain rotation [129, 191] and twinning [125, 191] are the main mechanisms. There is a correlation of the DRX mechanisms with deformation conditions, so the DRX mechanism is affected by the operating deformation processes [133]. In this study, these thermomechanical processing of hot extrusion, ECAP, FSP and the rolling with subsequent annealing brought more homogeneous microstructure compared to the as cast Mg-Ag alloys, which referred to different recrystallization kinetics. In the thermomechanical processing of hot extrusion, ECAP and FSP, the new microstructure resulted from the occurrence of recrystallization nuclei followed by nucleus growth and the long-range migration of the grain boundaries until complete impingement [124, 129]. These processes occurred in two steps and generally referred to discontinuous dynamic recrystallization (dDRX) [130, 131, 192]. For the rolling and annealing of Mg-Ag alloys, the workability substantially increased as additional slip systems became sufficiently available by thermal activation at elevated temperatures [193]. This conveyed excellent formability to Mg-Ag alloys and enabled sheet production by rolling processing. Twinning and basal slip were the main deformation mechanism judging from the as rolled microstructure. Since nucleation is slow in recrystallization of magnesium [194] and the rolling speed was fast, there was nearly no dynamic recrystallization during the rolling processing. Instead, many twins occurred in the Mg-Ag alloys. However, static recrystallization (SRX) happened during the annealing of as rolled Mg-Ag alloys [195].

5.2 Microstructure influences on mechanical properties and degradation

The as cast Mg-Ag alloys have inhomogeneous microstructure and the increase of silver can strengthen this tendency. Homogenization treatment after casting cannot relieve it well. Irregular grain shape and large grain size are adverse to the mechanical strength and elongation. For manufacturing processes to date, most of the developed magnesium products have been fabricated by casing, in particular, die casting and thixo-casting, whereas a plenty of defects exist in the as cast magnesium alloys, which affects the mechanical integrity during the degradation process [196]. In other words, quality control and further thermomechanical processing are necessary steps for Mg-Ag alloys, especially, when the silver content is high. Moreover, other studies mentioned that the microstructural difference between the fine-grained die-cast and coarse-grained sand-cast magnesium alloys has no significant effect on the *in vitro* degradation behavior. However, the degradation analysis of these alloys suggests that the high volume fraction of second phases in the as cast magnesium alloys may not be suitable for biodegradable implant applications, due to the high stability of the second phases in physiological conditions [197]. Hence, the as cast Mg-Ag alloys are not suitable for biodegradable implant applications.

5.2.1 Microstructure and mechanical properties

The mechanisms of mechanical strengthen include precipitates dispersion strengthening, grain refining strengthening, solid-solution strengthening, working hardening and so on [198-200]. Because of low solubility of silver in magnesium at low temperature, many second phases exist in the as cast Mg-Ag alloys, which contributes to the increase of hardness. However, these as cast alloys still have coarse and irregular grains, which leads to low and unstable mechanical strength. By hot extrusion, the grains were refined but many precipitates separated out from the Mg-Ag alloys when the silver content was high. These precipitates restricted grain growth during the hot extrusion, so the extruded alloys had smaller grains than the as cast alloys. This resulted in strengthening of tensile properties. The ECAP fabricated ultrafine grains and considerable amount of precipitates due to strong shearing force at lower temperature than the solvus temperature of silver in alloys. The ultrafine grains and precipitates strengthened the hardness, pronouncedly. In the rolling, with elevating of the rolling temperature, the amount of precipitates in Mg-Ag alloys was lower and the grain enlarged. As a result, the hardness of Mg-Ag alloys dropped with the elevated temperature.

In general, solid-solution strengthening is one of the major mechanisms to increase the strength of metallic materials. The effect of solid-solution strengthening in magnesium alloys has been investigated using many kinds of solute atoms [201, 202]. For Mg-Ag alloys, the element Ag is effective in suppressing grain boundary sliding (GBS) in solid-solution status. The suppression of GBS is associated with low grain boundary energy, of which the reduction depends on the alloying element Ag by changing the lattice parameter (c/a ratio) [203]. This means that the solution of Ag in magnesium can strengthen Mg-Ag alloys well for a given grain size. Moreover, the solution of Ag in magnesium will influence its plasticity. Hence, solid-solution strengthening is one of the methods to increase the hardness and mechanical properties of Mg-Ag alloys. On the other side, the silver element decreases the stacking-fault energy of magnesium according to the first-principle calculation. Silver improves the strength and ductility of magnesium by reducing the corresponding stacking-fault energy when the silver content is in specific range [204]. Another study also indicated that the solvus of silver in magnesium can improve both the strength and elongation of magnesium alloys [49].

Homogenization resulted in a bit lower tensile properties than that of the as cast alloys, since grain size and second phases influenced strength more than the solid solution. However, the strength of Mg-Ag alloys increased with the increase of silver content due to solid-solution strengthening. In FSP, the microstructures of the basal Mg-Ag alloys were replaced by fine grains without intermetallic precipitates in the stirred zone. The material in this area possesses fine equiaxed grains, which is a result of discontinuous dynamic recrystallization [130, 131, 192]. Normally, the hardness of the stirred zone is much higher than that of the base material [205]. The Mg-Ag alloys with fine grains and high solvus of silver possesses higher hardness and tensile strength. At the rolling temperature 450°C, no precipitation in alloys could be observed since this temperature was higher than the solvus temperature of silver. After rolling and annealing at 450°C, Mg-Ag alloys with higher silver content possessed higher hardness and tensile strength due to solid solution strengthening.

The fracture in magnesium alloys generally originates from the deformation twinning. However, the formation of deformation twinning is prevented by grain refinement. A fine-grained material is harder and stronger than one which is coarsely grained, because it has a greater total grain boundary area to impede dislocation motion. For many metals with equiaxial grains, the yield strength which varies with grain size can be represented by Hall-Petch equation ($\rho = \rho_0 + \mathrm{k}\mathrm{d}^{1/2}$) without considering the second phases or precipitates. In this expression, d is the average grain

size, ρ_0 is the yield stress of a single crystal, and k is a constant [206, 207] The k increases with the increase of the Taylor factor [208]. The Taylor factor generally depends on the number of the slip systems. Because the slip systems are limited and the Taylor factor is larger for h.c.p. (hexagonal close packing) metals than for f.c.c. (face centered cubic) and b.c.c. (body centered cubic) metals, h.c.p. metals exhibit the strong influence of grain size on strength. Therefore, it is suggested that high strength can be attained in the fine-grained magnesium alloys [209]. So the grain size of Mg-Ag alloys is inversely proportional to the hardness as well as the yield strength.

The Mg-Ag alloys after thermomechanical processing possess higher hardness and strength than the as cast alloys. When comparing the tensile properties between these thermomechanically processed Mg-Ag alloys, the grain size will be not the only influence factor. The factor of texture influence also should be involved, e.g., Schmid factor.

In total, the linear relationship of hardness of Mg-Ag alloys can be represented by the following formula:

$$H = a + b \cdot f\left(\frac{1}{x}\right) + c \cdot f(y) + d \cdot f(z) \qquad \text{Eq. 5.1}$$

The x is the grain size and y is the precipitation amount and z is the solid solubility of silver in magnesium. The a is the basic value of pure Mg. The b, c and d are constant values.

The correlation between grain size, hardness, yield strength and elongation was statistically analyzed and displayed in Fig. 5.1. As predicted by the Hall-Petch relation, the hardness is negatively correlated to grain size (Pearson correlation coefficient (PCC) = -0.555, p<0.05) and positively to the amount of second phases (PCC = 0.665, p<0.005). Further correlations for this alloying system were found between yield strength and hardness (PCC = 0.477, p<0.05). Here the main influencing factor is the grain size (PCC = -0.573, p<0.05), which shows a negative correlation to yield strength. And the yield strength and elongation are positively correlated (PCC = 0.596, p<0.01).

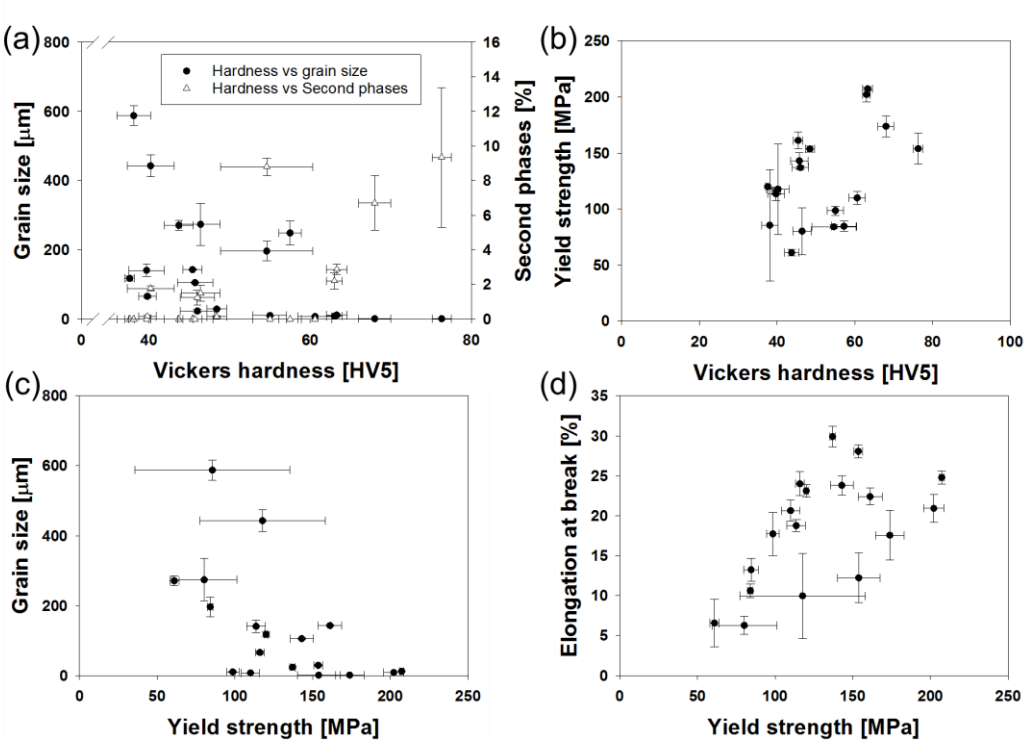

Fig. 5.1: Correlations between grain size and hardness or second phases and hardness (a), yield strength and hardness (b), grain size and yield strength (c), and elongation and yield strength (d).

5.2.2 Short time annealing and mechanical properties

Dynamic recrystallization during hot deformation processing resulted in grain refinement [133, 135, 147]. However, the rolling speed was fast in this study. According to the metallography analysis of the as rolled Mg-Ag alloys, no dynamic recrystallization happened during the rolling. Instead, many twins existed in the as rolled Mg-Ag alloys. The rolling of Mg-Ag alloys with high silver content at low temperature caused inhomogeneous grains due to precipitation restriction. When the rolling temperature was near the melting point, the grains in the as rolled Mg-Ag alloys became large.

The grains in the as rolled Mg-Ag alloys were refined by static recrystallization which occurred during the subsequent annealing. However, the final mechanical properties can deteriorate during the following heat treatment [142], if the parameters are not optimized. The general annealing eliminated all twins in Mg-Ag alloys, but the grains were still as big as that in the as rolled Mg-Ag alloys. If the annealing temperature was much high, secondary recrystallization of grains could happen. As a result, the large grains in Mg-Ag alloys decrease the hardness as well as tensile strength.

Studies identified that the deformation and annealing conditions can influence the speed of microstructure evolution to reach a stable status [142]. During the annealing, many nuclei appeared along the twins and grain boundaries. The stored energy in the as rolled Mg-Ag alloys drove the growth of grains during the static recrystallization. When the rolling temperature was higher, the grains were bigger and the twins inside were also less than that of the other Mg-Ag alloys. The increase of temperature results in a decrease of the nucleation site as well as the stored energy. The static recrystallization rate of the Mg-Ag alloys rolled at higher temperature is slower, especially when the annealing temperature is lower than the rolling temperature. The Mg-Ag alloys rolled at high temperature should use the equal or a higher annealing temperature in the annealing procedure. Moreover, with the increase of silver content in Mg-Ag alloys, the melting point becomes lower according to the simulated Mg-Ag phase diagram. The rolling temperature of Mg-Ag alloys with higher silver content is more near the melting temperature relatively, so the stored energy is less, thus, the static recrystallization is slow.

Overall, a long time annealing causes abnormal grain growth and the dropping of hardness as well as the deterioration of tensile strength. In this case, short time annealing can be applied to obtain small grains via static recrystallization. Through the optimization of the short time annealing, a precise regulation of microstructure can be achieved. The tensile strength of Mg-Ag alloys after short time annealing is much higher than that after general annealing. Meanwhile, the elongation is still sufficient for Mg-Ag alloys as biodegradable materials.

5.2.3 Microstructure and degradation behavior

There are different types of corrosion including uniform corrosion, galvanic corrosion, pitting corrosion, crevice corrosion, intergranular corrosion, erosion corrosion and stress corrosion in the natural environment [30]. The common degradation types for magnesium alloys as implant materials in physiological conditions are galvanic degradation and stress degradation. The manifestations are pitting or uniform degradation.

The main factor that influences the degradation behavior of Mg-Ag alloys is the silver composition and microstructure. Since silver has low solubility in magnesium at low temperature [122], many second phases or precipitates form during casting or thermomechanical processing [17]. The $Mg_{54}Ag_{17}$ has much higher positive potential than that of the matrix, so it has big influence on the degradation of Mg-Ag alloys [126]. Moreover, the second phases or precipitates influence the degradation behavior more than the factor of grain size. Some studies mentioned that the existence of Al-rich $Al_{11}RE_3$, β-$Mg_{17}Al_{12}$ or Mg_2Ca strongly influenced the

degradation process and enhanced the corrosion resistance of magnesium alloys [44, 126, 210]. On the contrary, many $Mg_{54}Ag_{17}$ facilitated pitting and a high degradation rate in Mg-Ag alloys. The degradation rate increases linearly with increasing quantity of precipitates [211].The Mg-Ag alloys with a large number of second phases or precipitates degraded rapidly, which is adverse to the further mechanical integrity and tissue healing progress. Micro-galvanic degradation is the main degradation mechanism in Mg-Ag alloys.

Heat treatment affects the microgalvanic degradation behavior significantly [44]. Homogenization and solution treatment (T4) decreased the degradation rate of Mg-Ag alloys and relieved the pitting very well by elimination of second phases or precipitates. However, the degradation rates of the as cast Mg-Ag alloys were still unstable even though homogenization was done, because the silver distribution was not homogeneous in the as cast alloys, especially when the silver content was high. Only part of the Mg-Ag alloys with high silver content was relieved by homogenization treatment.

The grain size has influence on the degradation rate that some magnesium alloys with finer grains have a lower degradation rate [127]. The AZ series alloys with the finest grains have the best degradation behavior in long periods of immersion test in PBS [127]. ECAP AE21 also has low degradation rate because of ultra-fine grains and homogeneous distribution of alloying elements in the matrix compared to the extruded material [126]. However, fine grains did not bring a lower degradation rate in Mg-Ag alloys. Hence, the degradation behavior of Mg-Ag alloys is mainly related to the amount of second phases or precipitates followed by the homogeneity of silver. As shown in Fig. 5.2, the degradation rate is mainly influenced by the amount of second phases (PCC = 0.718, $p<0.0005$), whereas no correlation to the grain size can be determined ($p>0.05$).

The degradation morphology in immersion tests is more related to the microstructure, especially the precipitates in grains and along the grain boundaries and twins. The precipitates cause localized degradation phenomenon [211]. Although the twins in the as rolled Mg-Ag alloys did not influence the degradation rate obviously, the surface of the as rolled Mg-Ag alloys was rough after immersion tests. The pits and rough surface of Mg-Ag alloys are due to the existence of precipitates and their distribution. The pits and rough surface can induce fast loss of mechanical integrity at early stage of implantation.

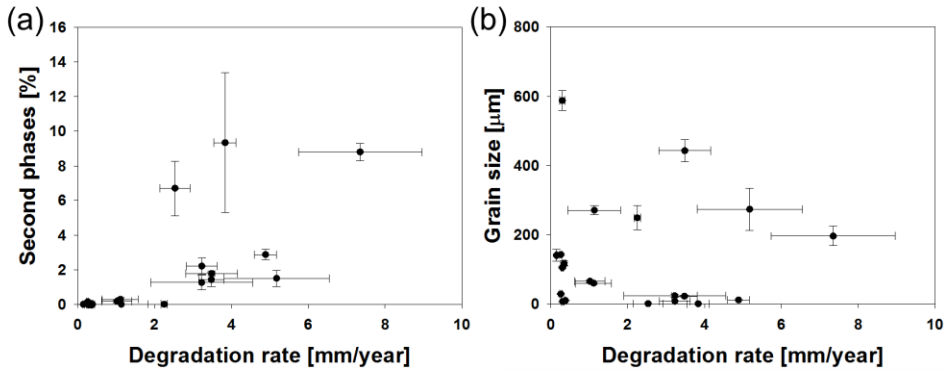

Fig. 5.2: Correlation between amount of second phases and degradation rate (a), and grain size and degradation rate (b).

5.2.4 The optimal microstructure and suitable thermomechanical processing

There are specific relationships between grain size, second phases/precipitates, degradation behavior and tensile properties of Mg-Ag alloys. The fine grains in Mg-Ag alloys have weak influence on the degradation rate but they have contribution to hardness and mechanical properties. The second phases or precipitates also promote the hardness and strength much. However, a high amount of second phases or precipitates in Mg-Ag alloys accelerates the degradation rate. The elimination of precipitates suppresses the degradation well, even though a slight increasing of degradation rate is observed with increasing of silver in Mg-Ag alloys without precipitates. The stability of degradation is related to the silver homogeneity. Moreover, the mechanical integrity is related to degradation behavior. Low degradation rate and uniform morphology retard the rapid loss of mechanical integrity.

The fine-grained microstructure without precipitates is the best for Mg-Ag alloys as biodegradable implant materials. An appropriate combination of thermomechanical processing and heat treatment is necessary for Mg-Ag alloys to control the precipitation and grain refinement [209], resulting in significant improvement of mechanical properties and good degradation resistance. However, not all thermomechanical processing are suitable for Mg-Ag alloys. Some studies mentioned that reduction of the temperature of thermomechanical processing can achieve ultrafine grains or better degradation resistance for specific magnesium alloys [31, 156, 192]. However, the process at such low temperature will result in high degradation rate of Mg-Ag alloys. The silver content determines suitable thermomechanical processing. In hot extrusion, magnesium alloys can be extruded at the temperature from 350 to

450°C [212], so there is possibility to obtain the microstructure without precipitates by elevating temperature. However, the grains in the extruded Mg-Ag alloys with high silver content will be very large and rough, which will lower the tensile properties. For FSP, it is feasible to obtain ultrafine microstructure without precipitates by optimizing its parameters, but the cooling procedure after FSP should be fast to avoid precipitation. Similarly, for the rolling processing, the Mg-Ag alloys with high silver content should be processed at high temperature at high temperature to avoid the precipitates. Several authors have recently highlighted the increase in grain size that occurs following the subsequent annealing, or slow cooling, of hot-rolled magnesium alloys [139-141]. Researchers found that annealing of as rolled AZ31 at 400°C for 1 h increased the grain size from between 5 and 10 μm to over 50 μm [139]. Hence, it is needed to adjust the microstructure by short time annealing at high temperature to get fine grains. Each thermomechanical processing has advantages, but it always takes process optimization to obtain a good material.

5.3 Cytocompatibility, mineralization and antibacterial properties

5.3.1 The relationship between degradation and cytocompatibility

In cytotoxicity tests, the extruded and extruded+T4 Mg-Ag alloys (Q6 and Q8) were applied since the alloys included a wide range of degradation rates. Meanwhile, most of them possess low enough degradation rate in DMEM with10% FBS.

The degradation rates of Mg-Ag alloys influence the pH values and osmolalities of the medium. During the degradation, although the pH value of medium can reach a stable status in specific time, the pH value of extracts from the alloys with fast degradation rate is still higher than the one from the alloys with relative low degradation rate. This trend is the same for osmolality, since more magnesium ions released from Mg-Ag alloys when the degradation rate is higher. Those ions did not form degradation products in short time but existed in extracts. Moreover, the high degradation rate can also increase the silver concentration in medium.

The cytocompatibility and tolerance of cells and tissues to degradation rate, is closely related to pH, osmolality [69]. High osmolality or concentration of magnesium ions can cause osmotic shock in human cells [185]. Cells can also be hindered by hydrogen generation and fail to attach to the surface. Therefore, a high degradation rate is not desired for magnesium alloys as

orthopedic implant materials. The degradation rate should be controlled to meet the cytotoxicity criteria first. Moreover, the amount of Ag which is tolerable for cells should be revealed.

The pH values of extracts from Mg-Ag alloys with high degradation rates (more than 2.25 mm/year) normally maintain at a high level (Fig. 4.21 and 4.22). The high pH values are adverse to the cell viability. During the degradation of Mg-Ag alloys, the Mg concentration in extracts increased substantially compared to cell culture medium (Table 4.3). It is more related to the osmolality of extracts than the others. For Q6 and Q8, when the increment of osmolality was more than $0.1 \cdot kg^{-1}$ compared to the osmolality of cell culture medium, the Mg concentration can reach at least 1000 mg/L. Nearly no human primary osteoblast could survive in the extracts with such high Mg concentration (Fig. 4.27). Moreover, the osmolality of DMEM+10% FBS is about $345 \cdot kg^{-1}$ in cell culture conditions. For most of the Mg-Ag alloys with a degradation rate of more than 2.25 mm/year, the osmolality has an increase of 35%. In this case, all human primary osteoblasts died in adhesion test.

The Q8 extract with 10.4 mg/L Ag has no potential cytotoxicity to human primary osteoblasts. The corresponding degradation was calculated to be 0.35 mm/year (Table 4.3). From the point view of silver concentration, the Q6 can have a higher degradation rate which should be tolerable to cells. When the degradation rate is below 0.35 mm/year, the highest increment of osmolality is 26% which allows human primary osteoblasts attach and survive in adhesion tests. Overall, when the degradation rate is lower than 0.35 mm/year for example of Q8. The silver concentration as well as pH and osmolality will not bring cytotoxicity to cells. Meanwhile, during the degradation, the released silver ions can react with bacteria effectively, so the Mg-Ag alloys show antibacterial properties.

5.3.2 Mineralization behavior

In mineralization assay, there are two different ways, inorganic mineralization and biomineralization, to form HA. The green areas are from inorganic mineralization by cell culture medium and the green particles are from biomineralization by HUCPV cells or human primary osteoblasts. Pure Mg can be covered by HA rapidly via inorganic mineralization. However, no HA formed via inorganic mineralization was found on Mg-Ag alloys. It does not mean that there was no inorganic mineralization process on Mg-Ag alloys. Further study is displayed in the degradation mechanism part.

DAPI staining on the basis of mineralization assay showed the status of nuclei of HUCPV cells and human primary osteoblasts in situ. The integral nuclei means that HUCPV cells and human primary osteoblasts grow and proliferate well on the extruded pure Mg and extruded+T4 Q6 and Q8 discs. As cytotoxicity assay, it also confirms the activity of cells on Mg-Ag alloys.

The released silver has influence on the synthesis of HA by cells. With increasing of silver content in Mg-Ag alloys, the productivity of HA by HUCPV cells and human primary osteoblasts decreased. This means that the released silver hindered the mineralization activity of HUCPV cells and human primary osteoblasts *in vitro*.

5.3.2 Antibacterial properties

Antibacterial properties are influenced by not only silver concentration but also pH value. However, high pH value can cause cytotoxicity to cells, so pure Mg cannot rely on a high pH to achieve its antibacterial effect, regardless of cytotoxicity.

Silver release plays a key role in eliminating multiple bacteria and preventing biofilm formation [111]. The novel point is that the addition of silver to pure Mg significantly improved the antibacterial effect in a dynamic environment because silver was released from the matrix continuously during the degradation of Mg-Ag alloys. The released silver particles and ions can react with bacteria effectively, so the Mg-Ag alloys have better antibacterial properties than pure Mg [17]. Silver release is determined by the degradation rate and the amount of silver in magnesium. When the degradation rate or silver content is high, many silver particles can be released from Mg-Ag alloys. Hence, a higher degradation rate or silver content can bring better antibacterial properties.

In the biofilm assay, the *in vitro* design of the dynamic system with large numbers of bacteria in the flowing medium represents harsh conditions, although the *in vivo* conditions normally show clearly lower bacteria concentrations. The flowing conditions and pH control system can exclude the pH effect of the corroding Mg alloys to bacteria as much as possible. Pure Mg did not show satisfactory antibacterial properties under these conditions. Based on the viability and total amount of bacteria on pure Mg discs, there are still considerable numbers of live bacteria. From the overview of the biofilms on the discs, it appears that pure Mg still has the potential to form many colonies or even a biofilm layer in suitable conditions, although the total amount of bacteria is less than that on the negative control groups [213]. Admittedly, the pH plays an

important antibacterial role due to the alkaline environment created during degradation [92-94], so the pure Mg has bacteriostatic effect to some extent.

When the degradation rate was high, a large amount of silver released. As a result, they showed good antibacterial properties. However, the viability of bacteria was not as low as expected, e.g., 99.9% reduction. One reason is that a large portion of silver flowed away with the medium. Another reason is that a large amount of bacteria (10^6/mL) exists in the medium, which indicates a harsh condition. The extruded+T4 Q6 and Q8 got better antibacterial properties than pure Mg. The extruded+T4 Q8 released more silver (two-fold) than the extruded+T4 Q6, but bacteria viability decreased only 4 percent due to the flow system of bioreactor. In this case, less released silver ions reacted with the bacteria which attached to the surface of discs. According to the decreasing trend of bacteria viability, if we continue to increase the silver content in magnesium, e.g., 15 wt.%, more effective antibacterial properties of Mg-Ag alloys could theoretically be achieved in the flow system of bioreactor. However, the degradation rate approaches its limit at an acceptable range for orthopedic implants [2]. From the viewpoint of morphology, the extruded+T4 Q6 and Q8 have more homogeneous and flatter degradation surfaces and lower pitting trend than pure Mg in the flow chamber according to the 3-D images, even though the low pH (7.2) of BCM has an adverse effect on the stability of the degradation layer.

Silver ions can bind strongly and build complexes with thiols, metallothionein, albumins, and macroglobulins *in vivo* [115, 214, 215]. The antibacterial properties of Mg-Ag alloys are related to the silver concentration in the infection site, which is determined by the amount of silver in the Mg-Ag alloy and its release rate. If only a small amount of silver was released, the remaining silver would be insufficient to inhibit bacteria. In contrast, if more active silver ions released, the antibacterial properties would be more effective [107], so it is better to alloy silver in pure Mg as much as possible, to ensure effective antibacterial properties on the basis of a controllable degradation rate. However, the total silver used in the human body should not exceed the amount that can cause arygia.

5.4 Degradation mechanism

In this part, the degradation behavior of Mg-Ag alloys in different degradation environments was investigated, since not only the microstructure of Mg-Ag alloys influences the degradation behavior but also the degradation environment can change it. In this part, the influence of

inorganic substance and proteins on selected Mg-Ag alloys (the extruded Q6, extruded Q8, extruded+T4 Q6, extruded+T4 Q8, extruded+T6 Q6 and extruded+T6 Q8) was revealed.

5.4.1 Environment influence on pH, osmolality and degradation rate

In immersion tests, a much high degradation rate brought a high and stable osmolality increment of extracts. During the degradation, the abundant Mg^{2+} combined with HCO^{3-} and dissolved CO_2 to form $Mg(CO_3)(H_2O)_3$ crystals, so these extracts did not show much higher osmolality compared to the others. Generally, for the alloys without much high degradation rate, their osmolality increments were dropping gradually, since these Mg-Ag alloys have a decrease of degradation rate with time.

The degradation rates showed that the composition of solutions had big influence on the degradation behavior. Mg-Ag alloys with low degradation rate had a stepped decreasing of degradation rate in solution 9, 8 and 7, because inorganic mineralization and protein adhesion hindered the degradation process. The composition of solution 7, 8 and 9 is listed in Table 5.1. When the degradation rate of Mg-Ag alloys was very high, they had no difference in solution 7 and 8. It means that the inorganic mineralization cannot retard the degradation further when the degradation rate was very high. Some alloys exhibited higher degradation rate in solution 9 than in solution 7 and 8, since no proteins protected the surface in solution 9. However, it did not work for extruded+T6 Q8 in solution with protein. When the degradation rate of Mg-Ag alloys, e.g., extruded+T4 Q6, was low enough, the proteins did not hinder the degradation further too. Hence, the proteins can only protect the Mg-Ag alloy when the degradation rate is in a specific range, for instance from 1.46 to 10.28 mm/year in the solution 9 (HBSS). Moreover, the amount of solvus silver in Mg-Ag alloys also influences the degradation behavior in specific solution. The extruded+T4 Q6 has the same degradation rate with the extruded+T4 Q8 in solution 8 (HBSS + 10% FBS). Whereas, in solution 9 (HBSS), the extruded+T4 Q8 has higher degradation rate than the extruded+T4 Q6.

Table 5.1: Composition of the solution 7, 8 and 9 for the immersion tests.

Solutions	Composition
7	HBSS + 10% FBS + 39.9 mM $NaHCO_3$ + 1.8 mM $CaCl_2 \cdot 2H_2O$ + 0.8 mM $MgSO_4 \cdot 7H_2O$
8	HBSS + 10% FBS
9	HBSS

5.4.2 Degradation and inorganic mineralization

To understand the influence of inorganic substances on degradation, the composition of different solutions is listed in Table 3.2. The basic solution HBSS has no Ca^{2+}, Mg^{2+} and SO_4^{2-} ions inside. In cell culture conditions, CO_2 will dissolve into solutions where CO_2 can form H_2CO_3, so the existence of CO_2 will influence the pH value and balance some ions in solutions (Eq. 5.2). As a result, the pH of solutions in cell culture conditions will be lower than that in the atmospheric environment.

$$CO_2 + H_2O \leftrightarrow H_2CO_3 \leftrightarrow H^+ + HCO_3^- \leftrightarrow 2H^+ + CO_3^{2-} \quad \text{Eq. 5.2}$$

Normally, during the early stage of immersion tests, the magnesium alloys degraded quickly [19]. First, the degradation procedure of magnesium follows these equations [57]:

Anodic reaction: $$Mg \rightarrow Mg^{2+} + 2e^- \quad \text{Eq. 5.3}$$

Cathodic reaction: $$2H_2O + 2e^- \rightarrow H_2 \uparrow + 2OH^- \quad \text{Eq. 5.4}$$

$$Mg^{2-} + 2OH^- \rightarrow Mg(OH)_2 \quad \text{Eq. 5.5}$$

However, there are considerable amount of Cl^- ions in HBSS. As one important factor that causes the fast degradation rate of magnesium alloys in physiological solution [7, 49, 50, 73, 216], they react with the $Mg(OH)_2$ by transforming the protective $Mg(OH)_2$ into soluble $MgCl_2$ [12, 217]. The specific process is the following formula:

$$Mg(OH)_2 + 2Cl^- \rightarrow MgCl_2 + 2OH^- \quad \text{Eq. 5.6}$$

The reaction between Cl^- and $Mg(OH)_2$ results in excess OH^- ions in the solutions, which causes the rising of the pH near the surface and in the bulk medium.

The HCO_3^- ions balance pH well as buffer and provide a more alkaline environment near the surface. The addition of HCO_3^- in HBSS increases the pH value and osmolality of initial solution. The solution containing $NaHCO_3$ shows alkaline values approaching the pH value of body fluid in physiological conditions. Relatively, the pH increments of solutions containing HCO_3^- were low during the degradation (Fig. 4.41). The HCO_3^- ions are observed to stimulate the degradation of magnesium alloys at the early immersion stage. [40]. The HCO_3^- can react with Mg^{2+} generated during magnesium dissolution [60]. The reaction between HCO_3^- and Mg^{2+}

results in the formation of insoluble carbonates which is $Mg(CO_3)(H_2O)_3$ according to the small angle X-ray patterns (Fig. 4.47 a). The total reaction is:

$$Mg + HCO_3^- + 4H_2O \rightarrow Mg(CO_3)(H_2O)_3 + OH^- + H_2 \uparrow \quad \text{Eq. 5.7}$$

The precipitation of $MgCO_3(H_2O)_3$ is more likely to form when $NaHCO_3$ and CO_2 exists, rather than the precipitation of $Mg(OH)_2$ in the neutral range of pH as 7-8 [54]. When there is high CO_2 concentration, e.g., in cell culture conditions, the CO_2 provides HCO_3^- by dissolving into solutions, continuously. In cell culture conditions, most of the $Mg(OH)_2$ transforms into $Mg(CO_3)(H_2O)_3$, continuously. As a result, this kind of crystal precipitates is the main degradation products as seen on the surface of the extruded+T6 Q6 and Q8. However, such precipitation of insoluble magnesium carbonate crystals can hardly retard the degradation process of the extruded+T6 Q6 and Q8.

According to the Eq. 5.7, many free OH^- ions are generated, which dramatically promotes the accumulation of OH^- further. Moreover, it was mentioned that the SO_4^{2-} ions can also stimulate the magnesium dissolution as well as HCO_3^- at the early stage of degradation [40, 50]. The SO_4^{2-} ions also directly influence the morphology of the interface layer by increasing its heterogeneity [60].

In total, due to the fast degradation rates of Mg-Ag alloys at the early stage and the effect of Cl^-, HCO_3^- and SO_4^{2-} ions, the surfaces of Mg-Ag alloys possessed relative high pH value. In the solutions containing Ca^{2+} and $H_2PO_4^-/HPO_4^{2-}$ ions, some complicated compounds $Mg_xCa_y(PO_4)(OH)_z$ including HA [$Ca_{10}(PO_4)_6(OH)_2$] and $Mg_3(PO_4)_2$ are likely to nucleate and grow rapidly on the surface of magnesium alloys due to the high pH value and existence of Mg^{2+} ions [19, 218, 219]. In general, the reaction among Mg^{2+}, Ca^{2+} and $H_nPO_4^{(3-n)-}$ (representing various phosphate ions, where n = 0, 1 or 2), can be described primarily by the following formula [19, 56, 218, 220]. The x, y and z could be zero or fraction.

$$xMg^{2+} + yCa^{2+} + H_nPO_4^{(3-n)-} + (n+z)OH^- \rightarrow Mg_xCa_y(PO_4)(OH)_z + nH_2O \quad \text{Eq. 5.8}$$

The $Mg_xCa_y(PO_4)(OH)_z$ can induce rapid passivation on the surface [40]. The rapid formation of insoluble protective degradation layer can retard degradation process effectively [19].

In solution 7, enough Ca^{2+} ions were provided on the basis of the existing $H_2PO_4^-/HPO_4^{2-}$. A high pH value was obtained due to degradation and stimulation to Mg-Ag alloys by ions. As a result,

the compact degradation layer containing $Mg_xCa_y(PO_4)(OH)_z$ can preferentially form rapidly to protect the extruded+T4 Q6 and Q8 well. Hence, the co-addition of $NaHCO_3$, $MgSO_4$ and $CaCl_2$ in HBSS contributes to retard the degradation of the extruded+T4 Q6 and Q8, effectively. Moreover, the trend of pitting is also significantly retarded.

In mineralization assay, it can be observed that HA formed on the surface of pure Mg, which protects the pure Mg well. Most of the HA on pure Mg formed by inorganic mineralization. However, most of the protective products on the surface of the extruded+T4 Q6 and Q8 is magnesium/calcium phosphates salts instead of HA, according to the degradation rates, EDS analysis and mineralization assays. This kind of magnesium/calcium phosphates plays an important role in suppressing the degradation rate by hindering the aggressive action of chloride ions [127]. The mechanism to slow down degradation rate is different from that of the pure Mg or even other magnesium alloys in such conditions.

In total, the addition of $NaHCO_3$, $MgSO_4$ and $CaCl_2$ together in HBSS decreased the degradation rate by forming magnesium/calcium phosphates compounds even though the concentration of Cl^- ions increased in the solution after the addition of $CaCl_2$. Moreover, the formation of calcium phosphates compounds *in vivo* could also account for the decrease in the degradation process [7, 221]. Various studies have shown that the degradation layer containing such magnesium/calcium phosphate compounds on magnesium can promote osteoinductivity and osteoconductivity, predicting good biocompatibility of magnesium [7, 19, 38]. In addition, magnesium binds strongly to phosphates. Thus, it influences the mineralization of bone tissue through its control of hydroxyapatite (HA) or magnesium/calcium phosphate formation [30, 222].

5.4.3 Interfacial behavior of proteins

The BSA concentration is about 23 mg/mL in FBS. The surfaces of Mg-Ag alloys with low degradation rate have very strong adsorption to proteins such as BSA molecules from FBS. The proteins can be adsorbed on the surfaces through a complex process that involves Van der Waals force and chemisorption. Proteins such as albumin possess a strong tendency of structural rearrangements when adsorbed on a nonbiological surface, depending on the surface properties [223]. The negatively charged carboxylate groups of the proteins behave like anchoring sites between the proteins and surface [63, 224]. The interactions between proteins and surfaces depend on the properties of the proteins as well as other parameters such as the pH value, temperature and the concentration of other ions and so on [63, 225]. The chelation of proteins and ions in the solution can form organometallic complexes which attaches on the

surface of Mg-Ag alloys. It influences the transport of anionic and cationic charges in the local environment [63, 64, 226]. The protein layer may hinder the diffusion of ions to some extent [226-229]. As a result, the interactions between proteins and the implant surfaces change the degradation process [63, 64, 67, 230].

The presence of proteins can significantly regulate the crystallization of inorganic hard tissues under physiological conditions. The precipitation of large-sized HAP is greatly retarded by FBS and only the nano-sized ACP (amorphous calcium phosphate) is formed. It also shows that FBS can suppress the aggregation of nano-calcium phosphate clusters. Furthermore, FBS can also retard the phase transformation of unstable amorphous calcium phosphate to crystallized hydroxyapatite in biological milieus [231]. That could be the reason that the XRD patterns of degradation products of Mg-Ag alloys in solutions with FBS are wide. Some of the $Mg(CO_3)(H_2O)_3$ on Mg-Ag alloys is amorphous when FBS exists in solution. However, the HA produced by cells is large and not influenced by FBS. The albumin may form a blocking layer on the surface in the first hours of exposure and the degradation layers formed consist of amorphous apatite [39, 232]. Hence, proteins can hinder the degradation and the amorphous magnesium carbonate may also suppress the degradation of the extruded+T4 Q6 and Q8. However, the FBS cannot retard the degradation further on the basis of very low degradation rate in HBSS, which may due to the BSA which can transport metals or ions. Moreover, when the degradation rate is very high, the proteins could agglomerate and cannot prevent the degradation anymore. This should be related to high pH value and osmolality of medium.

5.4.4 Interaction of degradation and proteins

It is generally believed that some kinds of metal ions, e.g., Ag, can react with proteins by combining the thiol groups of proteins, which is the main principle of silver staining. It was normally developed to detect proteins ultrasensitively in polyacrylamide gels via autocatalytic reduction of silver [233]. The colors of silver staining may correlate with the development of silver grains of characteristic sizes. The silver grains on proteins can be yellow band (21-39 nm) or brown bands (17-35 nm) [234]. The coloration of silver-stained proteins bands in polyacrylamide gels is caused by light scattering from silver grains of characteristic sizes [234]. In the brown extracts from the extruded+T6 Q6 and Q8 (Fig. 4.50), the size of silver particles on proteins should be 17-35 nm. The only difference to the silver staining is that silver particles attached on proteins directly without recovery procedure of silver ions.

The silver ions have remarkably reactive antibacterial properties instead of the zero-valent silver [235, 236]. The antibacterial properties of nano-silver particles are due to the release of silver ions because of their high specific surface area and the production of reactive oxygen species (ROS). The nano-silver based proteins are of broad-spectrum antibacterial activity towards the bacterial strains such as *Staphylococcus aureus*, *Serratia marcescens*, *Pseudomonas aeruginosa*, *Escherichia coli* and *Klebsiella pneumoniae* and lower propensity to induce microbial resistance than antibiotics [237, 238].

The adhesion of proteins on medical implant devices can support bacterial growth [63]. Suppression of bacterial growth for a long term by alkaline pH from magnesium degradation is not really possible, as enough alkaline pH cannot be maintained under physiological conditions. Therefore the approach to use Mg-Ag alloys can provide a sustained activity against bacteria. Moreover, FBS is reported to hinder the antibacterial activity of silver [239]. However, our previous research identified that the Mg-Ag alloys has better antibacterial properties than the pure Mg in the presence of FBS [17], even though the proteins layer may hinder the diffusion of ions to some extent [226-229]. There is surface complexation between BSA and silver, but there is also exchange of these surface complexes with BSA molecules in the solution, which is one of the methods that silver released to solution as well as direct releasing [240]. Combining the conclusions about degradation above, a schematic model of degradation mechanism of Mg-Ag alloys with low degradation rate can be sketched out (Fig. 5.3).

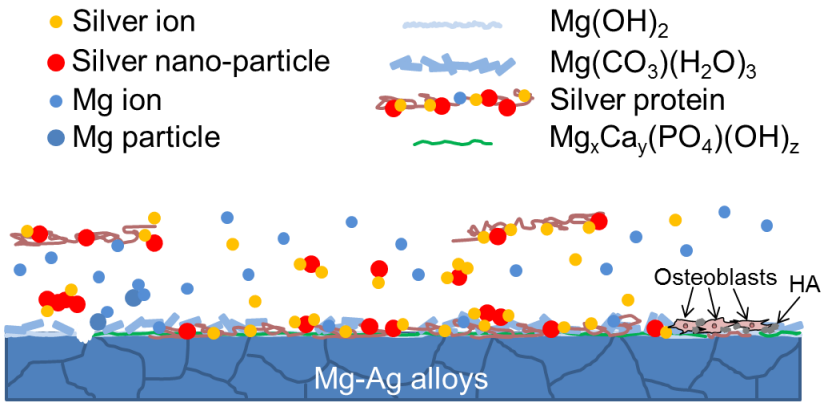

Fig. 5.3: Degradation schematic of Mg-Ag alloys with osteoblasts in physiological conditions *in vitro*. The silver releases from Mg-Ag alloys directly during degradation.

6. Summary and conclusion

1. With the increase of silver content, the grain size of as cast Mg-Ag alloys decreased and the amount of second phases $Mg_{54}Ag_{17}$ increased. Hardness and strength are related to precipitation, grain size and solvus of silver in magnesium. Generally, more precipitates, smaller grains and higher silver solvus can bring higher hardness and strength to Mg-Ag alloys.

The degradation rate is mainly influenced by second phases/precipitates followed by solvus of silver in magnesium. A high amount of precipitates cause severe pitting. With the dissolving of precipitates, the pitting transferred into homogeneous degradation, gradually. Twins had influence on degradation morphology rather than degradation rate. When the silver improved to 10 wt.% in magnesium, the degradation rate cannot be reduced to tolerable range of cells even after T4 treatment, even though the pitting was relieved, obviously.

The refining of grains and eliminating of precipitates were found to be an effective method to improve tensile properties, decrease degradation rate and relieve the pitting of Mg-Ag alloys. The extruded+T4 Q6 and Q8 showed low degradation rates as pure Mg and more homogeneous morphologies than pure Mg.

2. The influences of microstructure and silver content on the cytotoxicity and antibacterial properties of Mg-Ag alloys were revealed. The extruded+T4 Q6 and Q8 have no discernible *in vitro* cytotoxicity to human primary osteoblasts compared to pure Mg. The antibacterial properties depend on silver release. By increasing the silver content and controlling the degradation rate in a reasonable range, the extruded+T4 Q6 and Q8 showed better antibacterial properties than pure Mg in dynamic environment with abundant bacteria. The HUCPV cells and human primary cells survived and produced HA particles on the surface of the extruded pure Mg and extruded+T4 Q6 and Q8.

3. The degradation mechanism of Mg-Ag alloys was revealed by immersion tests, mineralization assay and further characterizations. The ions of HCO^{3-}, Cl^{-}, SO_4^{2+}, Ca^{2+} and $H_2PO_4^{-}/HPO_4^{2-}$ played key role in the degradation procedure. The HCO_3^{-}, Cl^{-} and SO_4^{2-} ions stimulated the degradation of Mg-Ag alloys to obtain a relative high pH near the surface at the initial stage. The high pH value contributed to the formation of $Mg_xCa_y(PO_4)(OH)_z$ on Mg-Ag alloys via inorganic mineralization, instead of HA which formed on pure Mg. However, the compounds only protected Mg-Ag alloys when the degradation rate was less than 3.2 mm/year in HBSS with 10%

FBS. Abundant Mg^{2+} ions and HCO_3^- formed $Mg(CO_3)(H_2O)_3$ as main degradation products on Mg-Ag alloys with high degradation rate. The FBS attached on the surface of Mg-Ag alloys to retards the degradation rate, only when the degradation rate was in specific range from 1.46 to 10.28 mm/year in HBSS. The released nano-scale silver particles combined with proteins from FBS.

Conclusion: Different thermomechanical processing and heat treatments had great influence on the microstructure evolution. An appropriate processing can be chosen according to the silver content. Hot extrusion, FSP and rolling are suitable processing for Q6. FSP and rolling is flexible for Q8. There is a window between no potential cytotoxicity and good antibacterial effect. It can be achieved by dissolve silver and adjust degradation rate. The degradation behavior is mainly influence by microstructure and degradation environment.

7. Outlook

- The parameters of thermomechanical processing routes should be optimized precisely further to obtain an ideal microstructure. Texture influence to mechanical properties should be analyzed. It is helpful to choose suitable processing route.
- Both the mechanical strength and degradation resistance can be improved further on the basis of the obtained results so far.
- The cytotoxicity and antibacterial tests could be carried out in a human cell and bacteria co-culture system.
- To explore more detailed degradation mechanism and find the correlation of degradation behavior *in vitro* and *in vivo*, the immersion condition should more complex and approach the human body environment.

References

[1] J. Velazguez, A. Jimenez, B. Chomon, T. Villa, Nutrition reviews, 57 (1999) 227.
[2] C. Seal, K. Vince, M. Hodgson, IOP conference series: materials science and engineering, IOP Publishing, 2009, pp. 012011.
[3] A. Sáenz, E. Rivera, W. Brostow, V.M. Castaño, Journal of Materials Education, 21 (1999) 267-276.
[4] Y. Ding, C. Wen, P. Hodgson, Y. Li, Journal of materials chemistry B, 2 (2014) 1912-1933.
[5] P. Zartner, R. Cesnjevar, H. Singer, M. Weyand, Catheterization and Cardiovascular Interventions, 66 (2005) 590-594.
[6] F. Witte, J. Fischer, J. Nellesen, H.-A. Crostack, V. Kaese, A. Pisch, F. Beckmann, H. Windhagen, Biomaterials, 27 (2006) 1013-1018.
[7] F. Witte, V. Kaese, H. Haferkamp, E. Switzer, A. Meyer-Lindenberg, C. Wirth, H. Windhagen, Biomaterials, 26 (2005) 3557-3563.
[8] M.P. Staiger, A.M. Pietak, J. Huadmai, G. Dias, Biomaterials, 27 (2006) 1728-1734.
[9] X.-N. Gu, Y.-F. Zheng, Frontiers of Materials Science in China, 4 (2010) 111-115.
[10] G. Song, S. Song, Advanced Engineering Materials, 9 (2007) 298-302.
[11] F. Witte, H. Ulrich, M. Rudert, E. Willbold, Journal of biomedical materials research Part A, 81 (2007) 748-756.
[12] Z. Li, X. Gu, S. Lou, Y. Zheng, Biomaterials, 29 (2008) 1329-1344.
[13] Y. Xin, T. Hu, P. Chu, Acta biomaterialia, 7 (2011) 1452-1459.
[14] K.A. Athanasiou, C.M. Agrawal, F.A. Barber, S.S. Burkhart, Arthroscopy: The Journal of Arthroscopic & Related Surgery, 14 (1998) 726-737.
[15] F. Witte, Acta biomaterialia, 6 (2010) 1680-1692.
[16] A. Lambotte, L 'traitement des fractures, (1907).
[17] D. Tie, F. Feyerabend, W.-D. Mueller, R. Schade, K. Liefeith, K.U. Kainer, R. Willumeit, European cells & materials, 25 (2012) 284-298; discussion 298.
[18] F. Witte, H. Ulrich, C. Palm, E. Willbold, Journal of biomedical materials research Part A, 81 (2007) 757-765.
[19] S. Zhang, X. Zhang, C. Zhao, J. Li, Y. Song, C. Xie, H. Tao, Y. Zhang, Y. He, Y. Jiang, Acta Biomaterialia, 6 (2010) 626-640.
[20] S. Izumi, M. Yamasaki, Y. Kawamura, Corrosion Science, 51 (2009) 395-402.
[21] X. Gu, Y. Zheng, L. Chen, Biomedical Materials, 4 (2009) 065011.
[22] H. Windhagen, K. Radtke, A. Weizbauer, J. Diekmann, Y. Noll, U. Kreimeyer, R. Schavan, C. Stukenborg-Colsman, H. Waizy, Biomedical engineering online, 12 (2013) 62.
[23] D. Zhao, F. Witte, F. Lu, J. Wang, J. Li, L. Qin, Biomaterials, 112 (2017) 287-302.
[24] D. Zhao, S. Huang, F. Lu, B. Wang, L. Yang, L. Qin, K. Yang, Y. Li, W. Li, W. Wang, Biomaterials, 81 (2016) 84-92.
[25] J.-W. Lee, H.-S. Han, K.-J. Han, J. Park, H. Jeon, M.-R. Ok, H.-K. Seok, J.-P. Ahn, K.E. Lee, D.-H. Lee, Proceedings of the National Academy of Sciences, 113 (2016) 716-721.
[26] B. O'Brien, W. Carroll, Acta biomaterialia, 5 (2009) 945-958.
[27] G. Mani, M.D. Feldman, D. Patel, C.M. Agrawal, Biomaterials, 28 (2007) 1689-1710.
[28] G. Sydow-Plum, M. Tabrizian, Materials Science and Technology, 24 (2008) 1127-1143.
[29] F. Witte, N. Hort, C. Vogt, S. Cohen, K.U. Kainer, R. Willumeit, F. Feyerabend, Current opinion in solid state and materials science, 12 (2008) 63-72.
[30] R. Zeng, W. Dietzel, F. Witte, N. Hort, C. Blawert, Advanced Engineering Materials, 10 (2008) B3-B14.
[31] E. Mostaed, M. Vedani, M. Hashempour, M. Bestetti, Biomatter, 4 (2014) e28283.
[32] Q. Ge, D. Dellasega, A.G. Demir, M. Vedani, Acta biomaterialia, 9 (2013) 8604-8610.
[33] J.-M. Seitz, A. Lucas, M. Kirschner, JOM, 68 (2016) 1177-1182.

[34] H.S. Brar, M.O. Platt, M. Sarntinoranont, P.I. Martin, M.V. Manuel, Jom, 61 (2009) 31-34.
[35] M.B. Kannan, R.S. Raman, Biomaterials, 29 (2008) 2306-2314.
[36] J. Lévesque, D. Dubé, M. Fiset, D. Mantovani, Materials Science Forum, Trans Tech Publ, 2003, pp. 521-526.
[37] Y. Xin, C. Liu, X. Zhang, G. Tang, X. Tian, P.K. Chu, Journal of Materials Research, 22 (2007) 2004-2011.
[38] L. Xu, G. Yu, E. Zhang, F. Pan, K. Yang, Journal of Biomedical Materials Research Part A, 83 (2007) 703-711.
[39] C. Liu, Y. Xin, X. Tian, P.K. Chu, Journal of Materials Research, 22 (2007) 1806-1814.
[40] Y. Xin, K. Huo, H. Tao, G. Tang, P.K. Chu, Acta Biomaterialia, 4 (2008).
[41] Y. Chino, M. Mabuchi, K. Shimojima, Y. Yamada, C.e. Wen, K. Miwa, M. Nakamura, T. Asahina, K. Higashi, T. Aizawa, Materials Transactions, 42 (2001) 414-417.
[42] C. Lorenz, J.G. Brunner, P. Kollmannsberger, L. Jaafar, B. Fabry, S. Virtanen, Acta Biomaterialia, 5 (2009) 2783-2789.
[43] C. Liu, Y. Wang, R. Zeng, X. Zhang, W. Huang, P. Chu, Corrosion Science, 52 (2010) 3341-3347.
[44] W. Zhou, T. Shen, N.N. Aung, Corrosion Science, 52 (2010) 1035-1041.
[45] H. Kuwahara, Y. Al-Abdullat, M. Ohta, S. Tsutsumi, K. Ikeuchi, N. Mazaki, T. Aizawa, (2000).
[46] X. Gu, W. Zhou, Y. Zheng, Y. Liu, Y. Li, Materials Letters, 64 (2010) 1871-1874.
[47] Y. Sun, B. Zhang, Y. Wang, L. Geng, X. Jiao, Materials & Design, 34 (2012) 58-64.
[48] X. Gu, Y. Zheng, S. Zhong, T. Xi, J. Wang, W. Wang, Biomaterials, 31 (2010) 1093-1103.
[49] X. Gu, Y. Zheng, Y. Cheng, S. Zhong, T. Xi, Biomaterials, 30 (2009) 484-498.
[50] G. Song, Advanced Engineering Materials, 7 (2005) 563-586.
[51] A. Srinivasan, P. Ranjani, N. Rajendran, Electrochimica Acta, 88 (2013) 310-321.
[52] Q. Peng, Y. Huang, L. Zhou, N. Hort, K.U. Kainer, Biomaterials, 31 (2010) 398-403.
[53] L. Yang, E. Zhang, Materials Science and Engineering: C, 29 (2009) 1691-1696.
[54] A. Yamamoto, S. Hiromoto, Materials Science and Engineering: C, 29 (2009) 1559-1568.
[55] T. Kokubo, H. Takadama, Biomaterials, 27 (2006) 2907-2915.
[56] Y. Xin, T. Hu, P.K. Chu, Corrosion Science, 53 (2011) 1522-1528.
[57] G. Song, A. Atrens, D. Stjohn, J. Nairn, Y. Li, Corrosion Science, 39 (1997) 855-875.
[58] D. Tie, F. Feyerabend, N. Hort, R. Willumeit, D. Hoeche, Advanced Engineering Materials, 12 (2010) B699-B704.
[59] F. Zhang, A. Ma, J. Jiang, H. Xu, D. Song, F. Lu, Y. Nishida, Progress in Natural Science: Materials International, 23 (2013) 420-424.
[60] N.A. Agha, F. Feyerabend, B. Mihailova, S. Heidrich, U. Bismayer, R. Willumeit-Römer, Materials Science and Engineering: C, 58 (2016) 817-825.
[61] S. Zhang, J. Li, Y. Song, C. Zhao, X. Zhang, C. Xie, Y. Zhang, H. Tao, Y. He, Y. Jiang, Materials Science and Engineering: C, 29 (2009) 1907-1912.
[62] W.D. Müller, M.L. Nascimento, M. Zeddies, M. Córsico, L.M. Gassa, M.A.F.L.d. Mele, Materials Research, 10 (2007) 5-10.
[63] S. Omanovic, S.G. Roscoe, Langmuir, 15 (1999) 8315-8321.
[64] S. Takemoto, M. Hattori, M. Yoshinari, E. Kawada, Y. Oda, Biomaterials, 26 (2005) 829-837.
[65] K. Ide, M. Hattori, M. Yoshinari, E. Kawada, Y. Oda, Dental materials journal, 22 (2003) 359-370.
[66] I. Frateur, L. Lartundo-Rojas, C. Méthivier, A. Galtayries, P. Marcus, Electrochimica Acta, 51 (2006) 1550-1557.
[67] G. Clark, D. Williams, Journal of biomedical materials research, 16 (1982) 125-134.
[68] R.L. Williams, S.A. Brown, K. Merritt, Biomaterials, 9 (1988) 181-186.
[69] L. Yang, N. Hort, R. Willumeit, F. Feyerabend, Corrosion Engineering, Science and Technology, 47 (2012) 335-339.

[70] S. Virtanen, Materials Science and Engineering: B, 176 (2011) 1600-1608.
[71] P. Wan, X. Lin, L. Tan, L. Li, W. Li, K. Yang, Applied Surface Science, 282 (2013) 186-194.
[72] E. Zhang, L. Xu, G. Yu, F. Pan, K. Yang, Journal of biomedical materials research Part A, 90 (2009) 882-893.
[73] W.-D. Mueller, M.L. Nascimento, M.F.L. De Mele, Acta biomaterialia, 6 (2010) 1749-1755.
[74] G. Song, A. Atrens, X. Wu, B. Zhang, Corrosion science, 40 (1998) 1769-1791.
[75] R. Tunold, H. Holtan, M.-B.H. Berge, A. Lasson, R. Steen-Hansen, Corrosion Science, 17 (1977) 353-365.
[76] N. Kirkland, J. Lespagnol, N. Birbilis, M. Staiger, Corrosion Science, 52 (2010) 287-291.
[77] I. Sinisaari, (2004).
[78] S.B. Goodman, Z. Yao, M. Keeney, F. Yang, Biomaterials, 34 (2013) 3174-3183.
[79] T.F. Moriarty, U. Schlegel, S. Perren, R.G. Richards, Journal of Materials Science: Materials in Medicine, 21 (2010) 1031-1035.
[80] M.A. Olsen, J.J. Nepple, K.D. Riew, L.G. Lenke, K.H. Bridwell, J. Mayfield, V.J. Fraser, The Journal of Bone & Joint Surgery, 90 (2008) 62-69.
[81] G. Reid, International journal of antimicrobial agents, 11 (1999) 223-226.
[82] M. Ribeiro, F.J. Monteiro, M.P. Ferraz, Biomatter, 2 (2012) 176-194.
[83] H. Shen, J. Tang, Y. Mao, Q. Wang, J. Wang, X. Zhang, Y. Jiang, Chinese medical journal, 127 (2014) 2748-2752.
[84] N.J. Hickok, I.M. Shapiro, Advanced drug delivery reviews, 64 (2012) 1165-1176.
[85] R.O. Darouiche, New England Journal of Medicine, 350 (2004) 1422-1429.
[86] A. Bogut, J. Niedźwiadek, D. Strzelec-Nowak, J. Blacha, T. Mazurkiewicz, W. Marczyński, M. Kozioł-Montewka, The new microbiologica, 37 (2014) 209-218.
[87] A. Fernandes, M. Dias, Journal of clinical and diagnostic research: JCDR, 7 (2013) 219.
[88] R.A. Brady, J.G. Leid, J.H. Calhoun, J.W. Costerton, M.E. Shirtliff, FEMS Immunology & Medical Microbiology, 52 (2008) 13-22.
[89] P. Vergidis, R. Patel, Infectious disease clinics of North America, 26 (2012) 173-186.
[90] J. Gallo, M. Holinka, C.S. Moucha, International journal of molecular sciences, 15 (2014) 13849-13880.
[91] H. Qin, H. Cao, Y. Zhao, C. Zhu, T. Cheng, Q. Wang, X. Peng, M. Cheng, J. Wang, G. Jin, Biomaterials, 35 (2014) 9114-9125.
[92] D.A. Robinson, R.W. Griffith, D. Shechtman, R.B. Evans, M.G. Conzemius, Acta biomaterialia, 6 (2010) 1869-1877.
[93] H. Qin, Y. Zhao, M. Cheng, Q. Wang, Q. Wang, J. Wang, Y. Jiang, Z. An, X. Zhang, RSC Advances, 5 (2015) 21434-21444.
[94] M.I. Rahim, R. Eifler, B. Rais, P.P. Mueller, Journal of Biomedical Materials Research Part A, (2015).
[95] G. Song, A. Atrens, Adv. Eng. Mater, 5 (2003) 837-858.
[96] A. Nostro, L. Cellini, M. Di Giulio, M. D'Arrigo, A. Marino, A.R. Blanco, A. Favaloro, G. Cutroneo, G. Bisignano, Apmis, 120 (2012) 733-742.
[97] J. Zeng, L. Ren, Y. Yuan, Y. Wang, J. Zhao, R. Zeng, K. Yang, X. Mei, Journal of Materials Science: Materials in Medicine, 24 (2013) 2405-2416.
[98] M.I. Rahim, A. Babbar, S. Lienenklaus, M. Pils, M. Rohde, Biomedical materials (Bristol, England), (2017).
[99] D. Xue, Y. Yun, Z. Tan, Z. Dong, M.J. Schulz, Journal of Materials Science & Technology, 28 (2012) 261-267.
[100] J. Walker, S. Shadanbaz, N.T. Kirkland, E. Stace, T. Woodfield, M.P. Staiger, G.J. Dias, Journal of Biomedical Materials Research Part B: Applied Biomaterials, 100 (2012) 1134-1141.
[101] L. Actis, L. Gaviria, T. Guda, J.L. Ong, Journal of the Korean Association of Oral and Maxillofacial Surgeons, 39 (2013) 43-54.
[102] S.D. Puckett, E. Taylor, T. Raimondo, T.J. Webster, Biomaterials, 31 (2010) 706-713.

[103] V.K. Truong, R. Lapovok, Y.S. Estrin, S. Rundell, J.Y. Wang, C.J. Fluke, R.J. Crawford, E.P. Ivanova, Biomaterials, 31 (2010) 3674-3683.
[104] M. Yoshinari, Y. Oda, T. Kato, K. Okuda, Biomaterials, 22 (2001) 2043-2048.
[105] Y. Zhao, M.I. Jamesh, W.K. Li, G. Wu, C. Wang, Y. Zheng, K.W. Yeung, P.K. Chu, Acta biomaterialia, 10 (2014) 544-556.
[106] V. Alt, T. Bechert, P. Steinrücke, M. Wagener, P. Seidel, E. Dingeldein, E. Domann, R. Schnettler, Biomaterials, 25 (2004) 4383-4391.
[107] B. Hussmann, I. Johann, M. Kauther, S. Landgraeber, M. Jäger, S. Lendemans, BioMed research international, 2013 (2013).
[108] R.J. White, British Journal of Community Nursing, 6 (2001) 3-8.
[109] H.-J. Park, J.Y. Kim, J. Kim, J.-H. Lee, J.-S. Hahn, M.B. Gu, J. Yoon, Water research, 43 (2009) 1027-1032.
[110] C. Marambio-Jones, E.M. Hoek, Journal of Nanoparticle Research, 12 (2010) 1531-1551.
[111] R.O. Becker, Metal-Based Drugs, 6 (1999) 311.
[112] S. Jacquart, R. Siadous, C. Henocq-Pigasse, R. Bareille, C. Roques, C. Rey, C. Combes, Journal of Materials Science: Materials in Medicine, 24 (2013) 2665-2675.
[113] A. Gettler, C. Rhoads, S. Weiss, The American journal of pathology, 3 (1927) 631.
[114] H. Aoyagi, S.-i. Iwasaki, Dental materials journal, 27 (2008) 612-625.
[115] A.B. Lansdown, Advances in pharmacological sciences, 2010 (2010).
[116] L.E. Gaul, A. Staud, Journal of the American Medical Association, 104 (1935) 1387-1390.
[117] J.W. Pifer, B.R. Friedlander, R.T. Kintz, D.K. Stockdale, Scandinavian journal of work, environment & health, (1989) 210-221.
[118] C. Baldi, C. Minoia, A. Di Nucci, E. Capodaglio, L. Manzo, Toxicology letters, 41 (1988) 261-268.
[119] J. Hardes, A. Streitburger, H. Ahrens, T. Nusselt, C. Gebert, W. Winkelmann, A. Battmann, G. Gosheger, Sarcoma, 2007 (2007).
[120] Y.S. Kim, M.Y. Song, J.D. Park, K.S. Song, H.R. Ryu, Y.H. Chung, H.K. Chang, J.H. Lee, K.H. Oh, B.J. Kelman, Particle and fibre toxicology, 7 (2010) 20.
[121] P.L. Drake, K.J. Hazelwood, Annals of Occupational Hygiene, 49 (2005) 575-585.
[122] A. Nayeb-Hashemi, J. Clark, Bulletin of Alloy phase diagrams, 5 (1984) 348-358.
[123] P. Partridge, Metallurgical reviews, 12 (1967) 169-194.
[124] T. Sakai, A. Belyakov, R. Kaibyshev, H. Miura, J.J. Jonas, Progress in Materials Science, 60 (2014) 130-207.
[125] R. Kaibyshev, O. Sitdikov, Physics of metals and metallography, 73 (1992) 635-642.
[126] P. Minárik, R. Král, M. Janeček, Applied Surface Science, 281 (2013) 44-48.
[127] M. Alvarez-Lopez, M.D. Pereda, J. Del Valle, M. Fernandez-Lorenzo, M. Garcia-Alonso, O.A. Ruano, M. Escudero, Acta Biomaterialia, 6 (2010) 1763-1771.
[128] A. Belyakov, H. Miura, T. Sakai, Materials Science and Engineering: A, 255 (1998) 139-147.
[129] S. Ion, F. Humphreys, S. White, Acta Metallurgica, 30 (1982) 1909-1919.
[130] A. Rollett, F. Humphreys, G.S. Rohrer, M. Hatherly, Recrystallization and related annealing phenomena, Elsevier, 2004.
[131] R. Doherty, D. Hughes, F. Humphreys, J. Jonas, D.J. Jensen, M. Kassner, W. King, T. McNelley, H. McQueen, A. Rollett, Materials Science and Engineering: A, 238 (1997) 219-274.
[132] C. Su, L. Lu, M. Lai, Philosophical Magazine, 88 (2008) 181-200.
[133] A. Galiyev, R. Kaibyshev, G. Gottstein, Acta materialia, 49 (2001) 1199-1207.
[134] S. Fatemi-Varzaneh, A. Zarei-Hanzaki, H. Beladi, Materials Science and Engineering: A, 456 (2007) 52-57.
[135] J. Tan, M. Tan, Materials Science and Engineering: A, 339 (2003) 124-132.
[136] Q. Miao, L. Hu, X. Wang, E. Wang, Journal of Alloys and Compounds, 493 (2010) 87-90.

[137] X.-Y. Yang, Y.-K. Zhu, H. Miura, T. Sakai, Transactions of Nonferrous Metals Society of China, 20 (2010) 1269-1274.
[138] Q. Miao, L. Hu, G. Wang, E. Wang, Materials Science and Engineering: A, 528 (2011) 6694-6701.
[139] A. Yamamoto, M. Kakishiro, M. Ikeda, H. Tsubakino, Materials science forum, Trans Tech Publ, 2004, pp. 669-672.
[140] A. Galiyev, R. Kaibyshev, Materials Science Forum, Trans Tech Publ, 2004, pp. 1175-1180.
[141] M. Eddahbi, J. Del Valle, M.T. Pérez-Prado, O.A. Ruano, Materials Science and Engineering: A, 410 (2005) 308-311.
[142] A. Beer, M. Barnett, Materials Science and Engineering: A, 485 (2008) 318-324.
[143] Y. Huang, L. Froyen, Intermetallics, 10 (2002) 473-484.
[144] M. Perez-Prado, O. Ruano, Scripta materialia, 46 (2002) 149-155.
[145] G. Higgins, Journal of Nuclear Materials, 8 (1963) 153-159.
[146] J. Bohlen, S. Yi, J. Swiostek, D. Letzig, H. Brokmeier, K. Kainer, Scripta Materialia, 53 (2005) 259-264.
[147] M.R. Barnett, Materials transactions, 44 (2003) 571-577.
[148] W. Chen, X. Wang, L. Hu, E. Wang, Materials & Design, 40 (2012) 319-323.
[149] H. Somekawa, T. Mukai, Materials Science and Engineering: A, 459 (2007) 366-370.
[150] R.Z. Valiev, T.G. Langdon, Progress in Materials Science, 51 (2006) 881-981.
[151] R.B. Figueiredo, T.G. Langdon, Materials Science and Engineering: A, 501 (2009) 105-114.
[152] X. Gu, N. Li, Y. Zheng, F. Kang, J. Wang, L. Ruan, Materials Science and Engineering: B, 176 (2011) 1802-1806.
[153] W. Thomas, International Patent Application No. PCT/GB92/0220, (1991).
[154] N. Afrin, D. Chen, X. Cao, M. Jahazi, Materials Science and Engineering: A, 472 (2008) 179-186.
[155] M.B. Kannan, W. Dietzel, R. Zeng, R. Zettler, J. Dos Santos, Materials Science and Engineering: A, 460 (2007) 243-250.
[156] S. Koleini, M.H. Idris, H. Jafari, Materials & Design, 33 (2012) 20-25.
[157] J. Kaneko, M. Sugamata, M. Numa, Y. Nishikawa, H. Takada, Journal of the Japan Institute of Metals(Japan), 64 (2000) 141-147.
[158] H. Watanabe, T. Mukai, K. Ishikawa, Journal of Materials Processing Technology, 182 (2007) 644-647.
[159] Z. Zeng, Y. Zhu, S. Xu, M. Bian, C. Davies, N. Birbilis, J. Nie, Acta Materialia, 105 (2016) 479-494.
[160] F. Kaiser, J. Bohlen, D. Letzig, K.-U. Kainer, A. Styczynski, C. Hartig, Advanced Engineering Materials, 5 (2003) 891-896.
[161] F. Kaiser, D. Letzig, J. Bohlen, A. Styczynski, C. Hartig, K.U. Kainer, Materials Science Forum, Trans Tech Publ, 2003, pp. 315-320.
[162] Y. Prasad, K. Rao, Materials Science and Engineering: A, 487 (2008) 316-327.
[163] D. Sarker, J. Friedman, D. Chen, Journal of Alloys and Compounds, 611 (2014) 341-350.
[164] H. Chao, H. Sun, W. Chen, E. Wang, Materials Characterization, 62 (2011) 312-320.
[165] S.-H. Kim, B.-S. You, C.D. Yim, Y.-M. Seo, Materials Letters, 59 (2005) 3876-3880.
[166] G. Allah, A.M. Elhussien, Sudan University of Science and Technology, 2015.
[167] P.J. Potts, P.C. Webb, Journal of Geochemical Exploration, 44 (1992) 251-296.
[168] D.C. Bell, N. Erdman, Low voltage electron microscopy: principles and applications, John Wiley & Sons, 2012.
[169] L. Reimer, Scanning electron microscopy: physics of image formation and microanalysis, Springer, 2013.
[170] J.W. Lichtman, J.-A. Conchello, Nature methods, 2 (2005) 910.

[171] M.M. Avedesian, H. Baker, ASM specialty handbook: magnesium and magnesium alloys, ASM international, 1999.
[172] B. Predel, Ag-Mg (Silver - Magnesium), in: B. Predel (Ed.) Ac-Ag ... Au-Zr: Supplement to Subvolume IV/5A, Springer Berlin Heidelberg, Berlin, Heidelberg, 2006, pp. 1-1.
[173] M. Lim, J.E. Tibballs, P.L. Rossiter, Zeitschrift für Metallkunde, 88 (1997) 162-169.
[174] J. Hanawalt, C. Nelson, J. Peloubet, trans. AIME, 147 (1942) 273-299.
[175] G.L. Song, A. Atrens, Advanced engineering materials, 1 (1999) 11-33.
[176] L. Commin, M. Dumont, J.-E. Masse, L. Barrallier, Acta materialia, 57 (2009) 326-334.
[177] F. Feyerabend, H. Drücker, D. Laipple, C. Vogt, M. Stekker, N. Hort, R. Willumeit, Journal of Materials Science: Materials in Medicine, 23 (2012) 9-24.
[178] M. Carboneras, M. García-Alonso, M. Escudero, Corrosion Science, 53 (2011) 1433-1439.
[179] F. Feyerabend, M. Johannisson, Z. Liu, R. Willumeit-Römer, BioNanoMaterials, 16 (2015) 51-58.
[180] S. Nagel-Heyer, C. Goepfert, F. Feyerabend, J.P. Petersen, P. Adamietz, N.M. Meenen, R. Pörtner, Bioprocess and biosystems engineering, 27 (2005) 273-280.
[181] Z. Liu, R. Schade, B. Luthringer, N. Hort, H. Rothe, S. Müller, K. Liefeith, R. Willumeit-Römer, F. Feyerabend, Oxidative Medicine and Cellular Longevity, 2017 (2017).
[182] L. Scorzolini, M. Lichtner, M. Iannetta, F. Mengoni, G. Russo, A.S. Panni, M. Vasto, M. Bove, C. Villani, C.M. Mastroianni, New Microbiol, 37 (2014) 321-328.
[183] K.E. Piper, M.J. Jacobson, R.H. Cofield, J.W. Sperling, J. Sanchez-Sotelo, D.R. Osmon, A. McDowell, S. Patrick, J.M. Steckelberg, J.N. Mandrekar, Journal of clinical microbiology, 47 (2009) 1878-1884.
[184] H. Rohde, E.C. Burandt, N. Siemssen, L. Frommelt, C. Burdelski, S. Wurster, S. Scherpe, A.P. Davies, L.G. Harris, M.A. Horstkotte, Biomaterials, 28 (2007) 1711-1720.
[185] J. Fischer, D. Pröfrock, N. Hort, R. Willumeit, F. Feyerabend, Materials Science and Engineering: B, 176 (2011) 1773-1777.
[186] G. Caetano-Anollés, P.M. Gresshoff, Promega Notes Magazine, 45 (1994) 13-18.
[187] T. Sakai, J.J. Jonas, Acta Metallurgica, 32 (1984) 189-209.
[188] H. Miura, H. Aoyama, T. Sakai, Journal of the Japan Institute of Metals(Japan), 58 (1994) 267-275.
[189] A. Belyakov, R. Kaibyshev, Nanostructured Materials, 6 (1995) 893-896.
[190] G. Gottstein, L. Chang, H. Yung, Materials Science and Technology, 7 (1991) 158-166.
[191] G. Gottstein, U. Kocks, Acta Metallurgica, 31 (1983) 175-188.
[192] C. Chang, C. Lee, J. Huang, Scripta Materialia, 51 (2004) 509-514.
[193] T. Al-Samman, G. Gottstein, Materials Science and Engineering: A, 490 (2008) 411-420.
[194] O. Sivakesavam, I. Rao, U. PRASAD, Materials Science and technology, 9 (1993) 805-810.
[195] S. Biswas, D.S. Singh, B. Beausir, L.S. Toth, S. Suwas, Metallurgical and Materials Transactions A, 46 (2015) 2598-2613.
[196] H.E. Friedrich, B.L. Mordike, Magnesium technology, Springer, 2006.
[197] M.B. Kannan, Materials Letters, 64 (2010) 739-742.
[198] K. Ma, H. Wen, T. Hu, T.D. Topping, D. Isheim, D.N. Seidman, E.J. Lavernia, J.M. Schoenung, Acta Materialia, 62 (2014) 141-155.
[199] Q. Lu, W. Xu, S. van der Zwaag, Acta Materialia, 77 (2014) 310-323.
[200] Y. Yoshida, K. Arai, S. Itoh, S. Kamado, Y. Kojima, Science and Technology of Advanced Materials, 6 (2005) 185-194.
[201] A. Akhtar, E. Teghtsoonian, Acta Metallurgica, 17 (1969) 1339-1349.
[202] A. Akhtar, E. Teghtsoonian, Philosophical Magazine, 25 (1972) 897-916.
[203] H. Somekawa, H. Watanabe, T. Mukai, Philosophical Magazine, 94 (2014) 1345-1360.
[204] C. Wang, H.-Y. Zhang, H.-Y. Wang, G.-J. Liu, Q.-C. Jiang, Scripta Materialia, 69 (2013) 445-448.

[205] W. Xunhong, W. Kuaishe, Materials Science and Engineering: A, 431 (2006) 114-117.
[206] G.S. Rao, Y. Prasad, Metallurgical Transactions A, 13 (1982) 2219-2226.
[207] T.-C. Chang, J.-Y. Wang, O. Chia-Ming, S. Lee, Journal of Materials Processing Technology, 140 (2003) 588-591.
[208] R. Armstrong, I. Codd, R. Douthwaite, N. Petch, Philosophical Magazine, 7 (1962) 45-58.
[209] K. Kubota, M. Mabuchi, K. Higashi, Journal of Materials Science, 34 (1999) 2255-2262.
[210] E. Zhang, L. Yang, Materials Science and Engineering: A, 497 (2008) 111-118.
[211] E. Ghali, W. Dietzel, K.-U. Kainer, Journal of Materials Engineering and Performance, 13 (2004) 7-23.
[212] E. Oberg, F.D. Jones, H.L. Horton, H.H. Ryffel, J.H. Geronimo, Machinery's handbook, Industrial Press New York, 2004.
[213] T.R. Garrett, M. Bhakoo, Z. Zhang, Progress in Natural Science, 18 (2008) 1049-1056.
[214] V.K. Sharma, K.M. Siskova, R. Zboril, J.L. Gardea-Torresdey, Advances in colloid and interface science, 204 (2014) 15-34.
[215] N. Shahabadi, M. Maghsudi, Z. Ahmadipour, Spectrochimica Acta Part A: Molecular and Biomolecular Spectroscopy, 92 (2012) 184-188.
[216] F. Witte, J. Fischer, J. Nellesen, C. Vogt, J. Vogt, T. Donath, F. Beckmann, Acta Biomaterialia, 6 (2010) 1792-1799.
[217] G. Song, A. Atrens, Advanced engineering materials, 5 (2003) 837-858.
[218] L. Jonášová, F.A. Müller, A. Helebrant, J. Strnad, P. Greil, Biomaterials, 25 (2004) 1187-1194.
[219] Y. Song, D. Shan, R. Chen, F. Zhang, E.-H. Han, Materials Science and Engineering: C, 29 (2009) 1039-1045.
[220] H. Kuwahara, Y. Al-Abdullat, N. Mazaki, S. Tsutsumi, T. Aizawa, Materials Transactions, 42 (2001) 1317-1321.
[221] L. Li, J. Gao, Y. Wang, Surface and Coatings Technology, 185 (2004) 92-98.
[222] D. Williams, Medical device technology, 17 (2006) 9-10.
[223] P. Sabatino, L. Casella, A. Granata, M. Iafisco, I.G. Lesci, E. Monzani, N. Roveri, Journal of Colloid and Interface Science, 314 (2007) 389-397.
[224] P. Roach, D. Farrar, C.C. Perry, Journal of the American Chemical Society, 127 (2005) 8168-8173.
[225] E. Kiss, Colloids and Surfaces A: Physicochemical and Engineering Aspects, 76 (1993) 135-140.
[226] M. Khan, R. Williams, D. Williams, Biomaterials, 20 (1999) 631-637.
[227] D. Williams, I. Askill, R. Smith, Journal of biomedical materials research, 19 (1985) 313-320.
[228] R. Williams, D. Williams, Biomaterials, 9 (1988) 206-212.
[229] K. Merritt, S. Brown, N. Sharkey, Journal of biomedical materials research, 18 (1984) 1005-1015.
[230] X. Cheng, S.G. Roscoe, Biomaterials, 26 (2005) 7350-7356.
[231] P. Liu, J. Tao, Y. Cai, H. Pan, X. Xu, R. Tang, Journal of Crystal Growth, 310 (2008) 4672-4675.
[232] R. Rettig, S. Virtanen, Journal of biomedical materials research part A, 85 (2008) 167-175.
[233] T. Rabilloud, L. Vuillard, C. Gilly, J.-J. Lawrence, Cellular and molecular biology, 40 (1994) 57-75.
[234] C.R. Merril, M.E. Bisher, M. Harrington, A.C. Steven, Proceedings of the National Academy of Sciences, 85 (1988) 453-457.
[235] C.-N. Lok, C.-M. Ho, R. Chen, Q.-Y. He, W.-Y. Yu, H. Sun, P.K.-H. Tam, J.-F. Chiu, C.-M. Che, JBIC Journal of Biological Inorganic Chemistry, 12 (2007) 527-534.
[236] S. Liau, D. Read, W. Pugh, J. Furr, A. Russell, Letters in applied microbiology, 25 (1997) 279-283.

[237] S.A. Jones, P.G. Bowler, M. Walker, D. Parsons, Wound Repair and Regeneration, 12 (2004) 288-294.
[238] T.V. Mathew, S. Kuriakose, Colloids and Surfaces B: Biointerfaces, 101 (2013) 14-18.
[239] S. Grade, J. Eberhard, A. Neumeister, P. Wagener, A. Winkel, M. Stiesch, S. Barcikowski, Rsc Advances, 2 (2012) 7190-7196.
[240] X. Wang, G. Herting, I.O. Wallinder, E. Blomberg, Physical Chemistry Chemical Physics, 17 (2015) 18524-18534.

Acknowledgements

I’m sincerely grateful that my supervisor, Prof. Dr. Regine Willumeit-Römer, gave me the opportunity to study in the field of biomaterials. I really appreciate that my second supervisor, Prof. Dr. Christine Selhuber-Unkel, checked my thesis.

My experimental supervisor, Dr. Frank Feyerabend, supported me strongly to my research and taught me much biological knowledge. The head of WBM, Dr. Thomas Ebel, gave me many useful advices in the thesis writing. The head of WBB, Dr. Bérengère Luthringer, supported me continuously to carry out experiments in biology lab. The head of WZP, Dr. Norbert Hort shared much research experience and writing skills with me. I really appreciate your kind help.

I would like to acknowledge Gábor Szakács for the help of casting and hot extrusion, Gabriele Salamon for the isolation of human primary osteoblasts and Juliane Zirm from iba for bacteria preparation. Monika Luczak gave me great assistance in sample preparation and Gert Wiese provided perfect technical support in metallographic preparation. I thank for the help of Dr. Ronald Schade and Hoger Rothe from iba in antibacterial tests. I’m grateful that Prof. Yuri Estrin, Dr. Jan Bohlen, Dr. Björn Wiese, Luciano Andrei Bergmann and Jochen Harmuth collaborated with me very well and gave me great assistance.

Thanks a lot to all of my colleagues in our biometal institute and the cooperative institutes. I really appreciate your friendship with me.

I thank for the CSC (China Scholarship Council) scholarship and Regine Willumeit-Römer’s financial support during my PhD career. Without the financial assistances, I cannot finish my PhD works. At last, I am very grateful to my parents, my sister and my girlfriend Meng Zhang for their selfless support in my daily life.

Appendix

1. Abbreviations

3-D	Three-dimensional
AE	Auger electrons
AgNPs	Silver nano-particles
α-MEM	Eagle's minimal essential medium
b.c.c.	Body centered cubic
BCM	Bacteria culture medium
BSA	Bovine serum albumin
BSE	Back-scattered electron
CCM	Cell culture medium
CLSM	Confocal laser scanning microscope
CPD	Critical point drying
DAPI	4´,6-Diamidino-2-Phenylindole Dihydrochloride
dDRX	Discontinuous dynamic recrystallization
Diam.	Diameter
DLS	Dynamic light scattering
DMEM	Dulbecco's modified eagle medium
DRX	Dynamic recrystallization
ECAP	Equal channel angular pressing

EDM	Electrical discharge machine
EDS	Energy dispersive X-ray spectroscopy
EIS	Electrochemical impedance spectroscopy
FBS	Fetal bovine serum
f.c.c.	Face centered cubic
FSP	Friction stir processing
GBS	Grain boundary sliding
HA	Hydroxyapatite
HBSS	Hank’s balanced salt solution
h.c.p.	Hexagonal close packing
HUCPV	Human umbilical cord perivascular
ICP-MS	Inductive coupled plasma-mass spectroscopy
LSFE	Low stacking fault energy
MDR	Mean degradation rate
Mg-Ag	Magnesium-Silver
MGS	Mean grain size
OM	Optical metallography
OP-S	Oxide polishing suspensions
PBS	Phosphate buffered saline
PE	Primary electron

PLA	Polylactic acid
P/S	Penicillin/Streptomycin
ROS	Reactive oxygen species
S. aureus	*Staphylococcus aureus*
SBF	Simulated body fluid
Sdr	Developed interfacial areas
SDS	Sodium dodecyl sulfate
SE	Secondary electron
SEM	Scanning electron microscope
S. epidermidis	*Staphylococcus epidermidis*
SFE	Stacking fault energy
SRX	Static recrystallization
T	Temperature
T4	Solution treatment
T6	Aging treatment
UFG	Ultrafine grain
UTS	Ultimate tensile strength
XRD	X-ray diffraction
XRF	X-ray fluorescence
YTS	Yield tensile strength

2. Elements symbols and formulas

Ag	Silver
Ar	Argon
Ca	Calcium
$Ca_5(PO_4)_3OH$	Hydroxyapatite
$CaCl_2$	Calcium chloride
Cl	Chlorine
HCO_3	Carbonate
HNO_3	Nitric acid
K	Potassium
Mg	Magnesium
$Mg(OH)_2$	Brucite
$MgSO_4$	Magnesium sulfate
Na	Sodium
$NaHCO_3$	Sodium bicarbonate
P	Phosphorus
RE	Rare earth
SF_6	Sulfur hexafluoride
Ti	Titanium
Y	Yttrium

Zn	Zink
Zr	Zirconium

3. List of publications and conferences

Papers:

1. Frank Feyerabend, Martin Johannisson, **Zhidan Liu**, Regine Willumeit-Römer. Influence of various sterilization methods on hardness, grain size and corrosion rate of a Mg6Ag-alloy. BioNanoMaterials 16(1), 51-58 (2015). DOI: 10.1515/bnm-2015-0005.
2. **Zhidan Liu**, Ronald Schade, Bérengère Luthringer, Norbert Hort, Holger Rothe, Sören Müller, Klaus Liefeith, Regine Willumeit-Römer, Frank Feyerabend. Influence of the microstructure and silver content on degradation, cytocompatibility and antibacterial properties of Mg-Ag alloy *in vitro*. Oxidative Medicine and Cellular Longevity (2017). DOI: 10.1155/2017/8091265.
3. Nezha Ahmad Agha*, **Zhidan Liu***, Frank Feyerabend, Regine Willumeit-Römer, Billiana Gasharova, Stefanie Heidrich, Boriana Mihailova. The effect of osteoblasts on the surface oxidation processes of biodegradable Mg and Mg-Ag alloys studied by synchrotron IR microspectroscopy (submitted). (* Equally contributed)
4. **Zhidan Liu**, Regine Willumeit-Römer, Frank Feyerabend, Yiyi Lu, Norbert Hort, Luciano Bergmann, Jan Bohlen, Yuri Estrin. Microstructure-properties relationship at the example of Mg-Ag alloys (submitted).
5. **Zhidan Liu**, Regine Willumeit-Römer, Ruiqing Hou, Bérengère Luthringer, Vasyl Mikhailovich Haramus, Frank Feyerabend. Exploration of degradation mechanism of Mg-Ag alloys and the mineralization behavior in the presence of HUCPV cells and human primary osteoblasts (submitted).
6. **Zhidan Liu**, Regine Willumeit-Römer, Dietmar Letzig, Frank Feyerabend, Jan Bohlen. Tensile properties and biodegradation behavior of Mg-Ag alloys after multiple rolling and annealing regulation (submitted).

Conferences:

1. Presentation entitled “Microstructure-Property Relationship for Mg-Ag Alloys as Biodegradable Implant Materials” in the 6th International Conference on Magnesium, ICM6, 2017, Shenyang, *Excellent Oral Presentation*.
2. Presentation entitled “Relationship between microstructure, degradation rate, cytotoxicity and antimicrobial properties of Mg-Ag alloys” in Magnesium in Translational Medicine, Liptovsky Mikulas, 2016, Slovakia.

3. Poster entitled “Magnesium-silver alloys: Antibacterial effects and cell tolerance” in the anniversary of the German Society for Biomaterials e.V, Freiburg, 2015, Germany.
4. Keynote presentation entitled “Cytotoxicity and antibacterial properties of Mg-Ag alloys” in the 7th Symposium on Biodegradable Metals, Carovigno, 2015, Italy.
5. Presentation and poster entitled “Tensile properties of the extruded antibacterial Mg-Ag alloys” in the 6th Symposium on Biodegradable Metals, Maratea, 2014, Italy.

4. Curriculum vitae

Zhidan Liu

E-mail: zhidanliu@163.com

Research Experience

09.2013 - 07.2017	PhD – Thesis: Thermomechanically Processed Mg-Ag alloys as Antibacterial and Biodegradable Implant Materials, Helmholtz-Zentrum Geesthacht (HZG) and Christian-Albrecht-University (CAU) Kiel, Germany
09.2010 - 07.2013	MSc – Thesis: Corrosion Behavior of AZ61 with the Addition of Rare Earth after Hot Extrusion Processing, Zhengzhou University, China
09.2006 - 07.2010	BSc – Thesis: Evaluation of HA/CS/PCS Composites applied in Bone Tissue Engineering, Harbin Institute of Technology (HIT), China

Education Background

09.2013 - 07.2017	A doctoral candidate at the Faculty of Engineering, Christian-Albrecht-University (CAU) Kiel, Kiel, Germany
09.2010 - 07.2013	Master's degree at the School of Materials Science and Engineering, Zhengzhou University, Zhengzhou, China
09.2006 - 07.2010	Bachelor's degree at the School of Materials Science and Engineering, Harbin Institute of Technology (HIT), Weihai, China